SEISMIC HAZARD ANALYSIS AND SEISMIC SLOPE STABILITY EVALUATION IN NORTHWESTERN PAKISTAN

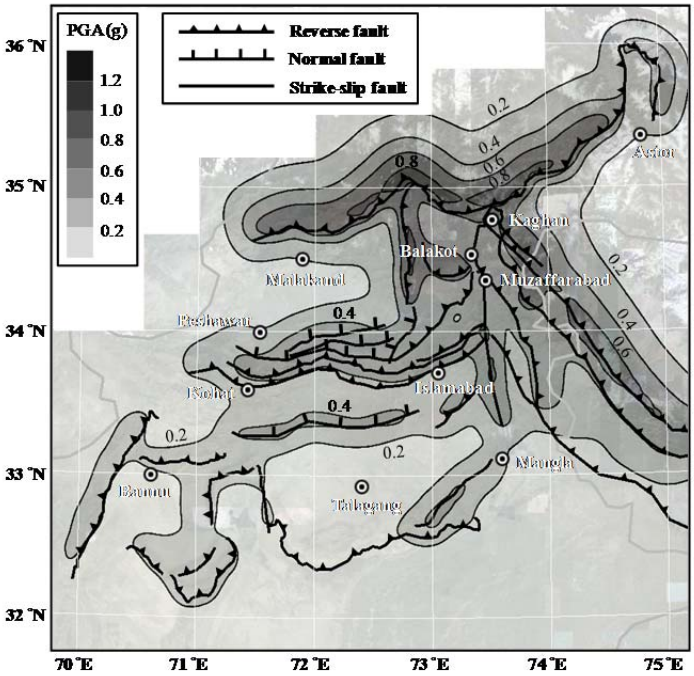

Final Report prepared by:

Youssef M.A. Hashash and Scott M. Olson – Co-PI – Byungmin Kim – Graduate Researcher- University of Illinois at Urbana-Champaigm, Urbana, IL 61801 - USA

Irshad Ahmad – Co-PI – NWFP University of Engineering & Technology, Peshawar - Pakistan

October 2011

SUMMARY

This report evaluates the seismic hazard and slope stability in northwestern Pakistan. The area, located at the western edge of the Himalayas, has numerous active faults including the Main Boundary Thrust (MBT) and Main Mantle Thrust (MMT). This report describes the methodology used to perform regional deterministic and probabilistic seismic hazard analyses. New seismic sources were defined from 32 identified faults while prior studies have been based on diffuse seismicity and areal sources zones. Fault parameters were selected using available data and empirical correlations for faults elsewhere. Recurrence relations were constructed for all discrete faults based on both historical and instrumented seismicity in addition to geologic evidence. Four plate boundary attenuation relations from the Next Generation Attenuation of Ground Motions (Abrahamson et al. 2008) Project were employed to predict ground motions. The selected parameters are compared to measurements from the recent 2005 Kashmir earthquake.

The results from both probabilistic and deterministic seismic hazard analyses exhibit good agreement. Median deterministic spectra compare favorably with uniform hazard spectra (UHS) for 475- or 975-year return periods, while the 84th-percentile deterministic spectra compare favorably with the UHS for a 2475-year return period. Peak ground accelerations (PGAs) for 2475-year return periods exceed 1.0g for Kaghan and Muzaffarabad which are surrounded by major faults. The PGAs for a 475-year return period for these cities are approximately 0.6g – 3 to 4 times greater than estimates by previous studies using diffuse areal source zones. The PGAs for some cities located farther from faults (including Astor, Malakand, Mangla, Peshawar, and Talagang) are similar to those predicted using diffuse areal source zones. Seismic hazard maps for PGA and spectral accelerations at periods of 0.2 sec and 1.0 sec

corresponding to three return period (2475, 975, and 475 years) were produced. Based on deaggregation results, a discussion of the conditional mean spectra for engineering applications is presented.

Landslides are most common consequence of earthquakes, resulting in significant amount of damages of structures and lives. Therefore, predicting locations and severity of landslide is essential part of the earthquake engineering. The most common earthquake-induced landslides occur of shallow disrupted type. However, the currently used seismic slope stability analysis cannot capture the actual trend of landslide distribution, especially high landslide concentration near field. This report proposes the effect of vertical ground acceleration, topographic effect, and bond break effect, in addition to the strong horizontal ground acceleration, as factors that contribute the landslide distribution near earthquake source. Landslide database from four earthquake cases (1989 Loma-Prieta, California; 1999 Chi-Chi, Taiwan; 2005 Kashmir, Pakistan; and 2008 Wenchuan, China) were selected to verify these factors for slope stability analysis. When only horizontal acceleration was considered as current practice of slope stability analysis, the factor of safety did not become less than unity for all cases. However, the factor of safety was predicted to be less than unity near fault and explained well the trend of landslide distribution when vertical acceleration, topographic effect, and bond break effect were taken into account.

TABLE OF CONTENTS

SUMMARY **2**

LIST OF TABLES **6**

LIST OF FIGURES **7**

CHAPTER 1. INTRODUCTION **14**

CHAPTER 2. PRIOR SEISMIC HAZARD STUDIES IN PAKISTAN **18**

2.1 Monalisa et al. (2007) 18

2.2 PMD and NORSAR (2006) 20

2.3 NORSAR and PMD (2006) 20

CHAPTER 3. DETERMINISTIC SEISMIC HAZARD ANALYSIS **24**

3.1 Earthquake catalog 24

3.2 Source characterization 25

3.2.1 Geometry 25

3.2.2 Maximum Magnitude, M_{max} 27

3.2.3 R-factor 27

3.2.4 Comparison with historical earthquake records 28

3.3 Attenuation relationships and parameters 28

3.4 DSHA logic tree 30

3.5 Controlling faults at selected sites 30

3.6 DSHA sensitivity analysis 30

3.7 Comparison with the measurement during 2005 Kashmir earthquake 31

CHAPTER 4. PROBABILISTIC SEISMIC HAZARD ANALYSIS **43**

4.1 Bounded exponential distribution recurrence model 43

4.1.1 Threshold magnitude, m^0, and upper bound magnitude, m^u 44

4.1.2 Activity rate 44

4.1.3 *b*-value 46

4.2 Characteristic distribution recurrence model 47

4.2.1 Characteristic rate A (relation between slip rate and characteristic rate) 48

4.2.2 Characteristic rate B (relation between activity rate and characteristic rate) 49

4.2.3 Characteristic rate C (seismic moment balance method) 50

4.3 Total recurrence 51

4.4 Logic Trees for PSHA 52
4.5 PSHA sensitivity analysis 52
4.6 Evaluation of the proposed PSHA procedure 53
CHAPTER 5. SEISMIC HAZARD RESULTS 63
5.1 Islamabad 63
5.2 Muzaffarabad 64
5.3 Kaghan 65
5.4 Peshawar 65
5.5 Summary of seismic hazard analyses for eleven NW Pakistan cities 66
5.6 Comparison with previous studies 67
5.7 Hazard maps 69
CHAPTER 6. CONDITIONAL MEAN SPECTRA (CMS) 95
6.1 The CMS framework 95
6.2 Application of CMS to two Cities in NW Pakistan 96
CHAPTER 7. SEISMIC SLOPE STABILITY APPROACH 103
7.1 General approaches to analyze seismic slope stability 104
7.2 Pseudo-static slope stability analysis 106
7.3 2005 Kashmir, Pakistan, earthquake using existing pseudo-static slope stability analysis 108
CHAPTER 8. FACTORS THAT AFFECT PSEUDO-STATIC SLOPE STABILITY 117
8.1 Incorporating vertical acceleration into pseudo-static analysis 117
8.2 Topographic effects 118
8.3 Potential bond break effect associated with vertical acceleration 121
CHAPTER 9. PROPOSED NEW APPROACH TO PSEUDO-STATIC SLOPE STABILITY ANALYSIS AND VERIFICATION USING EARTHQUAKE CASES 126
9.1 2005 Kashmir, Pakistan, earthquake 126
9.2 1989 Loma-Prieta earthquake 128
9.3 1999 Chi-Chi, Taiwan, earthquake 130
9.4 2008 Wenchuan, China, earthquake 131
CHAPTER 10. CONCLUSIONS 146

LIST OF TABLES

Table 2-1 Comparison of PGAs (Green) predicted by Monalisa et al. (2007) for 475-year return period using attenuation relations by Ambraseys et al. (1996) and Boore et al. (1997), and by PMD and NORSAR (2006) for 500-year return period using attenuation relation by Ambraseys et al. (1996). 22

Table 3-1 Major historical earthquakes. 34

Table 3-2 Major instrumented earthquakes from the composite earthquake catalog used for this study ($M_w \geq 6.0$). 35

Table 3-3 Fault parameters. Maximum magnitude is for $Z_{tor} = 0$, D = 15 km, and R-factor = 0.9. R, N, and SS denote reverse, normal, and strike-slip, respectively. 36

Table 3-4 The controlling fault and closest source-to-site distance for the DSHA 37

Table 5-1 Mean magnitude and distance from deaggregation for Islamabad and Muzaffarabad. For Islamabad, all earthquakes correspond to the MBT fault, and for Muzaffarabad, all earthquakes correspond to the Riasi thrust. 70

Table 7-1 Hoek-Brown parameters and geometry parameters for four cases. 112

LIST OF FIGURES

Figure 1-1 General tectonic setting of Pakistan with the velocities of plate movement from Larson et al. (1999) and Bilham (2004). Major faults with two active belts are shown. The dashed rectangle denotes the study area in Northwestern Pakistan. 16

Figure 1-2 Faults in NW Pakistan and earthquakes (M_w ≥4.0) from 1505 to 2006 used in this study. Numbers beside faults for identification. See Table 3-3 for fault names and properties. GPS measurement by Bendict et al. (2007) and inferred plate movement from Larson et al. (1999) are shown as arrows. Zones 1, 2, and 3 are for grouping the faults to estimate the slip rates for faults based on available plate movement velocity information. 17

Figure 2-1 Instrumented earthquake (M_w ≥ 4.0) from the composite catalog used in this study with time compared with catalog used by Monalisa et al. (2007). The area considered is 69.5 °E – 75.5 °E, 31.5 °N – 36.5 °N. 23

Figure 3-1 PGA prediction using M_w = 7.6, Z_{tor} = 0, and D = 15 km for foot wall and hanging wall sides with $V_{s,30}$ = 760 m/s. 38

Figure 3-2 Logic tree for faults in NW Pakistan (NWP) using the DSHA. The numbers in parentheses represent the weights assigned for each branch. AS, BA, CB, I represent Abrahamson-Silva (2008), Boore-Atkinson (2008), Campbell-Bozorgnia (2008), and Idriss (2008). The weights for the Z_{tor} are shown in the table. 39

Figure 3-3 DSHA sensitivity analysis to selected attenuation relationships. 40

Figure 3-4 Contour maps of median PGA (left) and 84 percentile of PGA (right) for 2005 Kashmir earthquake using the DSHA procedure and $V_{s,30}$ = 760 m/sec. The grids of 0.1° × 0.1° were used. The measurement stations are shown as black squares. The white line denotes the trace of rupture zone. 41

Figure 3-5 PGA prediction using DSHA for (a) very dense soil and soft rock ($V_{s,30}$ = 560 m/s) and (b) stiff soil ($V_{s,30}$ = 270 m/s), and measured strong motions (Durrani et al. 2005) during the 2005 Kashmir earthquake. Idriss (2008) is not available yet for $V_{s,30}$ < 450 m/s. 42

Figure 4-1 Earthquake distribution (31.5°N-36°N, 69.5°E-75.5°E) as a function of time. Two different periods were considered to construct the earthquake recurrence of faults. Period 1 is from 1981 to 2006 and the Period 2 is from 1975 to 2004. 54

Figure 4-2 Completeness analysis for NW Pakistan for different magnitude classes using Stepp (1972) method. σ_λ = standard deviation, λ = rate of earthquake occurrence, and T_s = time interval. The solid lines are parallel to $1/\sqrt{T_s}$ 55

Figure 4-3 Comparison of fault activity rates (Activity rate 1:1982 to 2006; and Activity rate 2: 1975 to 2004). Numbers represent the fault number used in this study. 56

Figure 4-4 Regression lines using Least Square (LS) method and Maximum Likelihood (Bhat et al.) method (Weichert 1980) for the complementary cumulative rate of observed earthquakes for (a) Period 1 (1981-2006), (b) Period 2 (1975-2004), and (c) declustered catalog (1981-2006). The b = 0.8 line starting from annual earthquake rate at M_w=4 for each case is also shown. 57

Figure 4-5 Relationship between slip rates and characteristic rates of U.S faults. A-type faults in California are divided into several segments which have various slip rate. The characteristic rates for these faults were calculated using three methods (A-priori, Ellsworth, and Hanks and Bakun) used by WGCEP (2008). Boxes are used to illustrate uncertainties in slip rates and characteristic rates for these faults. 58

Figure 4-6 The complementary cumulative rate of observed earthquakes and recurrence models from the composite catalog used in this study. Total recurrence models are sum of all recurrence models of faults. The recurrence models of MBT are shown as examples. 59

Figure 4-7 Logic tree for faults in NW Pakistan using the PSHA. Numbers in parentheses represent weights assigned to each branch. The weights for Z_{tor} are same as DSHA. 60

Figure 4-8 PSHA sensitivity analysis for characteristic rates and activity rates with 975-year return period. All other parameters are used with weights described in the logic tree..... 61

Figure 4-9 PSHA sensitivity analysis for upper bound magnitudes with 975-year return period. All other parameters are used with weights described in the logic tree. 61

Figure 4-10 Contour maps of PGAs with 475- (left) and 2475-year (right) return periods using the PSHA procedure and $V_{s,30}$ = 760 m/sec. The grids of 0.1° × 0.1° were used. 62

Figure 5-1 Seismic hazard analysis results for Islamabad for an assumed bedrock with $V_{s,30}$ of 760 m/sec. (a) PSHA hazard curves for PGA at 5% damping. The hazards by the top five contributing faults are shown; (b) PSHA uniform hazard spectra (UHS) and DSHA hazard spectra. 71

Figure 5-2 Deaggregation of seismic hazard for Islamabad for 475-year return period at three spectral periods of (a) 0.05 sec, (b) 0.2 sec, and (c) 1.0 sec. 72
Figure 5-3 Seismic hazard analysis results for Muzaffarabad for an assumed bedrock with $V_{s,30}$ of 760 m/sec. (a) PSHA hazard curves for PGA at 5% damping. The hazards by the top five contributing faults are shown; (b) PSHA uniform hazard spectra (UHS) and DSHA hazard spectra. 73
Figure 5-4 Deaggregation of seismic hazard for Muzaffarabad for 475-year return period at three spectral periods of (a) 0.05 sec, (b) 0.2 sec, and (c) 1.0 sec. 74
Figure 5-5 Seismic hazard analysis results for Kaghan for an assumed bedrock with $V_{s,30}$ of 760 m/sec. (a) PSHA hazard curves for PGA at 5% damping. The hazards by the top five contributing faults are shown; (b) PSHA uniform hazard spectra (UHS) and DSHA hazard spectra. 75
Figure 5-6 Seismic hazard result for Peshawar for an assumed bedrock with $V_{s,30}$ of 760 m/sec. (a) PSHA hazard curves for PGA at 5% damping. The hazards by the top five contributing faults are shown; (b) PSHA uniform hazard spectra (UHS) and DSHA hazard spectra. 76
Figure 5-7 Comparisons of spectral accelerations computed by PSHA at 475-, 975-, and 2475-year return periods with median and 84th percentile spectral accelerations computed by DSHA for 11 cities in NW Pakistan for an assumed bedrock with $V_{s,30}$ of 760 m/sec. (a) PGA; (b) SA (T = 0.2 sec); and (c) SA (T = 1.0 sec)..... 77
Figure 5-8 Seismic hazard result for Astor for an assumed bedrock with $V_{s,30}$ of 760 m/sec. (a) PSHA hazard curves for PGA at 5% damping. The hazards by the top five contributing faults are shown; (b) PSHA uniform hazard spectra (UHS) and DSHA hazard spectra. 78
Figure 5-9 Seismic hazard result for Balakot for an assumed bedrock with $V_{s,30}$ of 760 m/sec. (a) PSHA hazard curves for PGA at 5% damping. The hazards by the top five contributing faults are shown; (b) PSHA uniform hazard spectra (UHS) and DSHA hazard spectra. 79
Figure 5-10 Seismic hazard result for Bannu for an assumed bedrock with $V_{s,30}$ of 760 m/sec. (a) PSHA hazard curves for PGA at 5% damping. The hazards by the top five contributing faults are shown; (b) PSHA uniform hazard spectra (UHS) and DSHA hazard spectra. 80
Figure 5-11 Seismic hazard result for Kohat for an assumed bedrock with $V_{s,30}$ of 760 m/sec. (a) PSHA hazard curves for PGA at 5% damping. The hazards by the top five contributing faults are shown; (b) PSHA uniform hazard spectra (UHS) and DSHA hazard spectra. 81

Figure 5-12 Seismic hazard result for Malakand for an assumed bedrock with $V_{s,30}$ of 760 m/sec. (a) PSHA hazard curves for PGA at 5% damping. The hazards by the top five contributing faults are shown; (b) PSHA uniform hazard spectra (UHS) and DSHA hazard spectra. 82
Figure 5-13 Seismic hazard result for Mangla for an assumed bedrock with $V_{s,30}$ of 760 m/sec. (a) PSHA hazard curves for PGA at 5% damping. The hazards by the top five contributing faults are shown; (b) PSHA uniform hazard spectra (UHS) and DSHA hazard spectra. 83
Figure 5-14 Seismic hazard result for Talagang for an assumed bedrock with $V_{s,30}$ of 760 m/sec. (a) PSHA hazard curves for PGA at 5% damping. The hazards by the top five contributing faults are shown; (b) PSHA uniform hazard spectra (UHS) and DSHA hazard spectra. 84
Figure 5-15 PGAs computed by PSHA and DSHA for an assumed bedrock with $V_{s,30}$ of 760 m/sec, compared to those computed by others (PMD and NORSAR 2006; Monalisa et al. 2007). PGAs estimated by Monalisa et al. (2007) correspond to a 475-year return period, while PMD and NORSAR (2006) values correspond to a 500-year return period. 85
Figure 5-16 Seismic hazard map of NW Pakistan for PGA at a 475-year return period. A 0.1° × 0.1° grid was analyzed using PSHA for an assumed bedrock with $V_{s,30}$ of 760 m/sec. The contour interval is 0.2g. 86
Figure 5-17 Seismic hazard map of NW Pakistan for PGA at a 975-year return period. A 0.1° × 0.1° grid was analyzed using PSHA for an assumed bedrock with $V_{s,30}$ of 760 m/sec. The contour interval is 0.2g. 87
Figure 5-18 Seismic hazard map of NW Pakistan for PGA at a 2475-year return period. A 0.1° × 0.1° grid was analyzed using PSHA for an assumed bedrock with $V_{s,30}$ of 760 m/sec. The contour interval is 0.2g. 88
Figure 5-19 Seismic hazard map of NW Pakistan for SA (T=0.2 sec) at a 475-year return period. A 0.1° × 0.1° grid was analyzed using PSHA for an assumed bedrock with $V_{s,30}$ of 760 m/sec. The contour interval is 0.4g. 89
Figure 5-20 Seismic hazard map of NW Pakistan for SA (T=0.2 sec) at a 975-year return period. A 0.1° × 0.1° grid was analyzed using PSHA for an assumed bedrock with $V_{s,30}$ of 760 m/sec. The contour interval is 0.4g. 90
Figure 5-21 Seismic hazard map of NW Pakistan for SA (T=0.2 sec) at a 2475-year return period. A 0.1° × 0.1° grid was analyzed using PSHA for an assumed bedrock with $V_{s,30}$ of 760 m/sec. The contour interval is 0.4g. 91

Figure 5-22 Seismic hazard map of NW Pakistan for SA (T=1.0 sec) at a 475-year return period. A 0.1° × 0.1° grid was analyzed using PSHA for an assumed bedrock with $V_{s,30}$ of 760 m/sec. The contour interval is 0.2g. 92
Figure 5-23 Seismic hazard map of NW Pakistan for SA (T=1.0 sec) at a 975-year return period. A 0.1° × 0.1° grid was analyzed using PSHA for an assumed bedrock with $V_{s,30}$ of 760 m/sec. The contour interval is 0.2g. 93
Figure 5-24 Seismic hazard map of NW Pakistan for SA (T=1.0 sec) at a 2475-year return period. A 0.1° × 0.1° grid was analyzed using PSHA for an assumed bedrock with $V_{s,30}$ of 760 m/sec. The contour interval is 0.2g. 94
Figure 6-1 Correlation coefficient suggested by Baker (2008) and Baker and Jayaram (2008). 100
Figure 6-2 CMS at various periods for 475-, 975-, and 2475-year return periods in Islamabad.101
Figure 6-3 CMS at various periods for 475-, 975-, and 2475-year return periods in Muzaffarabad. 102
Figure 7-1 Distribution of landslides triggered by the 2005 Kashmir earthquake, shown as red dots. Epicenter (star mark), Balokot-Garhi fault (Green line), Jhelum fault (blue line), and cities of Muzaffarabad (M) and Balakot (B) are also shown. (Sato et al. 2007). 113
Figure 7-2 Distribution of slope angles for (a) 2005 Kashmir, Pakistan, earthquake (Kamp et al. 2008), (b) 1989 Loma Prieta earthquake (Khazai and Sitar 2004), (c) 1999 Chi-Chi, Taiwan, earthquake (Khazai and Sitar 2004), and (d) 2008 Wenchuan, China, earthquake (Yin et al. 2010). 114
Figure 7-3 Horizontal accelerations with respect to source-to-site distance predicted using the NGA GMPEs for the M_w 7.6 Kashmir, Pakistan, earthquake. 115
Figure 7-4 Landslide concentration data for the 2005 Kashmir, Pakistan, earthquake by Sato et al. (2007) and the mean factor of safety calculated by using existing pseudo-static method. 116
Figure 8-1 Pseudo-static FS computed using various combinations of horizontal and vertical pseudo-static coefficient, k_h and k_v. Strength and geometric properties represent typical values listed in Table 7-1. 122
Figure 8-2 Vertical-to-horizontal acceleration ratio for thrust faults by Elnashai and Papazouglou (1997) and Ambraseys and Simpson (1996). Extrapolated portion from Ambraseys and Simpson (1996) is shown in thinner lines. 123

Figure 8-3 Topographic factors proposed by various researchers. 124
Figure 8-4 Illustration showing procedure of slope stability analysis taking account bond break effect. (a) Dimensions and forces involved in static stability, where W = slice weight; N = normal force; and T = shear force. Side forces are assumed to be equal and opposite, and therefore were not included. (b) Evaluation of "bond break" where $a_{v,max}$ = maximum vertical acceleration; σ_t = tensile strength. 125
Figure 9-1 Flow chart of new approach for the pseudo-static slope stability analysis. AS08, BA08, CB08, and I 08 represent Abrahamson and Silva (2008), Boore and Atkinson (2008), and Campbell and Bozorgnia (2008), and Idriss (2008), respectively. A 05, CB03, EP97, and AS96 represent Ambraseys et al. (2005), Campbell and Bozorgnia (2003), Elnashai and Papazouglou (1997), and Ambraseys and Simpson (1996), respectively. 133
Figure 9-2 Vertical acceleration along the distance from the fault for 1989 Loma-Prieta earthquake. 134
Figure 9-3 Logic tree of slope model for the case of 2005 Kashmir, Pakistan, earthquake. 135
Figure 9-4 Landslide concentration data for the 2005 Kashmir, Pakistan, earthquake (Sato et al. 2007) and factor of safety calculated by using various effects. 136
Figure 9-5 Mean factor of safety and mean ± 1 standard deviation for adding each factor: (a) static condition, (b) with horizontal acceleration (a_h), (c) with a_h and vertical acceleration (a_v), (d) with a_h and topographic effect, (e) with a_h, a_v, and topographic effect, and (f) a_h, a_v, topographic effect, and bond break effect. 137
Figure 9-6 Results of sensitivity analysis for material properties and slope geometry parameters: (a) unit weight, (b) cohesion, (c) friction angle, (d) slope thickness, and (e) slope angle. Mean FS and mean FS ± 1 standard deviation (σ) are shown for each parameter. 138
Figure 9-7 Results of sensitivity analysis for (a) k_h, (b) k_v, (c) topographic factor, (d) horizontal acceleration, and (e) vertical acceleration. 139
Figure 9-8 Limits of southern Santa Cruz Mountains landslide area (left) and locations of earthquake-induced landslides with the surface projection of fault rupture (right) (Keefer 2000) 140
Figure 9-9 Landslide concentration data for the 1989 Loma-Prieta earthquake by Keefer (2000) and factor of safety calculated by using various effects. The mean FS ± 1 standard deviation are shown in a shaded area. 141

Figure 9-10 Locations of landslides induced by 1999 Chi-Chi, Taiwan, earthquake along the Cher-Long-Pu fault and geological setting of affected area (Khazai and Sitar 2004)..... 142
Figure 9-11 Landslide concentration data for the 1999 Chi-chi, Taiwan, earthquake (Khazai and Sitar 2004) and factor of safety calculated by using various effects. 143
Figure 9-12 Distribution of earthquake-triggered landslides (black polygons) on the isoseismic map (Dai et al. 2010) 144
Figure 9-13 Landslide concentration data for the 2008 Wenchuan, China, earthquake (Dai et al. 2010) and factor of safety calculated by using various effects..... 145

CHAPTER 1. INTRODUCTION

Pakistan is located in a highly seismic area and has experienced large and destructive earthquakes historically and in recent times. The most recent severe earthquake occurred on 8 October 2005 in Kashmir, with a moment magnitude of 7.6 and focal depth of 26 km, and was followed by numerous aftershocks (U.S. Geological Survey (USGS) 2010). This earthquake resulted in at least 86,000 fatalities and more than 69,000 injuries (USGS 2010). The earthquake also triggered over 2,400 landslides, extensive liquefaction in alluvial valleys, and numerous building collapses (Bhat et al. 2005; Jayangondaperumal et al. 2008; Aydan et al. 2009). These consequences in a moderately-populated region brought renewed attention to seismic hazards in Pakistan.

Pakistan lies on the Indian Plate, which collides into the Eurasian Plate at a rate of about 45 mm/year and rotates counterclockwise (Sella et al. 2002), and has formed the Himalayan mountain ranges and flexures (Figure 1-1). This rotation and translation of the Indian Plate causes left-lateral slip in Baluchistan at 42 mm/year and right-lateral slip in the Indo-Burman ranges at 55 mm/year (Bilham 2004). The two main active fold-and-thrust belts in northwestern Pakistan region are the Sulaiman belt and the northwest (NW) Himalayan belt as shown in Figure 1-1. The Sulaiman mountain belt at the northwestern margin of the Indian subcontinent contains the Chaman fault where the 2008 Balochistan earthquake (M_w 6.4) occurred (Monalisa and Qasim Jan 2010). This study focuses on the NW Himalayan belt.

Faults along the Himalayan belt have produced countless earthquakes, including four great ($M_w > 8$) earthquakes in 1505, 1803, 1934, and 1950. Bilham and Ambraseys (2005) suggested that there is “missing slip” in Himalayas, reporting that the calculated slip rate of less than 5 mm/yr from the earthquake data over the past 500 years is less than one-third of the

observed slip rate (18 mm/yr) in the past decade. This missing slip is equivalent to four about M_w 8.5 earthquakes that could occur in the near future (Bilham and Ambraseys 2005). The NW Himalayan belt includes several major thrusts, such as the MMT (Main Mantle Thrust) and MBT (Main Boundary Thrust), which have produced several great earthquakes. The faults and seismicity in NW Himalayan belt are shown in Figure 1-2.

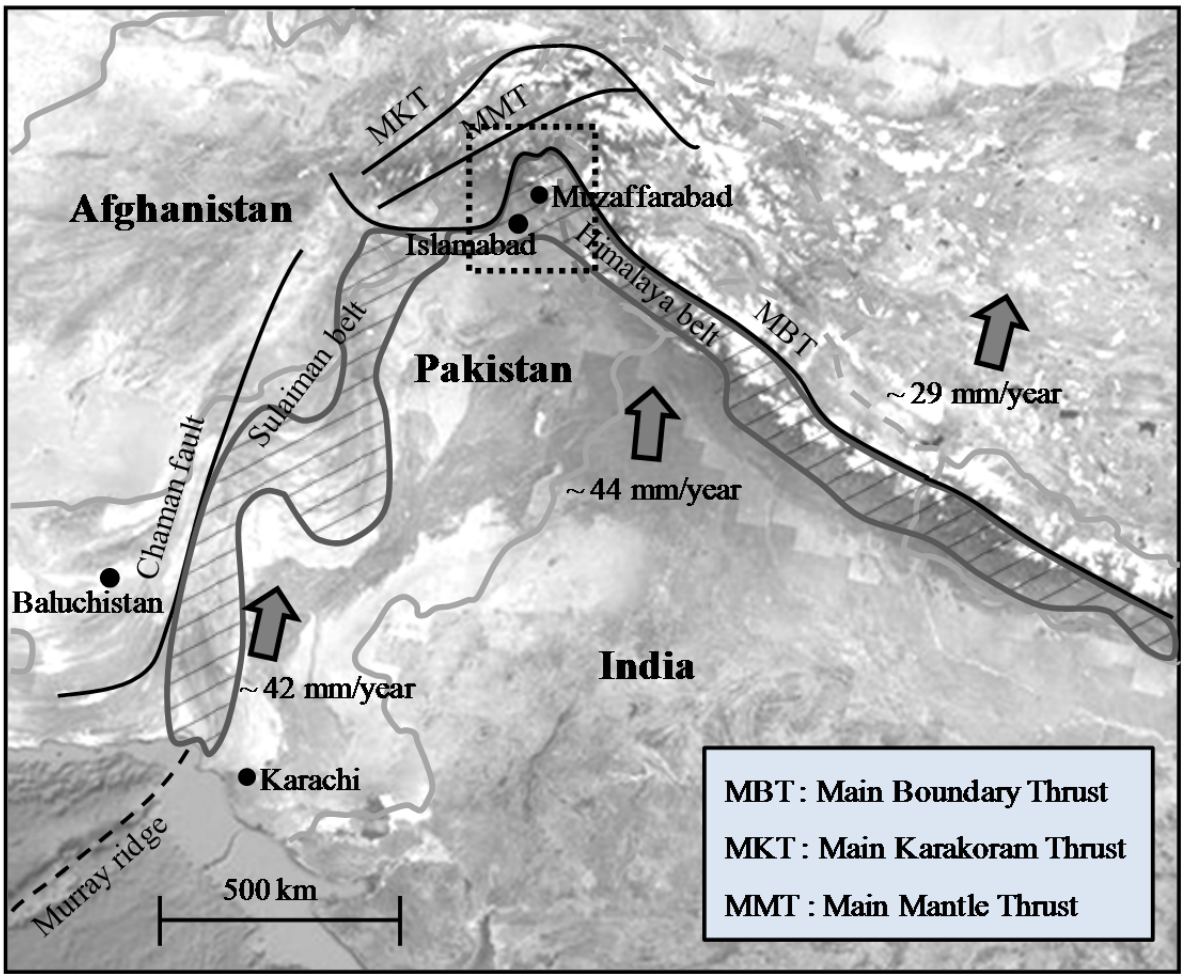

Figure 1-1 General tectonic setting of Pakistan with the velocities of plate movement from Larson et al. (1999) and Bilham (2004). Major faults with two active belts are shown. The dashed rectangle denotes the study area in Northwestern Pakistan.

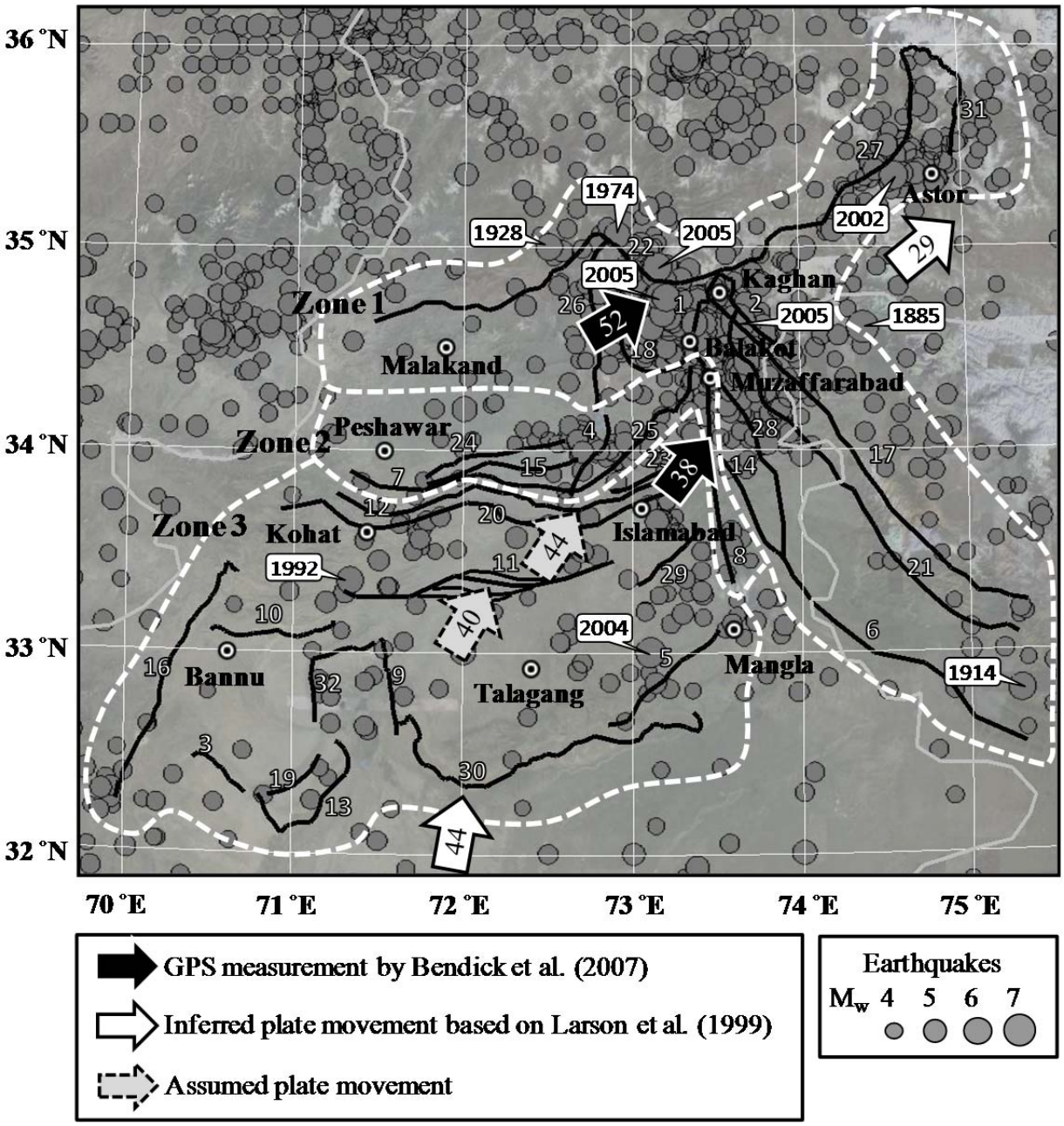

Figure 1-2 Faults in NW Pakistan and earthquakes ($M_w \geq 4.0$) from 1505 to 2006 used in this study. Numbers beside faults for identification. See Table 3-3 for fault names and properties. GPS measurement by Bendict et al. (2007) and inferred plate movement from Larson et al. (1999) are shown as arrows. Zones 1, 2, and 3 are for grouping the faults to estimate the slip rates for faults based on available plate movement velocity information.

CHAPTER 2. PRIOR SEISMIC HAZARD STUDIES IN PAKISTAN

Several seismic hazard studies have been conducted for regions of Pakistan because of its active tectonic setting, including recent studies by Monalisa et al. (2007), NORSAR and Pakistan Meteorological Department (PMD) (2006), and PMD and NORSAR (2006). While these studies incorporate historical and instrumented earthquakes, each involves some potentially limiting assumptions regarding seismic source zone characterization and earthquake catalog construction.

2.1 Monalisa et al. (2007)

Monalisa et al. (2007) presented a probabilistic seismic hazard analysis (PSHA) for the NW Himalayan belt. Their earthquake catalog includes 1057 instrumentally-recorded earthquakes ($M_w \geq 4$) obtained chiefly from the International Seismological Centre (ISC) and U.S. Geological Survey (USGS). Based on this and other geological information, Monalisa et al. (2007) defined four diffuse seismic source zones: the Peshawar-Hazara, Surghar-Kurram, Kohat-Potwar-Salt Range, and Swat-Astor seismic zones (PHSZ, SKSZ, KPSZ, and SASZ, respectively). The corresponding recurrence relations, characterized by b-value, annual activity rate, and upper bound magnitude (m^u), were developed for each seismic source zone. The activity rate and b-value were estimated by earthquake data in each zone, and the upper bound magnitude was estimated by the relationship between magnitude and rupture length (Bonilla et al. 1984; Nowroozi 1985; Slemmons et al. 1989; Wells and Coppersmith 1994). The depth for each seismic zone was defined as the average focal depth of earthquakes in that zone.

Monalisa et al. (2007) performed a PSHA using the Ambraseys et al. (1996) and Boore et al. (1997) attenuation relations to predict peak ground accelerations (PGA) for 10 cities, including Islamabad and Muzaffarabad. Careful review of this study called attention to the unexpectedly low ground motions. For example, the PGA with 475-year return period (i.e., 10%

probability of exceedance (PE) in 50 years) for Islamabad is only 0.1g and 0.15 g with the attenuation relations of Ambraseys and Simpson (1996) and Boore et al. (1997), respectively, despite Islamabad being located within 4 km of the MBT. Similarly, the PGA with 475-year return period is only 0.12g for Muzaffarabad, despite its proximity to Jhelum Fault and Riasi Thrust. PGA values for other cities calculated by Monalisa et al. (2007) are shown in Table 2-1.

The seismic hazard is likely underestimated because of the following reasons:

1. Diffuse areal source zones. Areal source zones are useful where fault haven't been well-characterized. However, the source zones defined by Monalisa et al. (2007) are too diffuse to capture seismicity adjacent to discrete faults. Furthermore, the source zones appear to have neglected the east section of the MBT, which plays an important role in seismic hazard.

2. Incomplete earthquake catalog. The earthquake catalog is missing major events, including the 1555 Kashmir, 1905 Kangra, and 2005 Kashmir earthquakes. In addition, the instrumented earthquake catalog appears incomplete, as illustrated in Figure 2-1. Note that the apparent increase in seismicity in both catalogs in the latter part of the 20th century results from an increase in seismic monitoring, not an increase in actual seismicity. A completeness analysis is presented later in the report.

3. Inconsistency between hazard curves and tabulated PGAs. Values of PGA read from the hazard curves and those tabulated by Monalisa et al. (2007) did not match for many cities. For example, the PGAs reported for Peshawar were 0.14g and 0.15g with 475-year return period using the two attenuation relationships. However, the corresponding PGAs obtained from the hazard curves were approximately 0.32g. Similarly, PGAs reported for Muzaffarabad were 0.1g and 0.13g with 475-year return period, but the hazard curves showed PGAs of about 0.14g and 0.16g.

2.2 PMD and NORSAR (2006)

Seismic hazard was computed for Azad Kashmir and northern Pakistan by using a PSHA based on diffuse areal source zones by the Pakistan Meteorological Department (PMD) and NORSAR (2006). The region was divided into 16 diffuse source zones based on tectonic setting and local seismicity. The earthquake catalog used in their study was based chiefly on the NORSAR database which was collected from agencies worldwide ($M_w \geq 4.5$) (PMD and NORSAR 2006). Another main source was the PMD database containing historical earthquakes from 1905 and most recent instrumented earthquake. Recurrence relations and focal depths for each source zone were developed from earthquakes assigned to each zone. The attenuation model proposed by Ambraseys et al. (1996) was used to establish the seismic hazard contour map of PGA values for return periods of 100, 500, and 1000 years.

The PSHA results yielded low PGA values for Islamabad and Muzaffarabad (see Table 2-1). The PGAs for Islamabad for return periods of 500 years and 1000 years are 0.2g and 0.26g, respectively. The PGAs for Muzaffarabad are 0.2g and 0.31g for return periods of 500 and 1000 years, respectively. The likely reason for the low PGAs is that using diffuse areal source zones tends to "smear" local seismicity corresponding to known faults throughout the entire source area, thereby decreasing seismic hazard.

2.3 NORSAR and PMD (2006)

NORSAR and PMD (2006) performed PHSA for the cities of Islamabad and Rawalpindi. The earthquake data obtained from the databases of the ISC, USGS, EHB, NORSAR, and PMD were used. Based on seismo-tectonic setting, 11 shallow area source zones that cover shallow earthquakes, and one deep zone that covers deep earthquakes in Hindu Kush region were defined. However the deep zone was ignored in their study because it is far from the target cities and does

not affect the hazard result. Like other studies (PMD and NORSAR 2006; Monalisa et al. 2007), the recurrence relations were developed for each source zone using the earthquakes assigned to each zone. In addition to the area source zones, NORSAR and PMD (2006) modeled the Jhelum fault, the strike-slip fault in NW Pakistan, in two segments, and they used the Ambraseys et al. (1996) attenuation relation.

PGA values were reported for a grid of 20 points in a single seismic zone, covering Islamabad and Rawalpindi, and values ranged from 0.19g to 0.21g with 500-year return period. These PGAs are quite low considering that the MBT crosses the study area.

Table 2-1 Comparison of PGAs (Green) predicted by Monalisa et al. (2007) for 475-year return period using attenuation relations by Ambraseys et al. (1996) and Boore et al. (1997), and by PMD and NORSAR (2006) for 500-year return period using attenuation relation by Ambraseys et al. (1996).

Site	Monalisa et al. (2007)		PMD and NORSAR (2006)
	Ambraseys et al. (1996)	Boore et al. (1997)	Ambraseys et al. (1996)
Astor	0.07	0.082	0.28
Bannu	0.06	0.08	0.08
Islamabad	0.10	0.15	0.20*
Kaghan	0.09	0.12	0.20
Kohat	0.20	0.21	0.13
Malakand	0.20	0.21	0.20
Mangla	0.16	0.18	0.10
Muzaffarabad	0.10	0.13	0.20
Peshawar	0.14	0.15	0.20
Talagang	0.15	0.16	0.12

*NORSAR and PMD (2006) reported PGA values for Islamabad ranging from 0.19g to 0.21g with 500-year return period.

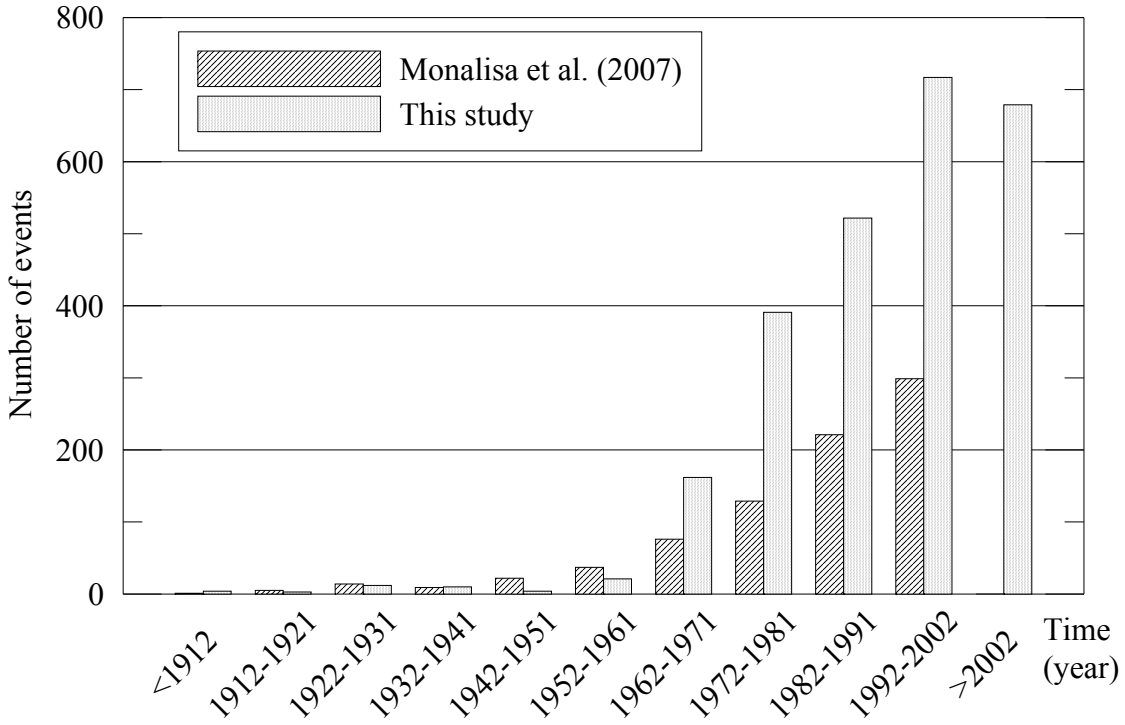

Figure 2-1 Instrumented earthquake ($M_w \geq 4.0$) from the composite catalog used in this study with time compared with catalog used by Monalisa et al. (2007). The area considered is 69.5 °E – 75.5 °E, 31.5 °N – 36.5 °N.

CHAPTER 3. DETERMINISTIC SEISMIC HAZARD ANALYSIS

In this report, we conducted both Deterministic Seismic Hazard Analysis (DSHA) (Reiter 1990) and Probabilistic Seismic Hazard Analysis (PSHA) (Cornell 1968) for NW Pakistan using information available for individual, discrete faults, rather than diffuse source zones. DSHA has an advantage in that less information is required for fault recurrence rates, which is not widely available for NW Pakistan. However, DSHA cannot account for the probability of occurrence of earthquakes. On the other hand, PSHA can incorporate uncertainties in recurrence, M_{max}, attenuation relations, and other parameters.

The four steps for a typical deterministic seismic hazard analysis (Reiter 1990) include 1) characterization of all possible earthquake zones, 2) selection of source-to-site distance, 3) selection of the controlling earthquake source in terms of the ground motion parameters, and 4) computation of seismic ground motions parameters at the site.

3.1 Earthquake catalog

The authors compiled a new earthquake catalog incorporating historical and instrumented seismicity. The historical earthquakes were obtained from the significant earthquake database of National Oceanic and Atmospheric Administration (NOAA). Table 3-1 provides details related to the historical earthquakes incorporated in the catalog.

Figure 2-1 includes instrumented earthquakes in NW Pakistan from catalogs available from the USGS, British Association for the Advancement of Science (BAAS), International Seismological Summary (ISS; 1918~1963), International Seismological Centre (ISC; 1964~present), and PMD. These catalogs use different magnitude scales such as M_w, surface wave magnitude (M_s), body wave magnitude (m_b), and local magnitude (M_L). These magnitudes were converted to M_w for this study. Conversions from Grunthal and Wahlstrom (2003) were

used for M_L and M_s, and conversions from Johnston (1996) and Hanks and Kanamori (1979) were used for m_b. Figure 2-1 shows comparison catalog used in this study and that used by Monalisa et al. (2007). The discrepancy in these two catalogs is a result of using different source information. Table 3-2 summarizes the $M_w > 6$ instrumented earthquakes in NW Pakistan. Duplicate events and manmade events among these catalogs were removed.

3.2 Source characterization

Based on the literature and regional tectonic settings, 32 faults in NW Pakistan were identified as shown in Figure 1-2. The earthquakes in northwestern corner of Figure 1-2 ascribe to the Main Karakoram Thrust (MKT) which is not included in this study because this fault is far from the main cities in NW Pakistan, and will not significantly affect the seismic hazard for these cities. Since the identified faults in NW Pakistan are densely located, the surface projection of the faults could cover most of earthquakes. Some earthquakes that were difficult to attribute to the fault were assigned to nearest fault, thus we chose not to use a background source model in addition to the fault models.

3.2.1 Geometry

Table 3-3 summarizes the geometries for the 32 faults segments considered in this study. Most of characterized faults in NW Pakistan are thrust faults created by compressional stresses due to plate convergence. Other faults, including the Darband, Hissartand, Kund and Nowshera faults, were considered to be normal faults based on the difference of velocities (52 mm/year and 38 mm/year) measured by Bendick et al. (2007) as shown in Figure 1-2. Faults striking from west to east were assumed to dip northward, while faults striking northwest to southeast were assumed to dip northeastward due to the movement of Indian Plate which subducts underneath the Eurasian Plate (McDougall and Khan 1990; Mukhopadhyay and Mishra 2005; Bendick et al.

2007; Raghukanth 2008). It was assumed that thrust faults dip at 30°, while normal and reverse faults dip at 60° due to lack of information on fault dip angle. The Dijabba, Jhelum, and Kalabagh faults are strike-slip (McDougall and Khan 1990; Dasgupta et al. 2000) and were assumed to dip at 90°. Since major cities are located on the footwall side of faults, the influence of dip angles on seismic hazard for these cities is limited, although further study of dip angle can improve the hazard result for hanging wall zones. The USGS divides large faults in California into multiple segments to take account for differences in slip rate, maximum potential magnitude, fault geometry, etc. On this basis, we divided the MBT, one of the chief faults in the region, into an east segment striking E-W and west segment striking NW-SE because these two segments are subject to different tectonic mechanisms due to their differing orientations.

Many of the faults in NW Pakistan lack sufficient characterization for seismic hazard analysis. Therefore, we considered the geometry of well-studied faults in Western U.S. as analogs for some faults in NW Pakistan, based on similar tectonic settings. The faults in NW Pakistan and in Western U.S. are both shallow crustal faults located along plate boundaries and are of similar age (McDougall and Khan 1990; Searle 1996; Dipietro et al. 2000). Western U.S. is located in a collision zone forming Cascadia subduction zone and San Andreas fault as well as numerous shallow crustal faults. The Pacific Northwest faults consist of many reverse faults due to collision of two plates. For California, there are also compressional stresses due to collision, resulting in some oblique and reverse faults (B-type). We recognize that this analogy is quite limited but unfortunately we lack the needed information on faults in Pakistan. Based on this assumed, yet limited, analog, we assigned depths to top of rupture, Z_{tor}, for all faults the same values and weights used by Petersen (2008) for the USGS seismic hazard mapping project. Specifically, Z_{tor} = 0, 2 km, and 4 km were assigned based on M_{max} for each fault with weights

which will be discussed in Section 3.4. A variable depth to the bottom of rupture (D) was used, with values of 10 km, 15 km, and 20 km, based on the USGS databases for Intermountain West, Pacific, and California faults.

3.2.2 Maximum Magnitude, M_{max}

Tocher (1958) first suggested a correlation between maximum earthquake magnitude that the fault is capable of producing and rupture parameters such as length and displacement. More recently, Wells and Coppersmith (1994) collected source parameters for 421 historical earthquakes and developed empirical relationships between M_{max} and rupture area (RA), rupture length, and rupture width. Hanks and Bakun (2002; 2008) and Working Group on California Earthquake Probabilities (WGCEP) (2003) suggested that the Wells and Coppersmith (1994) correlation slightly underestimates M_{max} for large RAs and proposed alternate relationships. In this study, we estimated M_{max}, using both relationships proposed by and Hanks and Bakun (2008) and Ellsworth B (WGCEP 2003) as the USGS (Petersen 2008) and WGCEP (2008) used. The average of two estimated M_{max} was used directly in the DSHA, and as the upper bound magnitude, m^u, in the PSHA as discussed later.

3.2.3 R-factor

WGCEP (2003) and WGCEP (2008) used a seismogenic factor, R, to account for aseismic slip, i.e., fault creep not contributing to seismicity. The R-factor can be calculated as:

$$R = 1 - b_s / b_l \qquad \text{Eq. (1)}$$

where b_s is slip rate at seismogenic depths and b_l is slip rate at greater depths. Values of b_s can be estimated from geodetic data and b_l can be estimated from either geological or geodetic data. An

R of unity implies that all fault slip occurs as earthquakes, while R = 0 implies that all fault slip occurs as aseismic creep. Multiplying the computed fault RA by R reduces the effective rupture area, and in turn, decreases the effective M_{max}. Singh (2000) suggested that there is an aseismic zone in the region lying between 35°N-40°N and 66°E-76°E which is adjacent to the study area of this study. Therefore, we considered that it is possible for faults in NW Pakistan to experience aseismic creep. Due to lack of geologic and geodetic information for faults in NW Pakistan, R-factors of 0.8, 0.9, and 1.0 were assigned to the NW Pakistan faults with weights in this study based on the values assigned to California faults (WGCEP 2003; WGCEP 2008).

3.2.4 Comparison with historical earthquake records

Table 3-3 provides M_{max} values computed from M_{max}-RA relationships and adjusted by R-factors. These values agree well with historical earthquakes. Most of the faults have M_{max} values ranging from 7.1 to 7.9, comparable to the major historical earthquakes in the catalog (Table 3-1; $M_w \sim 6.3$ to 7.8). Faults with computed $M_{max} > 8$, i.e., MBT (west), MBT (east), MMT, and MCT, are located along the Himalayan belt, and the M_{max} values are consistent with the earthquake magnitudes ($M_w \sim 8.5$) suggested by Bilham and Ambraseys (2005).

3.3 Attenuation relationships and parameters

Since there is no ground-motion model available for the region of Pakistan, we used five sets of ground-motions released by the Next Generation of Ground-Motion Attenuation Models (NGA) project (Power et al. 2008); Abrahamson-Silva, Boore-Atkinson, Campbell-Bozorgnia, Chiou-Youngs, and Idriss. These relations provide horizontal PGA, peak ground velocity (PGV), and 5% damped elastic pseudo-response spectral accelerations in the period range of 0 to 10 seconds for shallow crustal earthquakes. These NGAs were developed by using significant earthquakes along the plate boundaries including 1995 Kobe, Japan, and 1999 Chi-Chi, Taiwan,

earthquakes as well as numerous earthquakes in Western U.S. As discussed earlier, NW Pakistan is also located in the plate convergence region, and contains many shallow crustal faults such as MBT and MMT. Therefore we concluded that applying the NGAs for NW Pakistan is reasonable.

For all of the relations, we assumed a Site Class B/C boundary condition in the upper 30m (shear wave velocity, $V_{s,30}$ = 760 m/sec). The Abrahamson and Silva (2008) and Chiou and Youngs (2008) attenuation relations require a depth to reach V_s = 1 km/sec, $Z_{1.0}$. For $V_{s,30}$ = 760 m/sec, we computed $Z_{1.0}$ = 32 m and 24 m using their recommended correlations, respectively. The Campbell and Bozorgnia (2007) relation requires a depth to reach V_s = 2.5 km/sec, $Z_{2.5}$. For $V_{s,30}$ = 760 m/sec, we computed $Z_{2.5}$ = 0.63 km using their recommended correlation.

Figure 3-1 shows the PGA values predicted using $V_{s,30}$ = 760 m/s. As expected, the predicted PGAs for the hanging wall side of the thrust fault exceed the foot wall values until the site distance exceeds the distance to the surface of the fault plane. The Chiou and Youngs (2008) relation yields significantly larger PGAs than the other attenuation relations at distances to fault less than 15 km; therefore, we did not utilize their relation in this study. In all seismic hazard analyses performed in this study, we equally weighted ground motion parameters computed using the remaining four relations. For this current regional study we do not incorporate directivity effects. The NGA-west2 project is currently under way to incorporate directivity in the attenuation equations which can overcome the shortcomings of the currently used formulation by Somervile (1997). Use of these future attenuation relationships will improve the seismic assessment in this region.

3.4 DSHA logic tree

In a DSHA, a logic tree is used to consider alternative options for input parameters and predictive models used to estimate seismic hazard. Figure 3-2 presents the logic tree and branch weights used for all DSHA performed in this study. As described above, values of Z_{tor} and the corresponding weights used by Petersen (2008) for Quaternary faults in western United States were used in this study. Weights of 0.4, 0.4, and 0.2 were assigned to D = 10, 15, and 20 km, respectively. Weights of 0.2, 0.6, and 0.2 were assigned to R = 0.8, 0.9, and 1.0, respectively, based on the data from California faults. Lastly, the four selected attenuation relationships were equally weighted.

3.5 Controlling faults at selected sites

For locations proximate to multiple individual faults (or fault segments), the DSHA was repeated for each fault segment to define the maximum ground motion parameter predicted at the subject location and the corresponding controlling fault. Table 3-4 lists the controlling faults that give the highest amplitude spectral accelerations at all periods at selected cities in Pakistan. Because of the similarities of most M_{max} values, the controlling fault for most cities considered here is the most proximate fault. However, for some cities like Astor and Peshawar, more distal faults with larger M_{max} values are the controlling faults.

3.6 DSHA sensitivity analysis

Sensitivity analyses were conducted to understand the influence of a number of parameters on the DSHA results. The sensitivity analysis using the depth to the bottom of rupture (D) of 10 km, 15 km, and 20 km revealed that the D did not significantly influence the computed hazard for Islamabad and Muzaffarabad. These cities are located on the footwall of the controlling faults, and D does not influence the distance to fault for sites located on the footwall.

For sites such as Kaghan, located on a hanging wall, the distance to fault does not change if the site is within the horizontal projection of controlling fault, and therefore, D has little influence on seismic hazard (e.g., the median PGAs of 0.73g and 0.70g for Kaghan were yield for using D=10 km and 20 km, respectively). We also conducted the sensitivity analysis for dip angles (20° and 40°) of thrust fault models, and found that these dip angles also have a minor influence on seismic hazard for most of major cities located on a footwall. For the city like Peshawar which is located on the hanging wall side, the median PGAs of 0.74g and 0.70g were computed for dip angles of 20° and 40°, respectively. Similarly, the R-factor has little influence on the seismic hazard, at least for the small range of R values applied in this study. The difference in R of 0.2 only changes M_{max} by approximately 0.1 magnitude units. The median PGAs of 0.50g and 0.51g were computed for Islamabad using R = 0.8 and 1.0 respectively.

Figure 3-3 illustrates the DSHA sensitivity to the attenuation relations. As illustrated in the figure, the Idriss (2008) relation predicts higher PGAs while the other three NGA relations (Abrahamson and Silva 2008; Boore and Atkinson 2008; Campbell and Bozorgnia 2008) predict similar PGAs. Furthermore, the weighted PGAs are close to the PGAs predicted by these latter three relations.

3.7 Comparison with the measurement during 2005 Kashmir earthquake

As an initial validation of the DSHA model developed here, we compared measured accelerations during the 2005 Kashmir earthquake obtained by Durrani et al. (2005) with those predicted by DSHA. In order to predict the ground motion based on the methodology proposed in this study, all parameters and weights proposed in this report were considered except for the location of rupture. The rupture occurred during 2005 Kashmir earthquake is approximately 60 km long, with a focal depth of about 26 km (USGS 2010). We assumed the focal depth as a depth

to the bottom of rupture because most of aftershocks occurred shallower than this focal depth (Bendick et al. 2007) and other studies also reported similar depths to the bottom of rupture (Durrani et al. 2005; Bendick et al. 2007). Using the dip angle of 30° as assumed for thrust faults in NW Pakistan, the maximum magnitudes were calculated to be 7.60, 7.66, and 7.71 with the R-factor of 0.8, 0.9, and 1.0, respectively. These magnitudes are consistent with the reported magnitude (M_w 7.6) and used in the DSHA with assigned weights. We set $Z_{tor} = 0$ because $M_w > 7$ as described in Figure 3-2. Since site conditions at the recording stations are not known, we assumed that each recording station classified as Site Class C (very dense soil and soft rock) with $V_{s,30} = 560$ m/s and Site Class D (stiff soil) with $V_{s,30} = 270$ m/s. The DSHA was performed for these Site Classes, and for these $V_{s,30} = 560$ m/s and 270 m/s, $Z_{1.0} = 130$ m and 500 m, respectively (Abrahamson and Silva 2008) and $Z_{2.5} = 0.99$ km and 2.3 km, respectively (Campbell and Bozorgnia 2008).

Figure 3-4 presents contour maps of median and 84 percentile (median plus one standard deviation, σ) PGA, respectively, for uniform firm rock conditions corresponding to $V_{s,30} = 760$ m/s (Site Class B/C boundary). Figure 3-5 shows the predicted PGA attenuation with distance modified to Site Class C ($V_{s,30} = 560$ m/s) and Site Class D ($V_{s,30} = 270$ m/s) to facilitate comparison to the measured values. Two ground accelerations in two horizontal directions for each station (Abbottabad, Murree, and Nilore) with ± 10 km uncertainty of distance to fault are shown in the Figure 3-5. The peak ground accelerations measured at the rock station of Tarbela Dam, and at the base of Barotha Power Complex are also shown. The mean + 1σ of the median predictions for $V_{s,30} = 560$ m/s envelopes each site other than Nilore. The Nilore measurement was likely affected by the raft foundation dimensions where the instrument was placed (Durrani et al. 2005). For $V_{s,30} = 270$ m/s, only three attenuation relationships excluding Idriss (2008)

were used with equal weights because the parameters for Idriss (2008) are not available for $V_{s,30}$ < 450 m/s. The computed PGAs for $V_{s,30}$ = 270 m/s are slightly smaller than for $V_{s,30}$ = 560 m/s near the fault, but become greater at far distance where the recording stations are located. Overall, we consider the comparison to be acceptable.

Table 3-1 Major historical earthquakes.

Earthquake	Year	Estimated M_w	Estimated Max. MMI	Details	Source
Paghman, Afghanistan (34.60°N, 68.93°E)	1505	7.0 - 7.8	IX - X	60-km rupture of Chaman fault. Strike-slip and dip-slip movement	Quittmeyer and Jacob (1979)
Kashmir, Pakistan (33.50°N, 75.50°E)	1555	7.6	n/a	Limited intensity reports available	Ambraseys and Douglas (2004)
Alingar Valley, Afghanistan (34.83°N, 70.37°E)	1842	n/a	VIII - IX	Several hundred fatalities in Alingar River valley and Jalalabad Basin	Quittmeyer and Jacob (1979)
Kashmir, Pakistan (34.60°N, 74.38°E)	1885	6.3	VIII - IX	3,000 fatalities. Numerous buildings destroyed; large fissures observed; large landslide triggered south of Baramula	Lawrence (1967) Quittmeyer and Jacob (1979) Bilham (2004)
Chaman, Pakistan (30.85°N, 66.52°E)	1892	6.75	IIV-IX	30-km rupture of Chaman fault; Left-lateral strike-slip movement	Heuckroth and Karim (1973) Quittmeyer and Jacob (1979)
Kangra, India (33.00°N, 76.00°E)	1905	7.83±0.18	n/a	20,000 fatalities; 100,000 buildings destroyed; limited instrumented data available	Ambraseys and Bilham (2000) Kaul (1911)

Table 3-2 Major instrumented earthquakes from the composite earthquake catalog used for this study ($M_w \geq 6.0$).

Year	Latitude	Longitude	Magnitude (M_w)
1914	32.80 °N	75.30 °E	6.2
1928	35.00 °N	72.50 °E	6.0
1972	36.00 °N	73.33 °E	6.4
1974	35.10 °N	72.90 °E	6.1
1981	35.68 °N	73.60 °E	6.3
1992	33.35 °N	71.32 °E	6.0
2002	35.34 °N	74.59 °E	6.4
2004	33.00 °N	73.10 °E	6.6
2005	34.63 °N	73.63 °E	7.6
2005	34.90 °N	73.15 °E	6.4
2005	34.75 °N	73.20 °E	6.2
2005	34.76 °N	73.16 °E	6.1

Table 3-3 Fault parameters. Maximum magnitude is for Z_{tor} = 0, D = 15 km, and R-factor = 0.9. R, N, and SS denote reverse, normal, and strike-slip, respectively.

Fault ID	Fault name	Type	Dip (°)	Length (km)	Max. magnitude (M_w)	Slip rate (mm/yr)	Activity rate		Characteristic rate		
							1	2	A	B	C
1	Balakot Shear Zone	R	60	44	6.9	0.56	0.824	0.000	0.00048	0.00040	0.00049
2	Batal Thrust	R	30	65	7.4	0.83	0.745	0.133	0.00068	0.00057	0.00036
3	Bhittani Thrust	R	30	39	7.2	0.17	0.118	0.067	0.00017	0.00016	0.00011
4	Darband Fault	N	60	51	7.0	1.21	0.157	0.000	0.00095	0.00008	0.00095
5	Dijabba Fault	SS	90	83	7.2	0.37	0.549	0.600	0.00033	0.00122	0.00022
6	Himalayan Frontal Thrust	R	30	187	8.0	2.39	0.078	0.067	0.00175	0.00014	0.00046
7	Hissartang Fault	N	60	129	7.5	3.08	0.157	0.167	0.00221	0.00034	0.00119
8	Jhelum Fault	SS	90	138	7.5	3.30	3.960	0.267	0.00234	0.00235	0.00135
9	Kalabagh Fault	SS	90	53	7.0	0.24	0.078	0.033	0.00022	0.00009	0.00020
10	Karak Thrust	R	60	80	7.3	0.36	0.157	0.067	0.00032	0.00018	0.00020
11	Khair-I-Murat Fault	N	60	152	7.6	4.00	0.471	0.500	0.00279	0.00102	0.00137
12	Khairabad Fault	R	60	225	7.8	2.00	0.118	0.100	0.00149	0.00022	0.00057
13	Khisor Thrust	R	30	96	7.6	0.43	0.196	0.200	0.00038	0.00041	0.00014
14	Kotli Thrust	R	30	65	7.4	0.83	0.039	0.033	0.00067	0.00007	0.00036
15	Kund Fault	N	60	85	7.3	2.03	0.039	0.033	0.00151	0.00007	0.00108
16	Kurram Thrust	R	30	148	7.8	0.66	0.235	0.267	0.00055	0.00054	0.00015
17	MCT	R	30	333	8.3	4.25	1.451	0.600	0.00294	0.00166	0.00054
18	Mansehra Thrust	R	30	53	7.3	0.68	2.118	0.134	0.00056	0.00125	0.00034
19	Marwat Thrust	R	30	35	7.1	0.16	0.235	0.000	0.00015	0.00011	0.00011
20	MBT west	R	30	225	8.1	4.00	0.392	0.400	0.00279	0.00083	0.00068
21	MBT east	R	30	333	8.3	4.25	1.803	0.23	0.00294	0.00124	0.00054
22	MMT	R	30	340	8.3	4.34	7.373	1.833	0.00300	0.00651	0.00054
23	Nathiagali Thrust	R	30	59	7.4	0.27	0.196	0.033	0.00024	0.00015	0.00012
24	Nowshera Fault	N	60	80	7.3	1.92	0.392	0.467	0.00144	0.00093	0.00106
25	Punjal Thrust	R	30	103	7.7	2.46	0.627	0.500	0.00180	0.00110	0.00075
26	Puran Fault	R	60	102	7.4	1.31	4.471	0.533	0.00102	0.00303	0.00060
27	Raikot Fault	R	60	63	7.1	0.80	0.706	0.000	0.00065	0.00034	0.00053
28	Riasi Thrust	R	30	105	7.7	1.34	1.569	0.300	0.00104	0.00124	0.00040
29	Riwat Thrust	R	30	38	7.2	0.17	0.275	0.333	0.00016	0.00066	0.00011
30	Salt Range Thrust	R	30	193	8.0	0.87	0.196	0.200	0.00070	0.00041	0.00016
31	Stak Fault	R	60	62	7.1	0.79	0.824	1.167	0.00065	0.00226	0.00053
32	Surghar Range Thrust	R	30	67	7.4	0.30	0.235	0.167	0.00027	0.00038	0.00013

Table 3-4 The controlling fault and closest source-to-site distance for the DSHA

Cities	Fault number	Fault name	Closest distance (km)
Astor	22	MMT	23.91
Balakot	8	Jhelum Fault	1.94
Bannu	10	Karack Fault	8.57
Islamabad	20	MBT (west)	3.14
Kaghan	17	MCT	3.42
Kohat	20	MBT (west)	1.55
Malakand	22	MMT	21.09
Mangla	5	Dijabba Fault	8.78
Muzaffarabad	28	Riasi Thrust	1.78
Peshawar	20	MBT (west)	20.76
Talagang	30	Salt Range Thrust	23.56

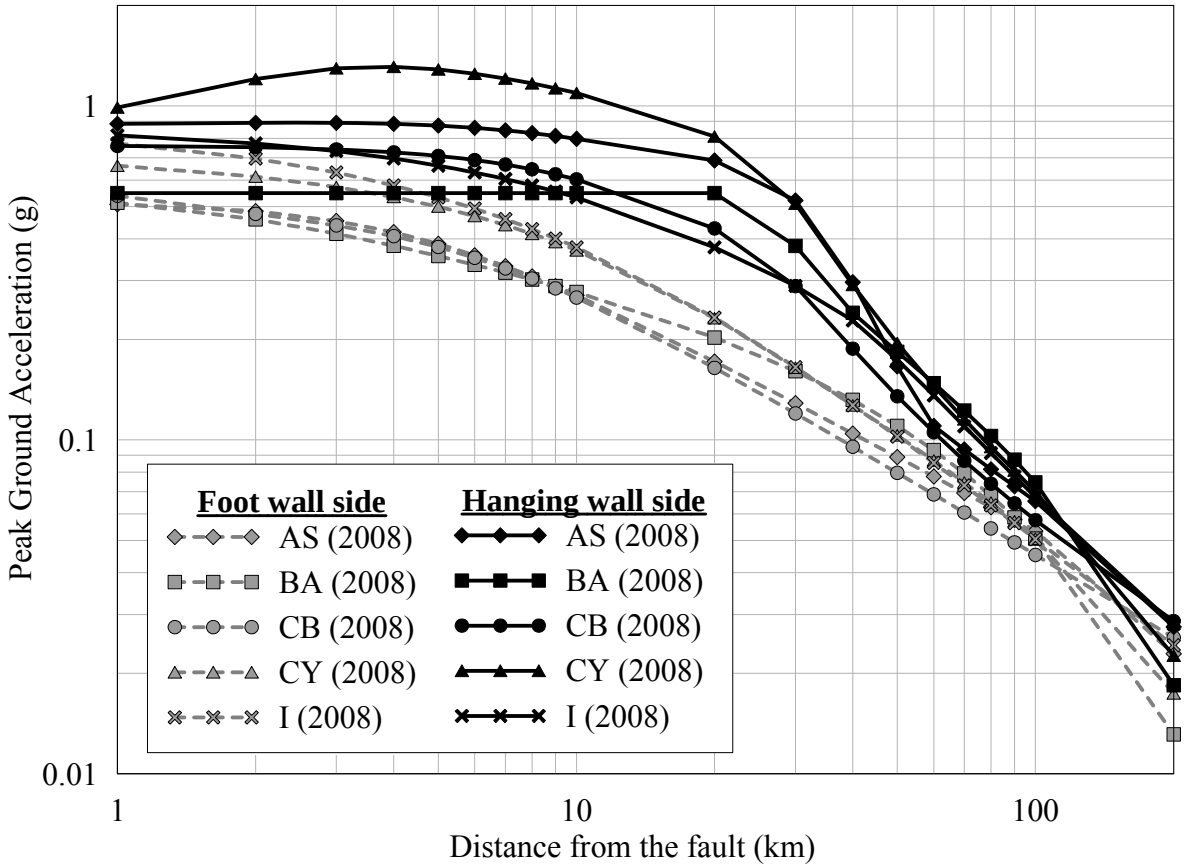

Figure 3-1 PGA prediction using M_w = 7.6, Z_{tor} = 0, and D = 15 km for foot wall and hanging wall sides with $V_{s,30}$ = 760 m/s.

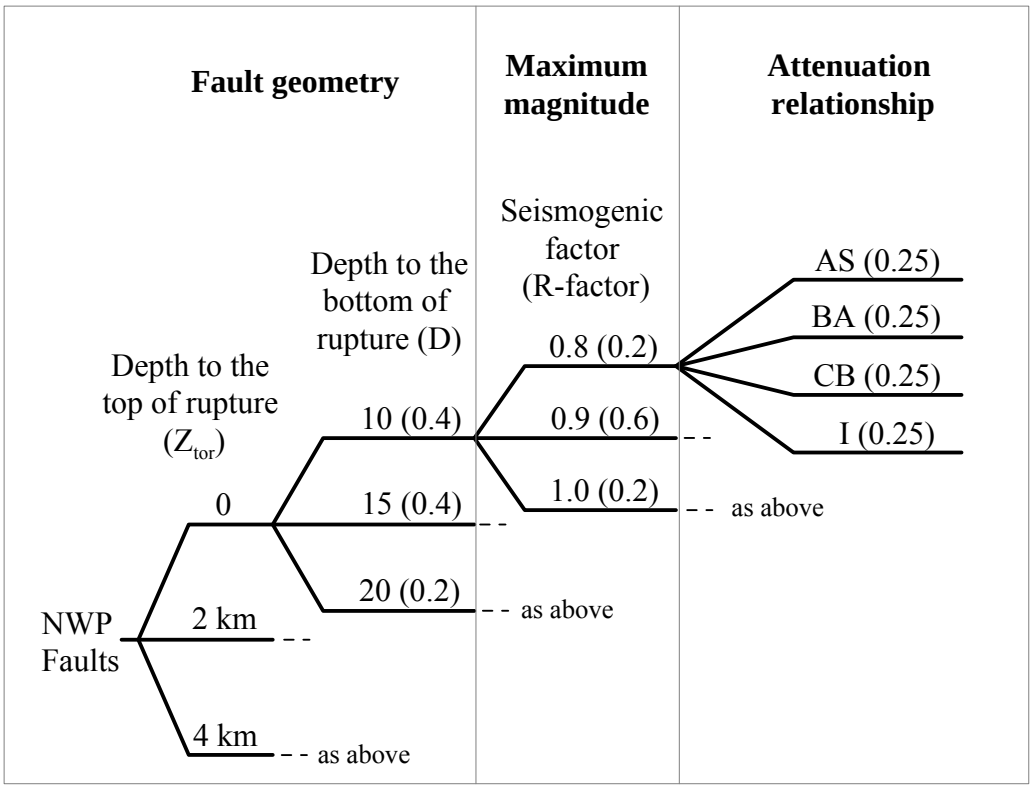

Weights for the depth to the top of rupture, Z_{tor}

Magnitude range	$Z_{tor} = 0$	$Z_{tor} = 2$ km	$Z_{tor} = 4$ km
$6.5 \leq M \leq 6.75$	0.333	0.333	0.333
$6.75 < M \leq 7.0$	0.5	0.5	–
$7.0 < M$	1.0	–	–

Figure 3-2 Logic tree for faults in NW Pakistan (NWP) using the DSHA. The numbers in parentheses represent the weights assigned for each branch. AS, BA, CB, I represent Abrahamson-Silva (2008), Boore-Atkinson (2008), Campbell-Bozorgnia (2008), and Idriss (2008). The weights for the Z_{tor} are shown in the table.

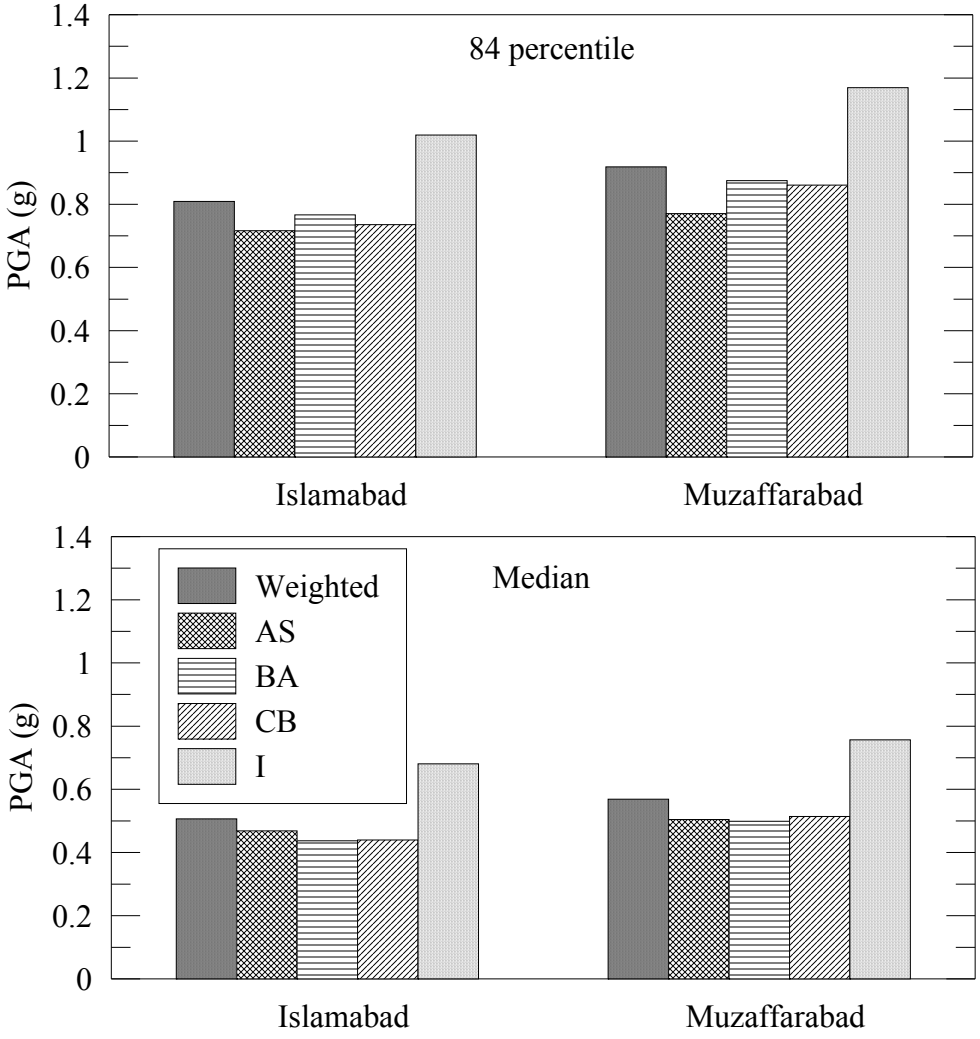

Figure 3-3 DSHA sensitivity analysis to selected attenuation relationships.

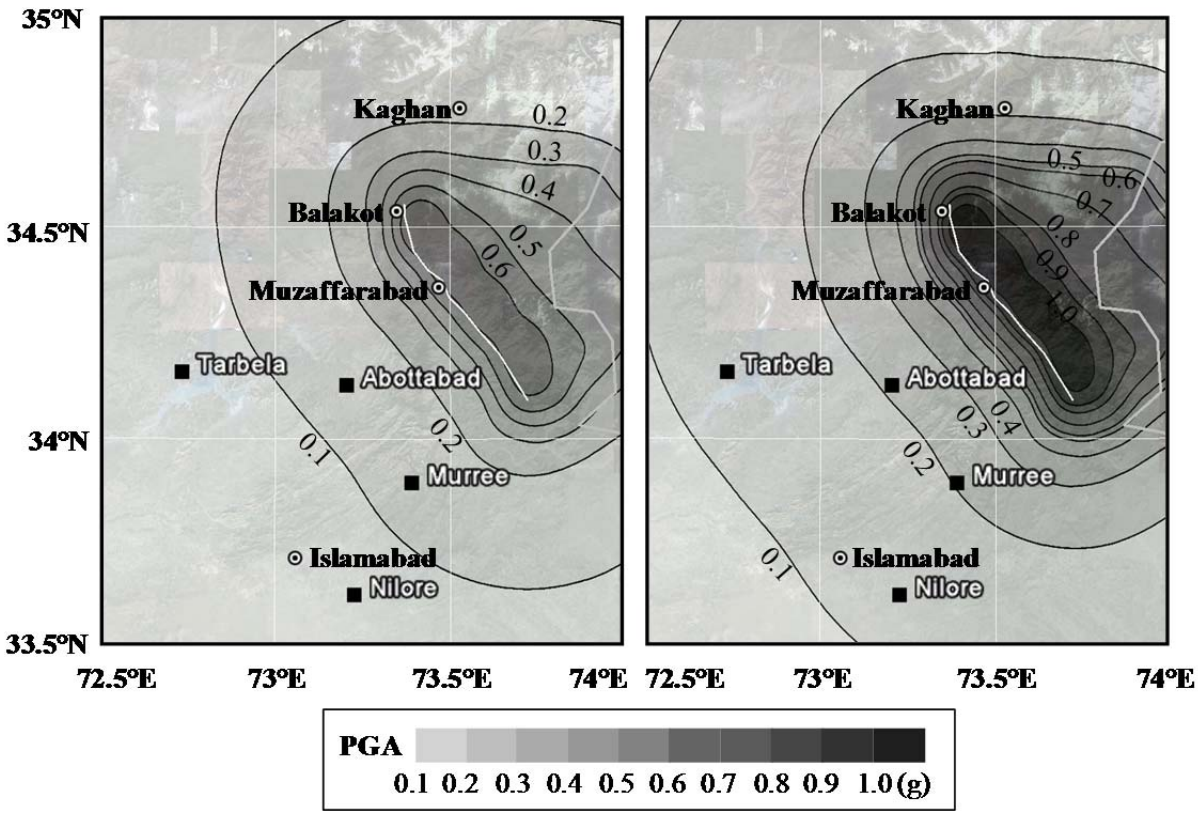

Figure 3-4 Contour maps of median PGA (left) and 84 percentile of PGA (right) for 2005 Kashmir earthquake using the DSHA procedure and $V_{s,30}$ = 760 m/sec. The grids of 0.1° × 0.1° were used. The measurement stations are shown as black squares. The white line denotes the trace of rupture zone.

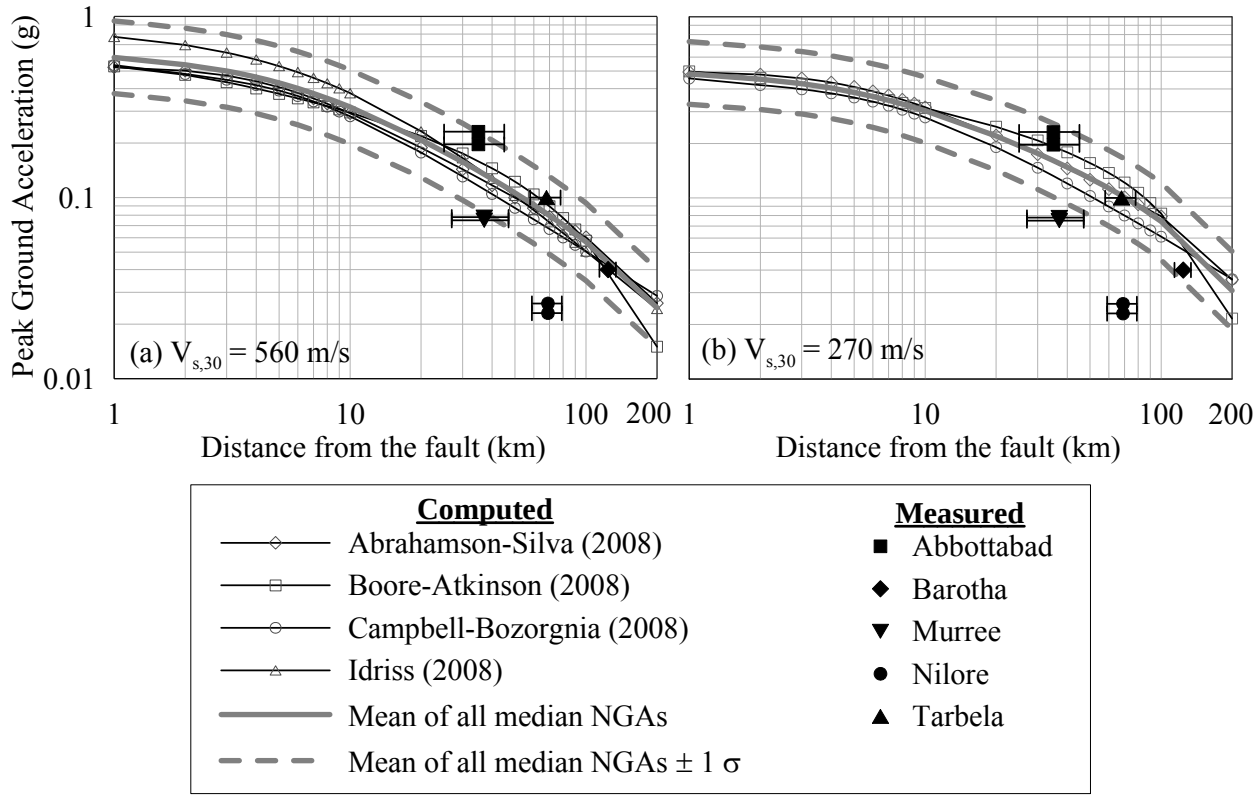

Figure 3-5 PGA prediction using DSHA for (a) very dense soil and soft rock ($V_{s,30}$ = 560 m/s) and (b) stiff soil ($V_{s,30}$ = 270 m/s), and measured strong motions (Durrani et al. 2005) during the 2005 Kashmir earthquake. Idriss (2008) is not available yet for $V_{s,30}$ < 450 m/s.

CHAPTER 4. PROBABILISTIC SEISMIC HAZARD ANALYSIS

Similar to DSHA, a typical PSHA consists of four main steps: 1) identification and characterization of earthquake source zones, 2) characterization of earthquake recurrence, 3) selection of attenuation relationships, and 4) computation of ground motion parameters corresponding to a probability of exceedance.

For the PSHA, we used the same fault geometries and attenuation relationships that were used in the DSHA. However, PSHA also requires earthquake recurrence characteristics for each fault or source. In this study, we used two common models to describe earthquake recurrence: bounded exponential magnitude distribution and characteristic earthquake distribution.

4.1 Bounded exponential distribution recurrence model

The exponential recurrence distribution was first introduced by Gutenberg and Richter (1954), which can be expressed as:

$$\log \lambda_m = a - bm \qquad \text{Eq. (2)}$$

where λ_m is the complementary cumulative earthquake rate for magnitude > m (i.e., annual rate of exceedance of magnitude m), and a and b are constants. Eq. (2) can also be expressed in exponential form as:

$$\lambda_m = \exp(\alpha - \beta m) \qquad \text{Eq. (3)}$$

where α = 2.303a and β= 2.303b.

To limit the maximum earthquake magnitude, Cornell and Vanmarcke (1969) proposed the bounded exponential recurrence, which can be expressed as:

$$\lambda_m = \nu \frac{\exp\left(-\beta\left(m - m^0\right)\right) - \exp\left(-\beta\left(m^u - m^0\right)\right)}{1 - \exp\left(-\beta\left(m^u - m^0\right)\right)} \qquad \text{for } m \le m^u \qquad \text{Eq. (4)}$$

where $\nu = \exp\left(\alpha - \beta m^0\right)$, m^0 is the threshold magnitude (m^0 = 4 in this study), and m^u is the upper bound magnitude. Thus m^0, m^u, β, and ν are the important parameters that characterize the recurrence relation for each fault.

4.1.1 Threshold magnitude, m^0, and upper bound magnitude, m^u

The m^0 defines the starting point of the recurrence relationship. If m^0 is set to be less than M_w 4.0, this will result in underestimation of recurrence because the composite catalog for Pakistan used for this study is lack of data for $M_w < 4.0$. Therefore, we set $m^0 = 4.0$. For the same reason, the previous studies (NORSAR and PMD 2006; PMD and NORSAR 2006; Monalisa et al. 2007) used the m^0 of 4.0 - 4.5.

As noted previously, we set $m^u = M_{max}$. USGS (Petersen 2008) used 0.2 magnitude unit for epistemic uncertainty, and 0.24 magnitude unit for aleatory uncertainty. Epistemic and aleatory uncertainties were combined in our analyses and a total uncertainty of 0.5 magnitude units was applied to the mean upper bound magnitude.

4.1.2 Activity rate

Activity rate, ν in Eq. (4), is the annual rate of earthquake occurrence with $m > m^0$. Activity rate for each fault is calculated by dividing the cumulative number of earthquakes occurring along each fault with $M_w > 4.0$ (starting from large magnitude and working toward

smaller magnitude) by the corresponding time period. Earthquakes with large focal depth were excluded from the analysis unless the magnitude was sufficiently large to influence the seismic hazard. Specifically, the earthquakes with focal depths > 35 km and $M_w < 5$, as well as those with focal depth > 45 km and $M_w < 6$, were excluded. Two estimates of activity rate (as explained below) were computed for each fault as shown in Table 3-3.

Figure 4-1 presents the instrumented earthquake distribution in NW Pakistan from 1960 - 2006. As discussed earlier, it is clear that the catalog is incomplete, at least for times preceding about 1972. Therefore, using the sample from entire time interval causes severe underestimation of mean rate of occurrence (λ) which can be estimated by the number of earthquakes divided by time interval (T_s). On the other hand, a reduced the time interval may not be suitable for return periods of large earthquakes due to lack of information. Therefore, it is important to determine the time interval where the mean rate of occurrence (λ) remains unchanged over time. We used the completeness analysis proposed by Stepp (1972) for three magnitude groups ($4 \leq M_w < 5$, $5 \leq M_w < 6$, and $M_w \geq 6$). He suggested that if the standard deviation of λ ($\sigma_\lambda = \sqrt{\lambda / T_s}$) is parallel to the line of $\sqrt{1/T_s}$, λ can be considered as stable for that T_s. Figure 4-2 shows the result of completeness analysis for different time intervals determined from 2006 (i.e., 2002-2006, 1997-2006, 1992-2006, etc.) The events for $4 \leq M_w < 6$ are complete during the recent 5- to 30-year interval. The departure of σ_λ from $\sqrt{1/T_s}$ after 30-year interval can be explained by incomplete reporting of earthquakes. The events for $M_w \geq 6$ are complete during the 55- to 100-year interval. The large earthquakes ($M_w \geq 6$) are much fewer than small and intermediate earthquakes ($4 \leq M_w < 6$) and do not have significant influence on estimation of activity rate. In addition, the σ_λ for these large earthquakes is slightly higher than, and parallel to the line of $\sqrt{1/T_s}$ during the 25- to 30-year interval. Therefore, we computed "Activity rate 1" for each fault using a 25-year time

interval in the earthquake catalog from 1981 to 2006 (Period 1) where the rate of occurrence for $4 \leq M_w < 6$ seems reasonably stable.

Figure 4-1 clearly shows a spike in the instrumented catalog in 2005, associated with the large number of foreshocks and aftershocks ($M_w \geq 4$) accompanying the 2005 Kashmir Earthquake. Therefore, we suspected that the foreshocks and aftershocks associated with this large event could bias the hazard calculation. Thus, we computed "Activity rate 2" for each fault using a 30-year period in the catalog from 1975 to 2004 (Period 2), excluding earthquakes associated with the 2005 Kashmir earthquake. Figure 4-3 compares activity rates 1 and 2 for the faults. Then, the earthquakes from 1981 to 2006 were declustered using the method by Gardner and Knopoff (1974). The total activity rate using these declustered earthquakes was estimated to be approximately 15.2 per year which is between two values of activity rate using Period 1 (30.7 per year) and Period 2 (9.4 per year). Therefore, we concluded that the approach using two activity rates is reasonable.

4.1.3 *b*-value

The *b*-value establishes the slope of the exponential recurrence model. Figure 4-4 shows the regression lines using Least Square (LS) method and Maximum Likelihood (ML) method (Weichert 1980) for the complementary cumulative rate of observed earthquakes from 25- to 30-year interval which was determined to be complete for $4 \leq M_w < 6$. The large magnitude range of computed recurrence model was compared with 100-year interval later in the report. Figure 4-4 also shows the line with $b = 0.8$ lines which was used for most of U.S. faults in the USGS seismic hazard mapping project (Petersen 2008). It was found that regression lines using LS and ML methods could not fit the data through all magnitude ranges. For earthquakes for Period 1 (1981-2006) in Figure 4-4 (a), the LS line can capture the overall trend of earthquake rate, but it

misses one point at the largest magnitude. On the other hand, the ML line captures the data at small magnitude range and the largest magnitude. The b = 0.8 line is similar to the ML line. For earthquakes for Period 2 (1975-2004) in Figure 4-4 (b), the ML line fails to capture the data above M_w = 4.5. The LS line fits most of data, and similar to the b = 0.8 line. For declustered earthquakes (1981-2006) in Figure 4-4 (c), the ML and LS lines are similar and fit most of data except for the largest magnitude. The b = 0.8 line is similar to ML and LS lines, but closer to the point for the largest magnitude, maintaining the best fit for small magnitude range. After all, we determined that the b = 0.8 line fits the overall earthquake data (especially for small and large magnitude range), and used that for all faults in NW Pakistan. The b-values of 0.85 and 0.80 do not result in significant difference in PGA values. For example, the PGAs with 475-year return period for Muazaffarabad using b = 0.80 and 0.85 were estimated to be 0.64g and 0.62g, respectively.

4.2 Characteristic distribution recurrence model

Youngs and Coppersmith (1985) observed that large magnitude earthquakes commonly occur at a higher rate than predicted by the exponential distribution model. This large earthquake is called characteristic earthquake. They proposed an alternate recurrence model, termed the characteristic distribution model, that combines an exponential magnitude distribution up to magnitude m' with a uniform distribution in the magnitude range of m^u - Δm_c to m^u at a rate density $\dot{n}(m_c)$. This study used the characteristic model with characteristic magnitude range, Δm_c, of 0.5 as suggested by Youngs and Coppersmith (1985) and the cumulative rate of characteristic earthquake, $\dot{N}(m_c)$, estimated by various methods which will be explained in the following

section. The upper bound magnitude was used as the characteristic magnitude for each fault. A total uncertainty of ± 0.5 magnitude units was applied to the mean characteristic magnitude.

Characteristic rate is the rate at which the characteristic earthquake occurs and is usually determined using the slip rate estimated by geodetic and geologic evidence and cosmogenic dating methods using ^{14}C, ^{3}He, or ^{10}Be, and paleoseismic data for the region. However, as discussed above, faults in NW Pakistan are not thoroughly investigated and the slip rate of each fault is not accurately known. In addition, the historical seismicity record is not long enough to include the characteristic events. Therefore, it is difficult to estimate the characteristic rate for faults in NW Pakistan. As a result, Kim et al. (2010) only employed exponential recurrence models to evaluate seismic hazard in Islamabad and Muzaffarabad. This study proposes three alternative methods to estimate characteristic rates. These three alternative characteristic rates for mean characteristic magnitude are listed for each fault in Table 3-3.

4.2.1 Characteristic rate A (relation between slip rate and characteristic rate)

The slip rates and characteristic rates for 250 faults in the Intermountain West, 60 faults in Pacific Northwest, and 151 A-type and B-type faults in California are shown in Figure 4-5. The best fit regression shown in Figure 4-5 is expressed as:

$$(Characteristic \quad rate) = 0.0008016 \times (Slip \quad rate)^{0.8988} \qquad \text{Eq. (5)}$$

The faults in NW Pakistan can be grouped into three zones according to the sense of total slip based on limited GPS measurements shown in Figure 1-2. Bendick et al. (2007) reported that velocities inferred from GPS measurements from 2001 to 2003 for observation sites near Balakot and Islamabad are approximately 52 mm/yr and 38 mm/yr, respectively. It was assumed that the

velocity of Indian Plate on the southern part of the study area and that of Eurasian Plate on the northern part of the study area are the same as observed values by Larson et al. (1999) (44 mm/year and 29 mm/year, respectively). From the difference of velocities of 29 mm/year and 52 mm/year, it can be noted that the total compression rate for Zone 1 is approximately 23 mm/year. Similarly the total extension rate for Zone 2 is about 14 mm/yr based on the diffrerence of velocities of 52 mm/year and 38 mm/years. For Zone 3, the Khair-I-Murat fault was considered as a normal fault formed by differential slip rate on its northern and southern regions based on its shape. Since the MBT west section is a thrust fault where considerable amount of compression stress occurs, the two velocities of 44 and 40 mm/year were assumed on the northern and southern parts of the Khair-I-Murat fault , respectively. These assumed velocities give compressional slip rates of 4 mm/year to MBT west section and 2 mm/year to Khairabad Fault , and extentional slip rate of 4 mm/year to the Khair-I-Murat Fault . The total slip rate for the rest of faults in Zone 3 is then 4 mm/year from the difference of the measured velocity (44 mm/year) and the assumed velocity (40 mm/year).

Then the total slip rate for each zone was distributed to individual fault based on the assumption that the slip rate is proportion to the fault length. Once the characteristic rate for the mean characteristic magnitude is estimated, the characteristic rates for the mean characteristic magnitude ± 0.5 magnitude units are calculated based on the relationship between return period and magnitude proposed by Slemmons (1982). Based on Slemmons (1982), the rate for the mean characteristic magnitude + 0.5 magnitude unit is 0.47 times that for mean characteristic magnitude, and the rate for the mean characteristic magnitude – 0.5 magnitude unit is 2.12 time that for mean characteristic magnitude.

4.2.2 Characteristic rate B (relation between activity rate and characteristic rate)

The second method that we employed was to assume that the characteristic rate is proportional to the activity rate of each fault. To estimate the overall characteristic rate, the earthquakes with $M_w > 6.5$ with a 100-year period (1907-2006) for NW Pakistan were considered since the large earthquakes ($M_w \geq 6.0$) were determined to be complete for the last 100 years from the completeness analysis. Total earthquake rate for $M_w > 6.5$ was estimate to be approximately 0.03 (per year) as shown in Figure 4-6. Then the overall characteristic rate was distributed to fault proportional to the activity rate of faults. Because two different activity rate sets (Activity rate 1 and Activity rate 2) were used, there are also two characteristic rate B sets. The average of two sets is used in the analysis.

4.2.3 Characteristic rate C (seismic moment balance method)

Many researchers including the USGS use the seismic moment balance method to estimate the characteristic rate of the faults. Aki (1966) proposed the relationship between seismic moment of earthquake and average displacement of the fault.

$$M_0 = \mu(RA)d \qquad \text{Eq. (6)}$$

where μ is the rigidity which is usually taken to be 3×10^{11} dyne/cm^2, and d is the average displacement over the slip surface.

The average displacement can be also expressed as $S \times T$ where S is the average seismic slip rate and T is the recurrence interval. Then the characteristic rate can be calculated.

$$(Characteristic \quad rate) = \frac{1}{T} = \frac{\mu(RA)S}{M_0} \qquad \text{Eq. (7)}$$

Seismic moment can be estimated by earthquake magnitude for California by Hanks and Kanamori (1979).

$$\log M_0 = 1.5M_w + 16.1 \qquad \text{Eq. (8)}$$

Once the characteristic magnitude is obtained based on the magnitude-rupture area relationships, the characteristic rate can be calculated using the equation with the estimated rupture area and slip rate.

4.3 Total recurrence

Using all parameters mentioned above, the recurrence models for individual faults were established. Figure 4-6 presents the total recurrence model, i.e, the sum of all recurrence models for individual faults in NW Pakistan. The weighted average of activity rates, characteristic rates, and R-factors were used to construct this total recurrence. The complementary cumulative rate of earthquake event in various time periods and areas were compared with the total recurrence as shown in Figure 4-6. For small magnitude range, the total recurrence rates are comparable with the observed earthquake rates. They slightly overestimate the middle magnitude range, but fit well the data for magnitude around 6.5 M_w. This phenomenon can be also observed in the fault recurrence model for Northern California (WGCEP 2008). The total recurrence rates for large earthquake range computed based on 25- to 30-year interval are also consistent with observed earthquake rate using 100-year interval.

The large earthquakes for entire Pakistan and for NW Pakistan with two different time intervals (1907-2006 and 1505-2006) were compared in Figure 4-6. The large earthquakes in

NW Pakistan in both time periods of 1907-2006 and 1505-2006 match with the mean upper bound magnitude – 0.5 magnitude unit. The large earthquakes in entire Pakistan match with the mean upper bound magnitude + 0.5 magnitude unit. The earthquake rate for entire Pakistan is higher than that for NW Pakistan because the larger area contains more earthquakes. Overall, the total recurrence model is in good agreement with the seismicity data in Pakistan.

4.4 Logic Trees for PSHA

Figure 4-7 show the logic tree for the PSHA. The same branches for fault geometry, R-factor, and attenuation relationships as in the DSHA were used in the PSHA. The weight of 0.6 was assigned to mean upper bound magnitude and 0.2 to mean upper bound magnitude ± 0.5 units. For the recurrence models, the characteristic model was weighted at 2/3 and bounded exponential model was weighted at 1/3. These weights were selected because there is increasing evidence that the characteristic recurrence relationship captures the earthquake rate of individual fault better than the exponential recurrence relationship (Youngs and Coppersmith 1985). The two sets of activity rates for the bounded exponential recurrence model were equally weighted. Weights of 0.25 were assigned to the proposed Characteristic rates A and B, and a weight of 0.5 was assigned to Characteristic rate C, the commonly-used moment balance method.

4.5 PSHA sensitivity analysis

Sensitivity analyses for two parameters in the PSHA logic tree, earthquake rate and upper bound magnitude, were performed to evaluate the influence of these on the seismic hazard. The sensitivity analysis for earthquake rate is shown in Figure 4-8. The results are shown for 975-year return period which represents intermediate values for 475- and 2475-year return periods. For Islamabad, the seismic hazard analysis with the characteristic rate A yields the highest PGA. The PGA estimated only with activity rate 1 is significantly high for Muzaffarabad, while that

for Islamabad is almost same with that estimated only with activity rate 2. Activity rate 1 is includes the numerous aftershocks of 2005 Kashmir earthquake. Therefore the activity rate 1 for the faults near Muzaffarabad is greater than the activity rate 2. On the other hand, there is no significant difference between activity rate 1 and activity rate 2 of faults near Islamabad.

The sensitivity of mean upper bound magnitude and mean upper bound magnitude ± 0.5 magnitude units is investigated in Figure 4-9. It is notable that the greater magnitudes yields lower PGAs because the characteristic rates were adjusted according to the magnitude. In that, the smaller characteristic rates were assigned to the larger magnitudes because the earthquake with larger magnitude tends to occur less frequently. The weighted average value is close to that computed using the mean magnitude value.

4.6 Evaluation of the proposed PSHA procedure

Figure 4-10 shows the contour map of PGAs with 475- and 2475-year return periods over the same area evaluated with the DSHA. The proposed PSHA procedure was used to generate this contour map with $V_{s,30}$ = 760 m/sec. For Muzaffarabad, the PGAs with 475- and 2475-year return periods are approximately 0.6 g and 1.0 g, respectively, which are consistent with median PGA and 84 percentile of PGA, respectively, obtained from DSHA of 2005 Kashmir earthquake in Section 3.7. This observation is also true for the case of Balakot.

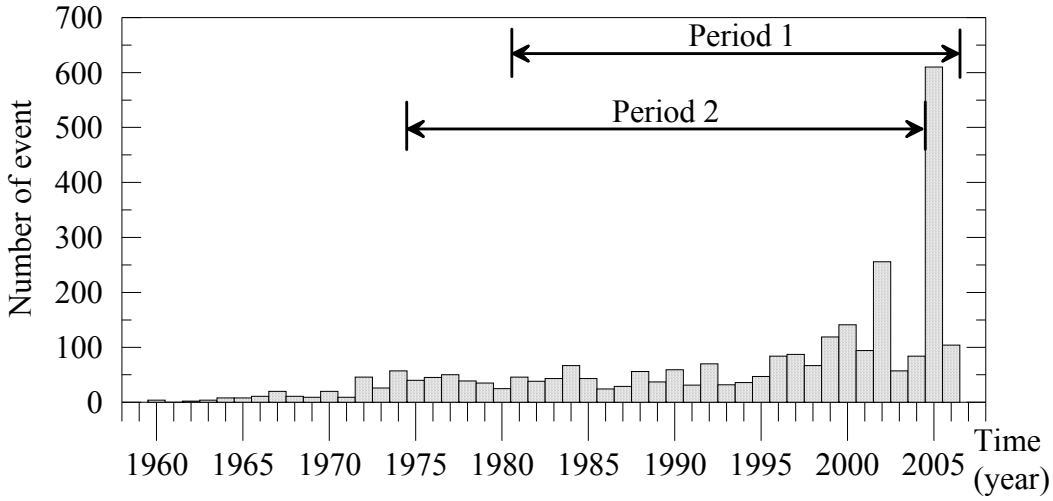

Figure 4-1 Earthquake distribution (31.5°N-36°N, 69.5°E-75.5°E) as a function of time. Two different periods were considered to construct the earthquake recurrence of faults. Period 1 is from 1981 to 2006 and the Period 2 is from 1975 to 2004.

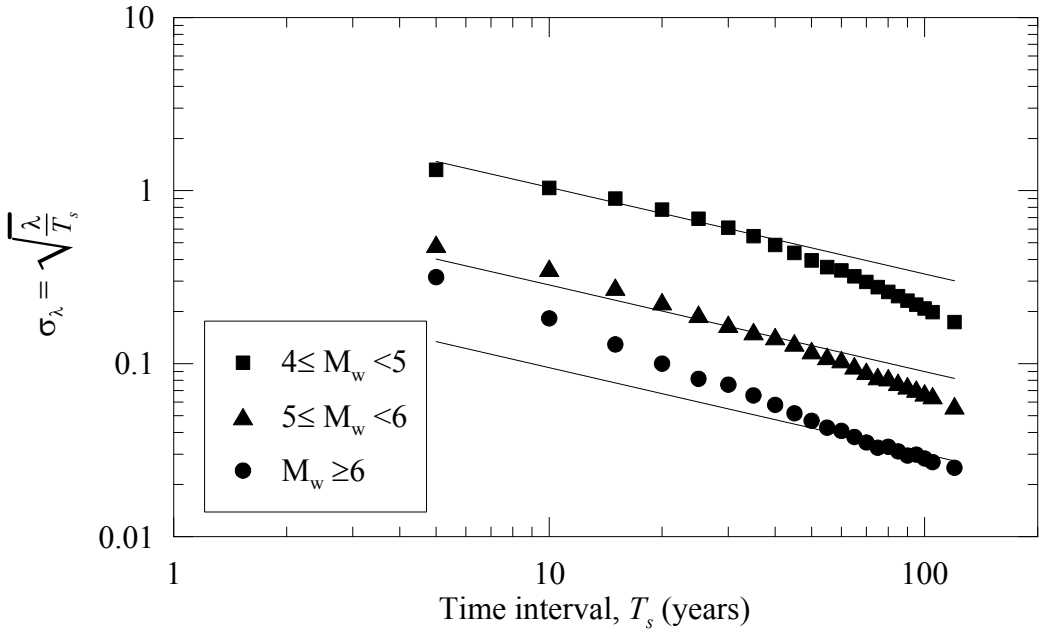

Figure 4-2 Completeness analysis for NW Pakistan for different magnitude classes using Stepp (1972) method. σ_λ = standard deviation, λ = rate of earthquake occurrence, and T_s = time interval. The solid lines are parallel to $1/\sqrt{T_s}$.

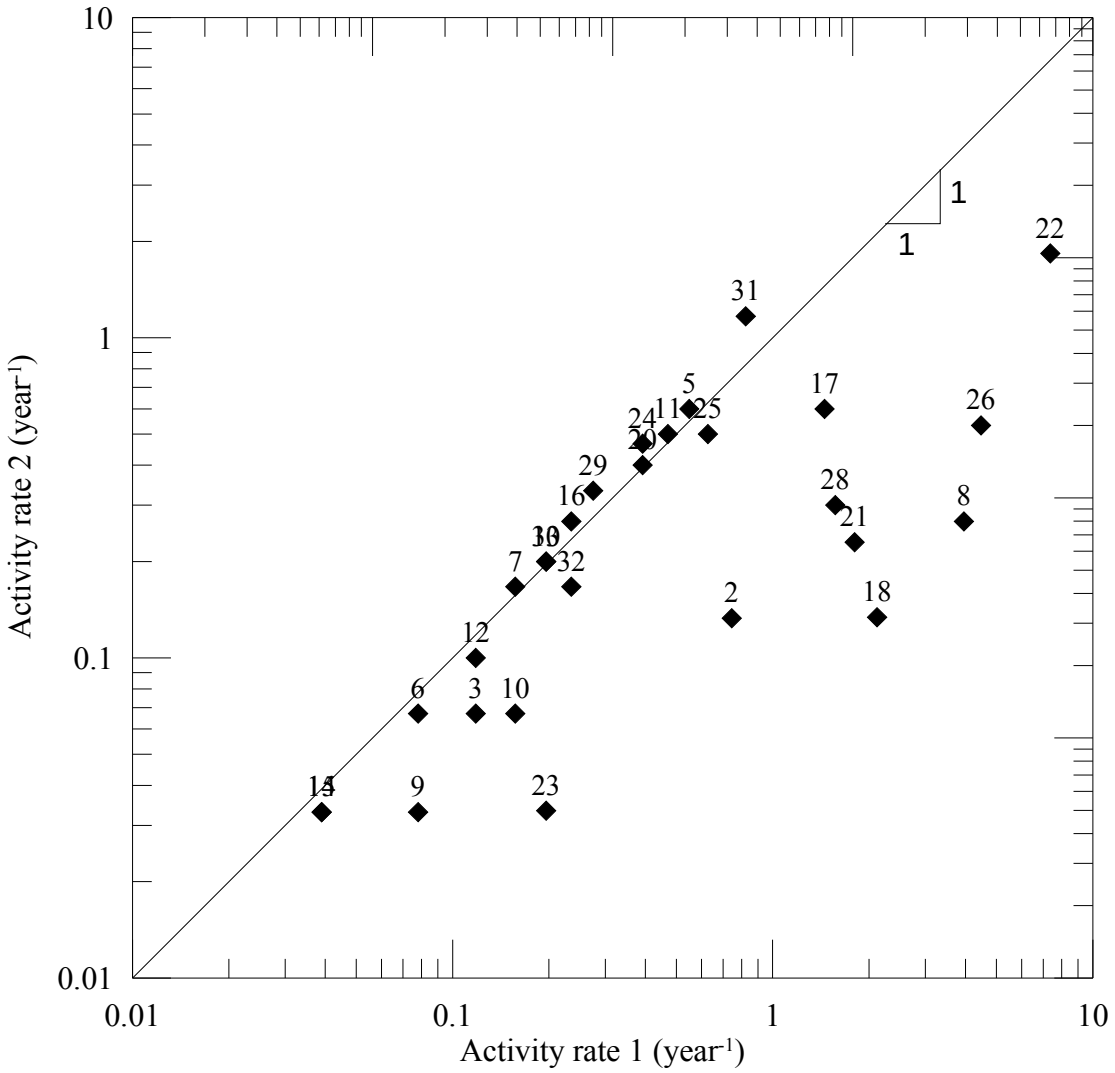

Figure 4-3 Comparison of fault activity rates (Activity rate 1:1982 to 2006; and Activity rate 2: 1975 to 2004). Numbers represent the fault number used in this study.

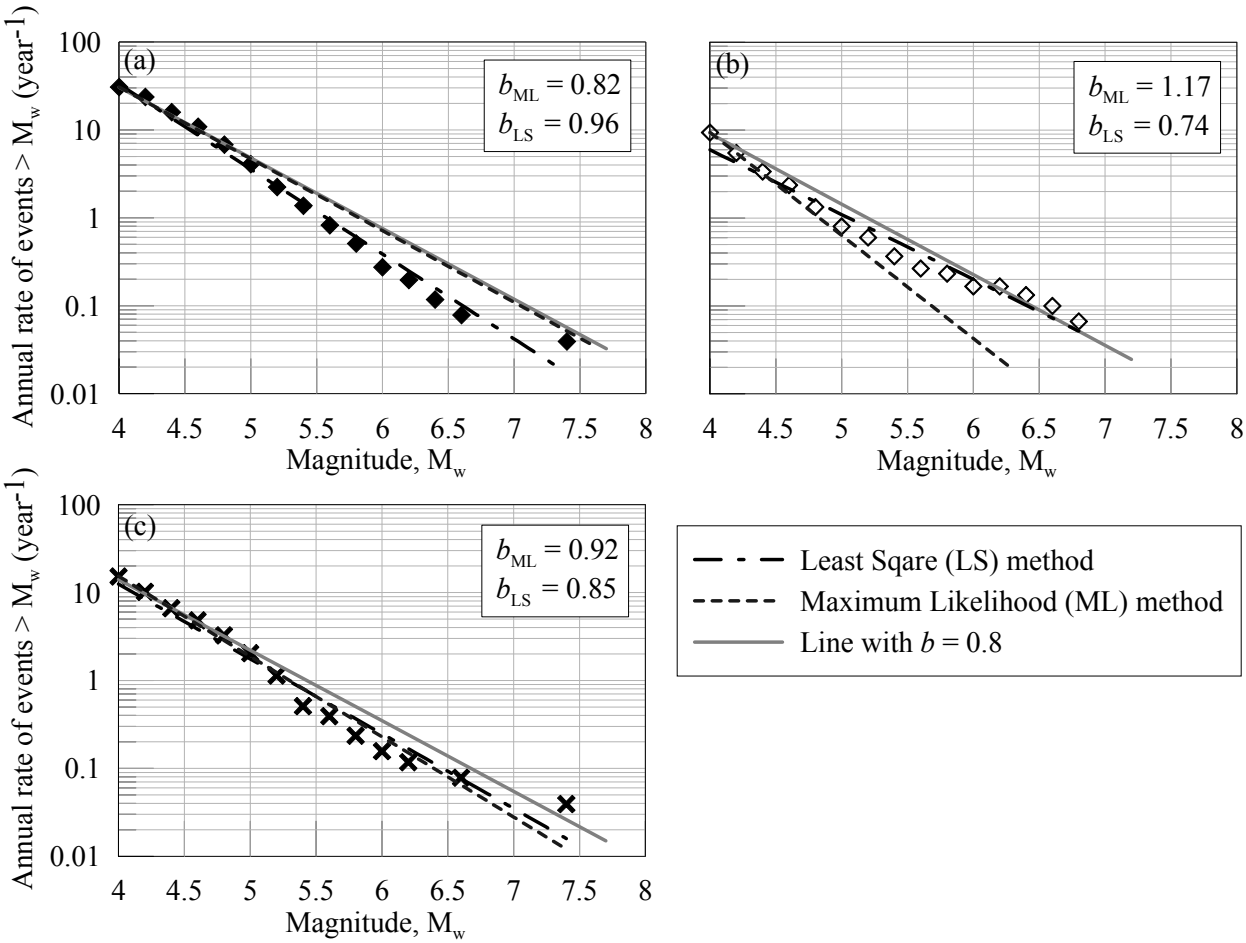

Figure 4-4 Regression lines using Least Square (LS) method and Maximum Likelihood (Bhat et al.) method (Weichert 1980) for the complementary cumulative rate of observed earthquakes for (a) Period 1 (1981-2006), (b) Period 2 (1975-2004), and (c) declustered catalog (1981-2006). The b = 0.8 line starting from annual earthquake rate at M_w=4 for each case is also shown.

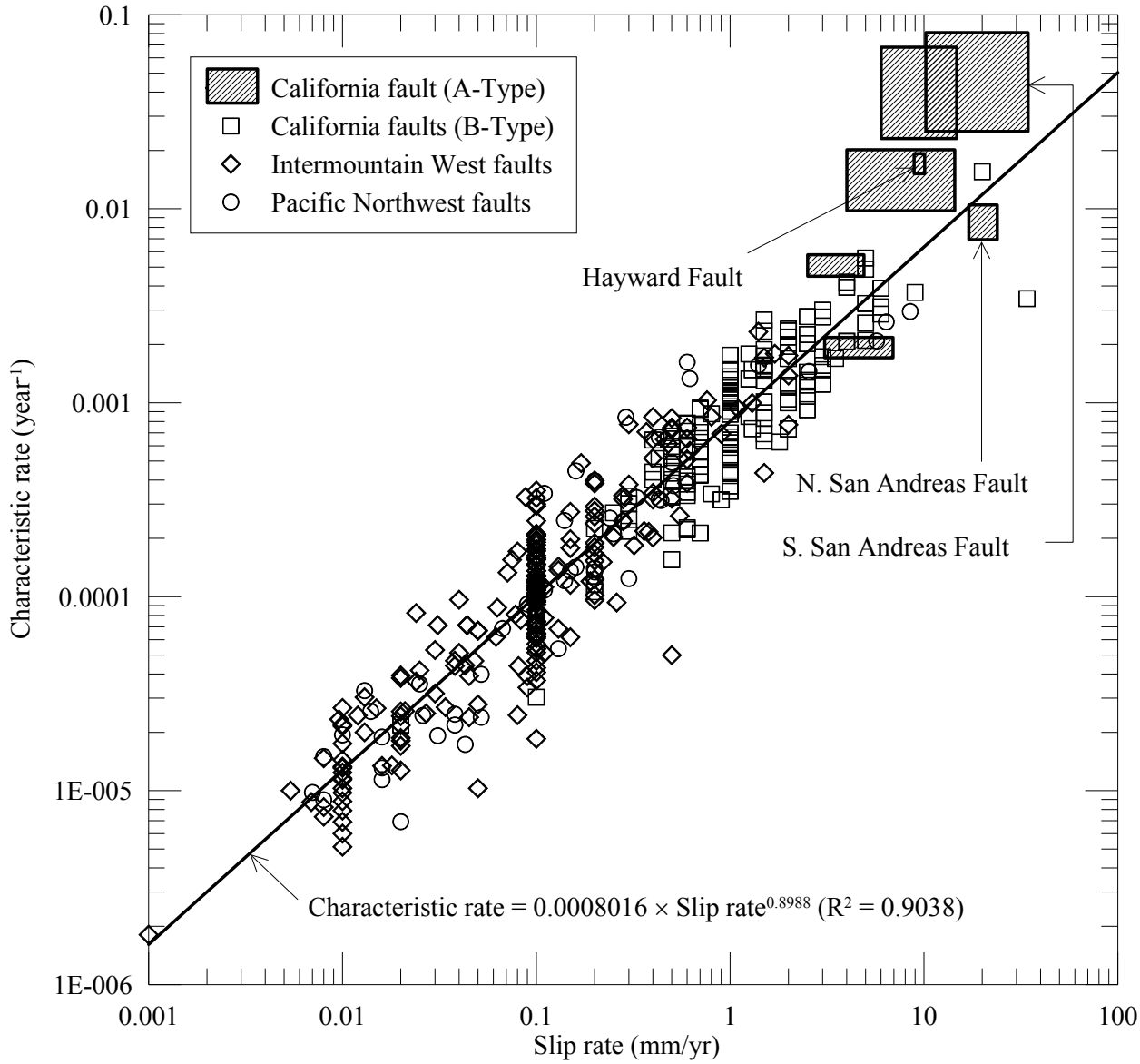

Figure 4-5 Relationship between slip rates and characteristic rates of U.S faults. A-type faults in California are divided into several segments which have various slip rate. The characteristic rates for these faults were calculated using three methods (A-priori, Ellsworth, and Hanks and Bakun) used by WGCEP (2008). Boxes are used to illustrate uncertainties in slip rates and characteristic rates for these faults.

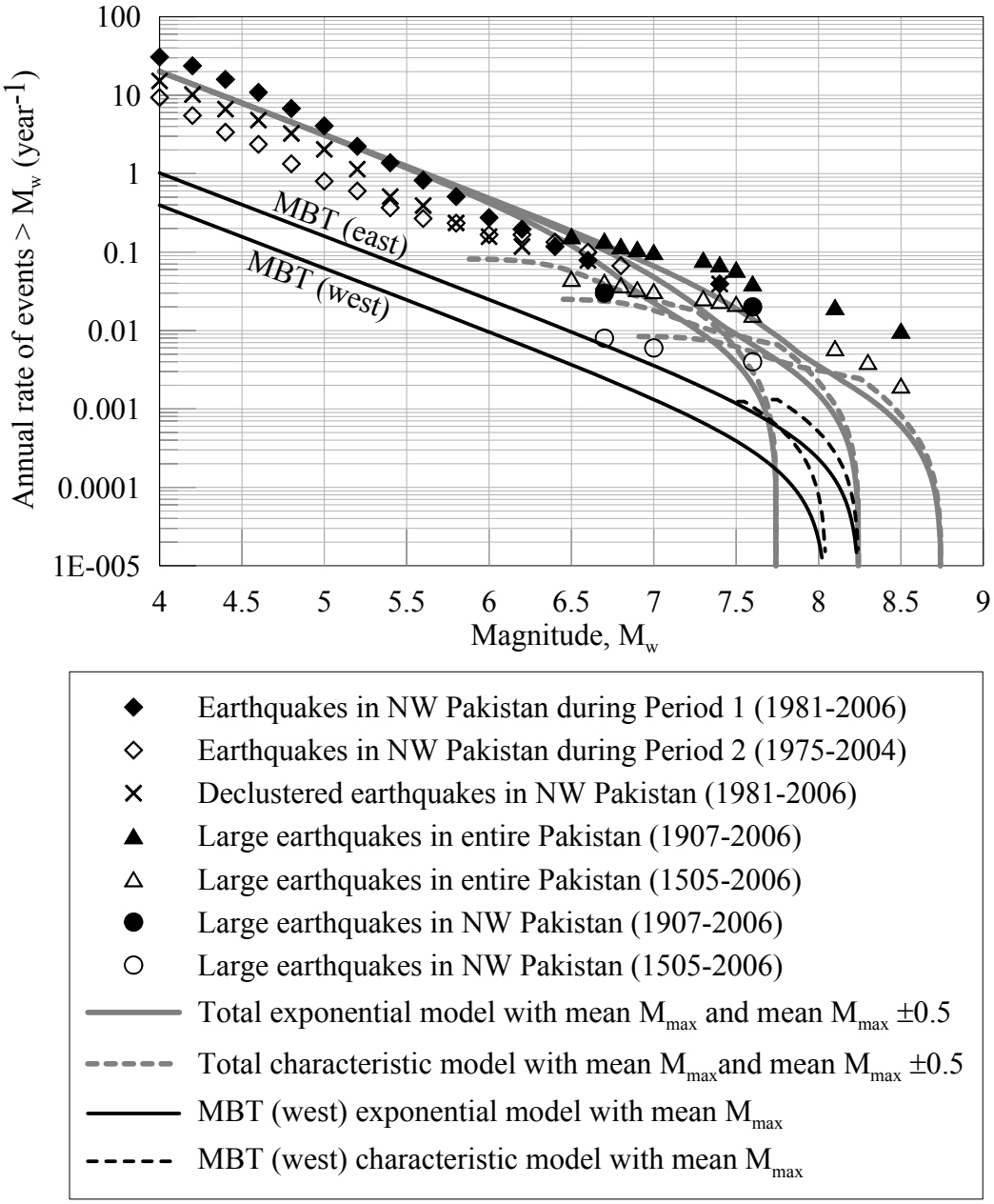

Figure 4-6 The complementary cumulative rate of observed earthquakes and recurrence models from the composite catalog used in this study. Total recurrence models are sum of all recurrence models of faults. The recurrence models of MBT are shown as examples.

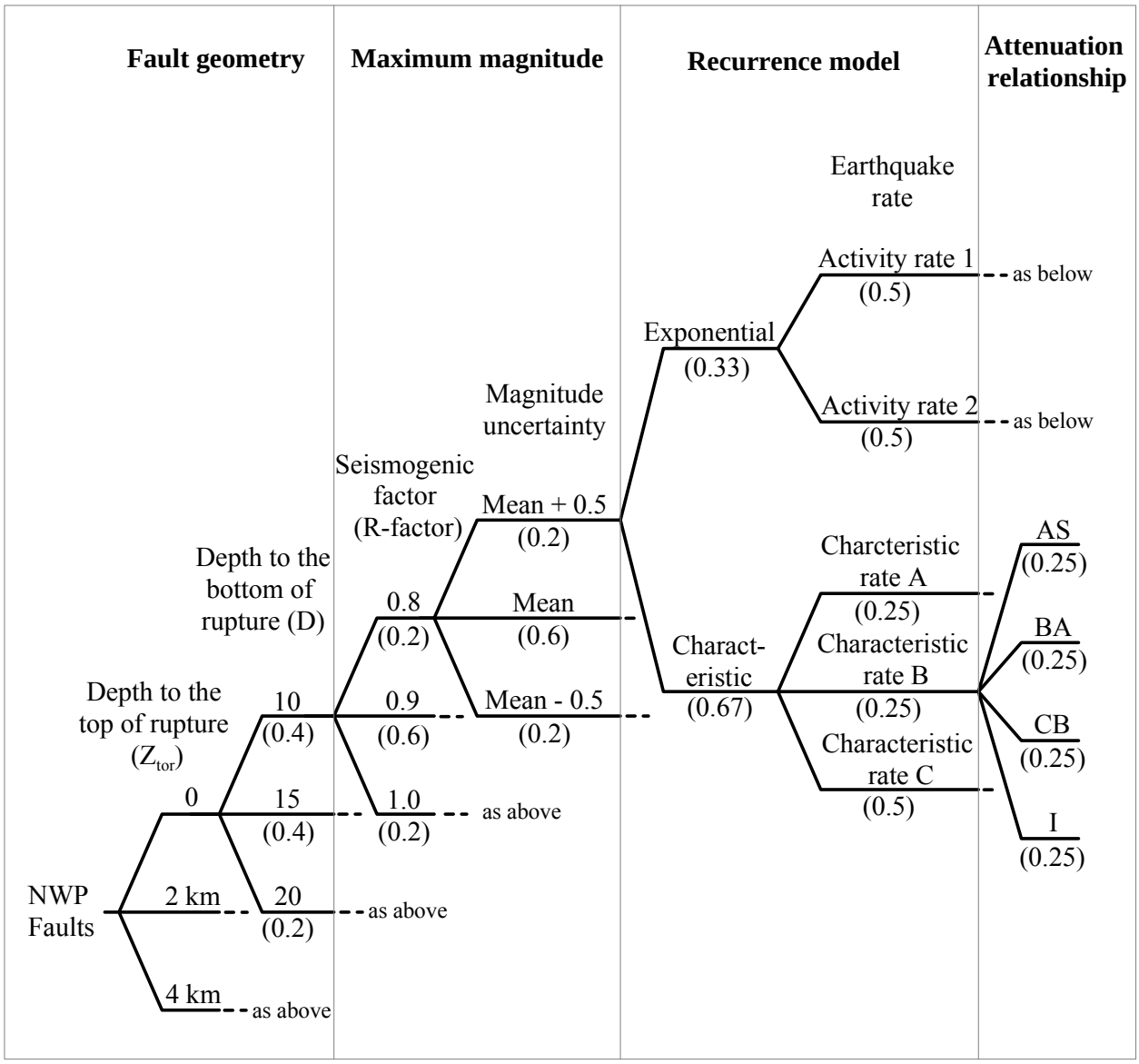

Figure 4-7 Logic tree for faults in NW Pakistan using the PSHA. Numbers in parentheses represent weights assigned to each branch. The weights for Z_{tor} are same as DSHA.

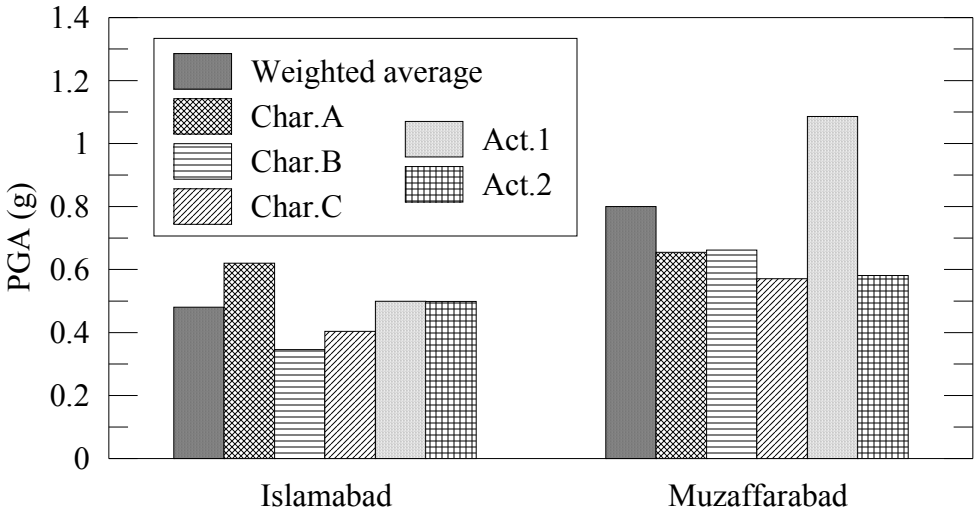

Figure 4-8 PSHA sensitivity analysis for characteristic rates and activity rates with 975-year return period. All other parameters are used with weights described in the logic tree.

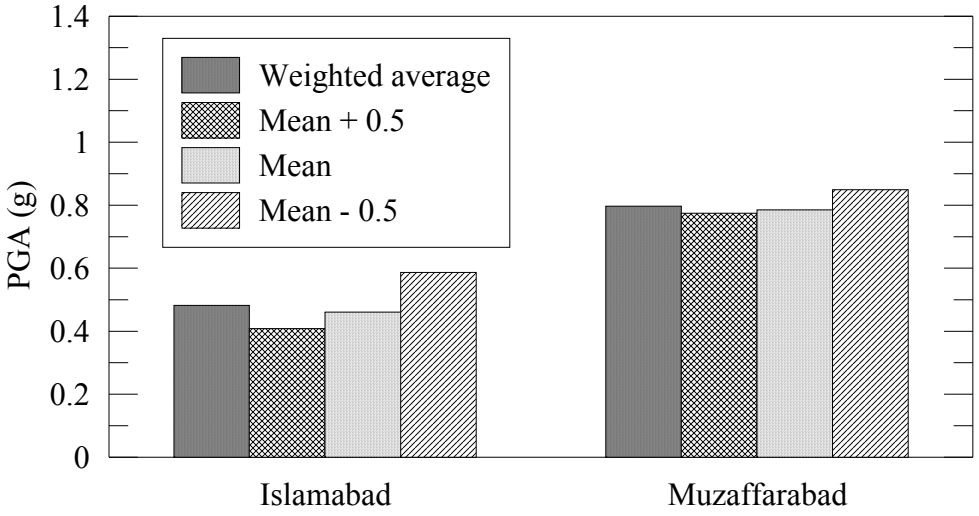

Figure 4-9 PSHA sensitivity analysis for upper bound magnitudes with 975-year return period. All other parameters are used with weights described in the logic tree.

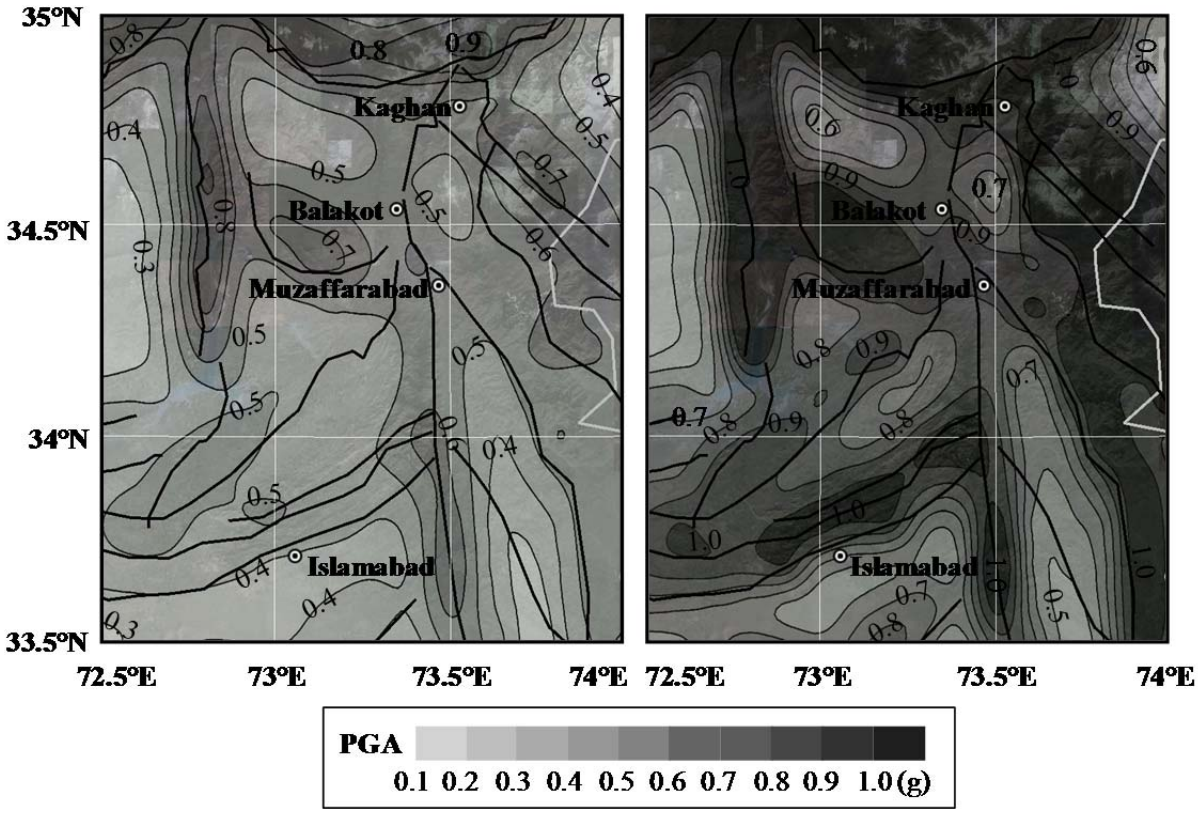

Figure 4-10 Contour maps of PGAs with 475- (left) and 2475-year (right) return periods using the PSHA procedure and $V_{s,30}$ = 760 m/sec. The grids of 0.1° × 0.1° were used.

CHAPTER 5. SEISMIC HAZARD RESULTS

Using the procedures described in this report, PSHA hazard curves, PSHA uniform hazard spectra, and DSHA spectra at 5% damping were developed for the 11 cities for an assumed bedrock with $V_{s,30}$ of 760 m/sec. The site effects should be separately considered by performing site response analysis or by applying site coefficients. Here, we present the results for Islamabad, Kaghan, Muzaffarabad, and Peshawar. From the uniform hazard curves, the annual frequency of exceedance for given peak horizontal ground acceleration (PGA) can be estimated. This and other spectral accelerations are commonly estimated for probabilities of exceedance (PE) of 10%, 5%, and 2% in 50 years, corresponding to return periods of 475, 975, and 2475 years, respectively.

5.1 Islamabad

Figure 5-1 presents the seismic hazard curves and select response spectra for Islamabad. Hazard curves for the top five contributing faults are included. The PGAs corresponding to 475-, 975-, and 2475-year return periods are approximately 0.35g, 0.48g, and 0.69g, respectively. The hazard curves illustrate that the MBT west section contributes the most to the hazard at most commonly-employed return periods. This fault located closer to the city than any other fault, exhibits high activity rate, and has a large M_{max}. Response spectra (Figure 5-1b) can be used to evaluate structural response at different natural periods. The SA is highest at T = 0.2 sec (1.73g for a 2475-year return period), while at T = 1.0 sec, SA is estimated to be 0.67g for 2475-year return period, which is similar to the PGA value.

Deaggregation of seismic hazard for Islamabad was conducted for the maximum amplitude of PGA and SAs (at T = 0.2 sec and 1.0 sec) for 475-year return period as shown in Figure 5-2. Deaggregation provides the relative contribution of hazard from each fault (i.e.,

seismic source) in terms of magnitude, source-to-site distance, R, and ground motion uncertainty, ε. The magnitude bin width is 0.2 M_w units, and the distance bin width is 5 km units. The mean and modal values of M, R, and ε that correspond to a given maximum amplitude can be calculated from deaggregation analysis. Mean values of M and R are commonly used to represent the controlling earthquake size and location for developing site-specific time histories (Bernreuter 1992; U.S. Department of Energy (U.S. DOE) 1996; U.S. Nuclear Regulatory Commission (U.S. NRC) 1997). The mean values of M, R, and ε for Islamabad are shown in Table 5-1. These mean values of M and R can be used to develop conditional mean spectra (discussed in a later section), and perform liquefaction analyses or pseudo-static slope stability analyses, etc. Modal values are used to select the controlling earthquake when a site is proximate to two equally hazardous faults (Bazzurro and Cornell 1999).

For Islamabad, large earthquakes on the nearby MBT west section dominate the hazard. There is a small contribution from more distant faults for T = 1.0 sec. Deaggregation for 975-and 2475-year return periods shows the similar trend.

The DSHA spectrum (Figure 5-1b) was constructed for the controlling fault (MBT west section) determined by deaggregation. The median DSHA spectrum is comparable to the UHS for a 975-year return period, and the 84th percentile DSHA spectrum is higher than the UHS for a 2475-year return period.

5.2 Muzaffarabad

The seismic hazard results for Muzaffarabad are shown in Figure 5-3. As shown in the PSHA hazard curve, PGAs corresponding to 475-, 975-, and 2475-year return periods are 0.64g, 0.80g, and 1.02g, respectively. These PGAs are greater than those for Islamabad due to proximity to more faults with higher activity rate and larger M_{max}. It can be noted that the Jhelum

fault contributes most to the hazard. The highest spectral acceleration is 2.70g at a period of 0.2 sec for a 2475-year return period.

The deaggregation results for the maximum amplitude of PGA and SAs (at T = 0.2 sec and 1.0 sec) for 475-year return period for Muzaffarabad is shown in Figure 5-4. Similar to Islamabad, large earthquakes on the nearby faults dominate the hazard at all return periods and spectral periods. There is a small contribution from more distant faults for T = 1.0 sec. Mean values of M, R, and ε for Muzaffarabad are shown in Table 5-1.

DSHA spectra were also constructed for Muzaffarabad using the controlling Riasi thrust. Overall, the median DSHA spectrum is similar to the 475-year return period UHS (particularly for T > 0.5 sec), while the 84th percentile DSHA spectrum ranges from the 975-year to the 2475-year return period UHS.

5.3 Kaghan

The seismic hazard results for Kaghan are shown in Figure 5-5. The PGAs for 475-, 975-, and 2475-year return periods are estimated to be 0.58g, 0.75g, and 1.00g, respectively. These values are comparable with those for Muzaffarabad. The MCT fault contributes significantly to the hazard at PGA greater than 0.4g. For smaller PGAs, the MMT and the Balakot Shear Zone contribute most to hazard. The UHS for the 2475-year return period yields spectral accelerations of 2.67g and 1.06g at T = 0.2 sec and 1.0 sec, respectively. The 84th percentile DSHA spectrum is in good agreement with UHS for a 2475-year return period, while the median DSHA spectrum falls between UHS for 475- and 975-year return periods.

5.4 Peshawar

The PGAs for 475-, 975-, and 2475-year return periods for Peshawar were estimated to be 0.21g, 0.28g, and 0.38g, respectively, from the hazard curve in Figure 5-6. These PGAs are

considerably smaller than Islamabad, Muzaffarabad, and Kaghan mainly because of the larger source-to-site distances for Peshawar. The MBT west section and Hissartang Fault are the two primary contributing faults (Figure 5-6a). The MBT west section contributes slightly more to hazard despite a larger source-to-site distance because it exhibits a larger M_{max} and higher activity rate than the Hissartan Fault. The SAs at T = 0.2 sec and 1.0 sec for a 2475-year return period are 1.01g and 0.42g, respectively. The median and 84th percentile DSHA spectra are comparable to the UHS for 475- and 2475-year return periods, respectively.

5.5 Summary of seismic hazard analyses for eleven NW Pakistan cities

Figure 5-7 compares spectral accelerations at T = 0.01 sec (PGA), 0.2 sec, and 1.0 sec computed using both DSHA and PSHA for 11 cities in NW Pakistan for an assumed bedrock outcrop with $V_{s,30}$ = 760 m/sec. The highest ground accelerations are estimated to occur in Kaghan and Muzaffarabad, with PGAs for a 2475-year return period exceeding 1.0g as a result of their proximity to major active faults. Although Islamabad and Kohat are both approximately 5 km away from the MBT west section, the PGAs for these cities are not as high as Kaghan and Muzaffarabad, because they are located on the foot wall side of the faults. Astor, Bannu, Malakand, Mangla, Peshawar, and Talagang are located much farther from significant faults; therefore, PGAs for these cities are considerably lower. Accelerations estimated by DSHA are comparable to those from PSHA. In general, median accelerations agree well with those corresponding to 475- or 975-year return periods, while the 84th percentile accelerations are comparable to those corresponding to the 2475-year return period. The PSHA hazard curves, PSHA uniform hazard spectra, and DSHA hazard spectra for the rest of cities are shown in Figure 5-8 through Figure 5-14.

5.6 Comparison with previous studies

Figure 5-15 compares PGAs corresponding to a 475-year return period from PSHA and median PGAs from DSHA with those computed in previous studies (PMD and NORSAR 2006; Monalisa et al. 2007). This comparison clearly illustrates the differences in computed seismic hazard using individual faults and using area sources or diffused seismicity for the cities close to active faults (e.g., Islamabad, Kaghan, Kohat, and Muzaffarabad). However, the differences are smaller for the cities located far from the active faults. For example at Astor, Monalisa et al. (2007) and PMD and NORSAR (2006) computed PGAs of 0.08g for a 475-year return period and 0.28g for a 500-year return period, respectively. This study yielded similar PGAs; 0.21g for a 475-year return period from PSHA, and median PGA of 0.21g from DSHA because only a few faults exist near this city and distance between most controlling fault (MMT) and the city is approximately 24 km.

Monalisa et al. (2007) and PMD and NORSAR (2006) both predicted the smallest PGA for Bannu (0.07g and 0.08g, respectively). Although the faults near this city have low activity rates, these PGA values appear too small because the city is less than 10 km from an active fault. In contrast, we computed a PGA of 0.16g for a 475-year return period from the PSHA and a median PGA of 0.30g from the DSHA. Similarly, Islamabad is located less than 5 km from the MBT west section, one of the most hazardous faults in NW Pakistan. Previous studies predicted very small PGAs for this city; 0.13g by Monalisa et al. (2007) and 0.20g by PMD and NORSAR (2006). In contrast, we computed PGA = 0.35g for a 475-year return period and median PGA = 0.51g for Islamabad by the PSHA and DSHA, respectively.

As additional examples, Monalisa et al. (2007) and PMD and NORSAR (2006) computed PGAs of 0.11g and 0.20g for Kaghan, despite the city being surrounded by several active faults

with high activity rates. In contrast, we computed the highest PGAs for this city, with a PGA = 0.58g for 475-year return period (PSHA) and a median PGA = 0.72g (DSHA). Similarly, Monalisa et al. (2007) and PMD and NORSAR (2006) computed PGAs of 0.21g and 0.13g, respectively, for Kohat. However, this city, like Islamabad, is located adjacent to the MBT west section. Therefore, this study computed much larger PGAs, similar to those for Islamabad.

Lastly, Muzaffarabad is located close to the epicenter of the 2005 Kashmir earthquake, and experienced severe damage during that earthquake. Moreover, this city is proximate to several active faults including the MBT, MCT, and Jhelum fault. Despite this, Monalisa et al. (2007) and PMD and NORSAR (2006) computed the PGAs of 0.12g and 0.20g, respectively, for Muzaffarabad. In contrast, this study computed much larger PGAs; 0.64g with 475-year return period by PSHA and median PGA of 0.54g by DSHA that compare reasonably with those measured in 2005. These values are also comparable with the deterministic prediction (0.66g) by Durrani et al. (2005), using the attenuation relationship by Ambraseys et al. (2005). Only in cities located farther from mapped faults (Malakand, Mangla, Peshawar, and Talagang), the PGAs computed in this study compare reasonably with those computed by Monalisa et al. (2007) and PMD and NORSAR (2006).

In summary, PGAs estimated in this study using individual faults show distinct differences among cities located at variable source-to-site distances, in contrast to previous studies that used areal source zones and computed PGAs that rarely exceeded 0.2 g and showed little differences among cities. As anticipated, PGAs computed for cities located far from faults (e.g., Astor, Malakand, Mangla, Peshawar, and Talagang) are similar to or slightly higher than those computed using areal source zones. In contrast, PGAs computed for cities located close to faults (e.g., Islamabad, Kaghan, Kohat, and Muzaffarabad) are 2 to 4 times greater than those

predicted by previous studies using areal source zones.

5.7 Hazard maps

Seismic hazard maps for NW Pakistan were produced using PSHA for an assumed bedrock condition with $V_{s,30}$ = 760 m/s (NEHRP B/C boundary) on a 0.1° × 0.1° grid. Figure 5-16 through Figure 5-18 provide seismic hazard maps of PGA for 475-, 975-, and 2475-year return periods, respectively. As higher ground accelerations are expected along the active faults, the hazard map shows contours enveloping the faults. As anticipated, the contours are wider on the hanging wall side of reverse and normal faults because higher ground accelerations are predicted on the hanging wall side than on the footwall side. The largest PGAs (> 0.8g for a 475-year return period) are predicted along the MMT. The next highest PGAs are observed along the MBT east section (greater than 0.6 g) and the MBT west section (greater than 0.4g). The PGAs are computed to be relatively low near the southern faults, including the Kurram Thrust and Salt Range Thrust because of their low activity rate.

Figure 5-19 through Figure 5-24 provide seismic hazard maps for SAs (T = 0.2 sec and 1.0 sec). These maps show trends similar to PGA, with the largest SAs occurring along the MMT. These values exceed 2.0g, 2.8g, and 4.0g at T = 0.2 sec for 475-, 975-, and 2475-year return periods, respectively. The hazard maps for SA at T = 1.0 sec are similar to those for PGA, with the largest SAs values occurring along the MMT.

Table 5-1 Mean magnitude and distance from deaggregation for Islamabad and Muzaffarabad. For Islamabad, all earthquakes correspond to the MBT fault, and for Muzaffarabad, all earthquakes correspond to the Riasi thrust.

Return period (years)	Period (sec)	Islamabad			Muzaffarabad		
		Mean magnitude (M_w)	Mean distance (km)	Mean epsilon	Mean magnitude (M_w)	Mean distance (km)	Mean epsilon
475	0.05	6.8	11	0.53	6.1	4.8	1.38
	0.2	6.9	11	0.53	6.4	5.1	1.25
	1.0	7.3	22	0.51	7.1	9.4	0.95
975	0.05	7.0	8.1	0.72	6.2	4.4	1.64
	0.2	7.1	8.7	0.71	6.5	4.4	1.54
	1.0	7.4	14	0.67	7.1	7.6	1.22
2475	0.05	7.2	6.5	1.09	6.3	4.0	1.96
	0.2	7.2	6.7	1.07	6.5	3.9	1.86
	1.0	7.5	8.8	0.98	7.1	6.1	1.55

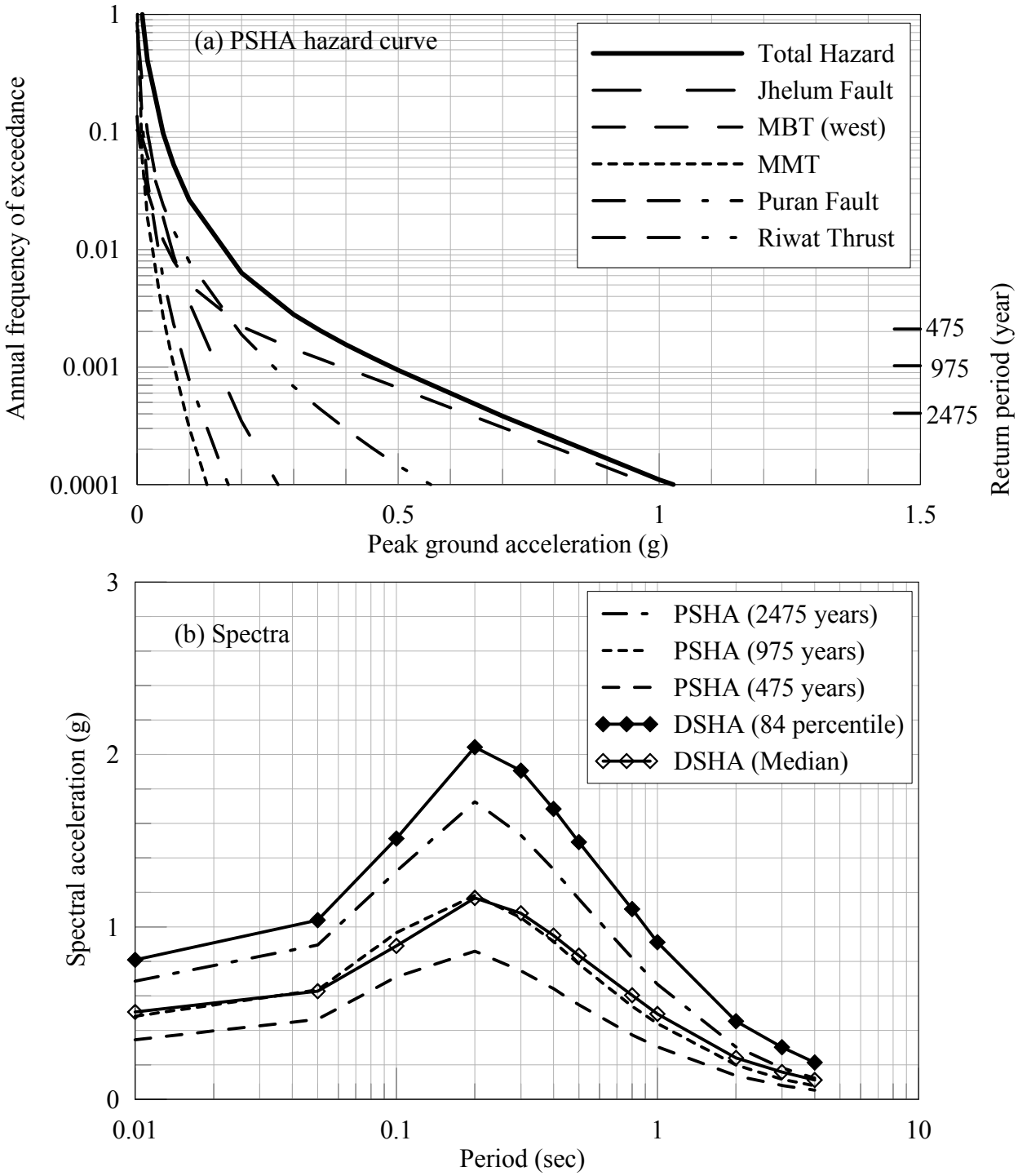

Figure 5-1 Seismic hazard analysis results for Islamabad for an assumed bedrock with $V_{s,30}$ of 760 m/sec. (a) PSHA hazard curves for PGA at 5% damping. The hazards by the top five contributing faults are shown; (b) PSHA uniform hazard spectra (UHS) and DSHA hazard spectra.

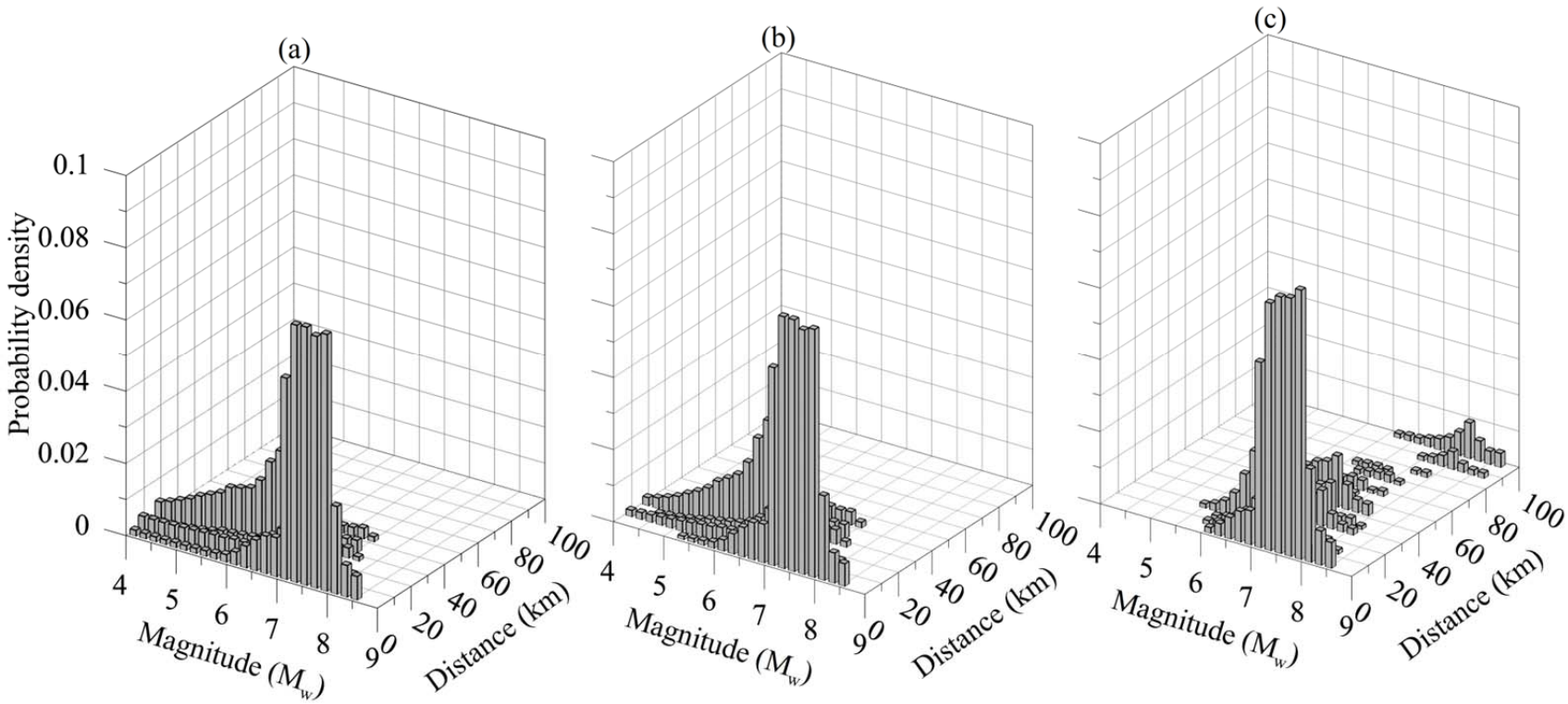

Figure 5-2 Deaggregation of seismic hazard for Islamabad for 475-year return period at three spectral periods of (a) 0.05 sec, (b) 0.2 sec, and (c) 1.0 sec.

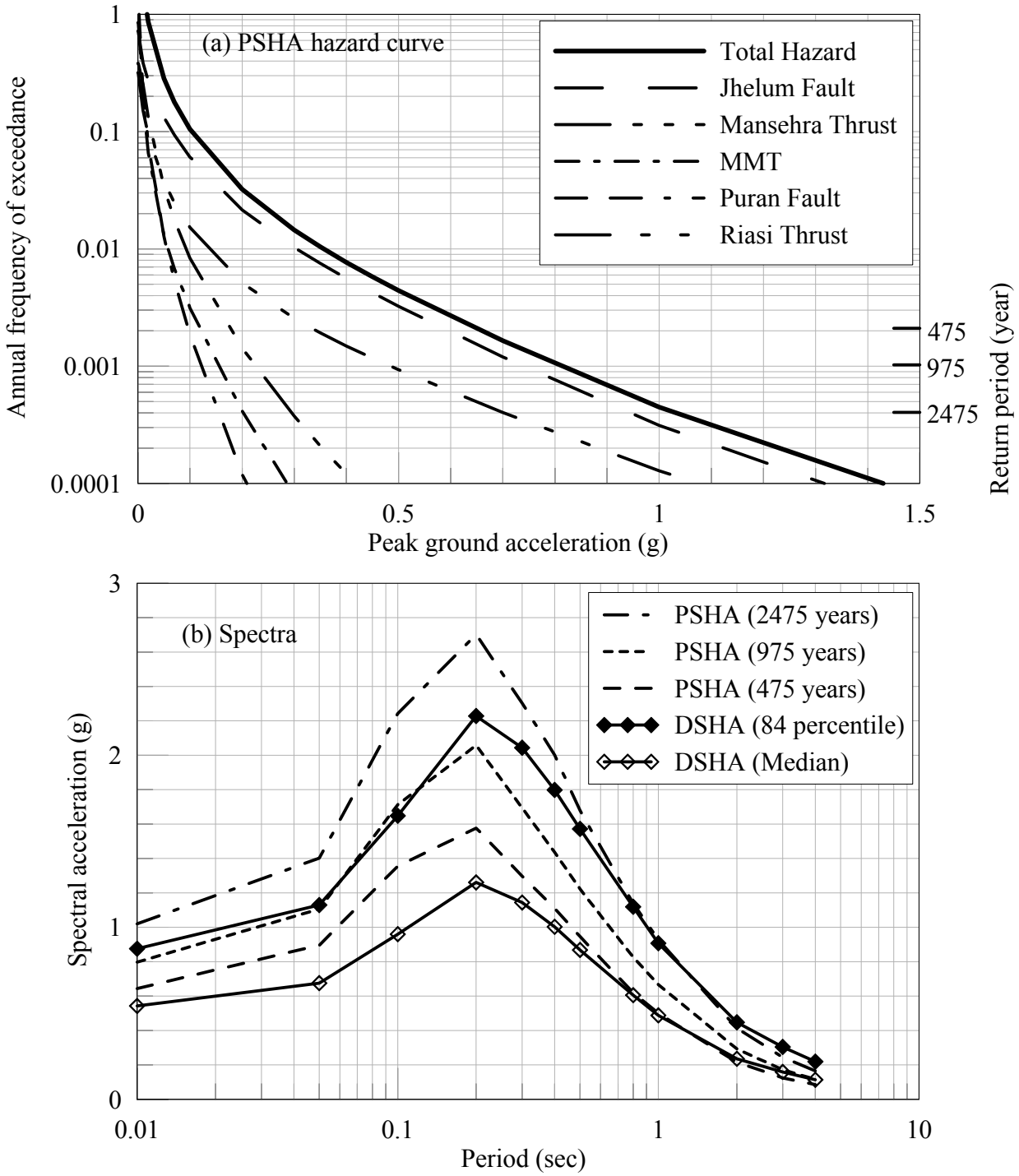

Figure 5-3 Seismic hazard analysis results for Muzaffarabad for an assumed bedrock with $V_{s,30}$ of 760 m/sec. (a) PSHA hazard curves for PGA at 5% damping. The hazards by the top five contributing faults are shown; (b) PSHA uniform hazard spectra (UHS) and DSHA hazard spectra.

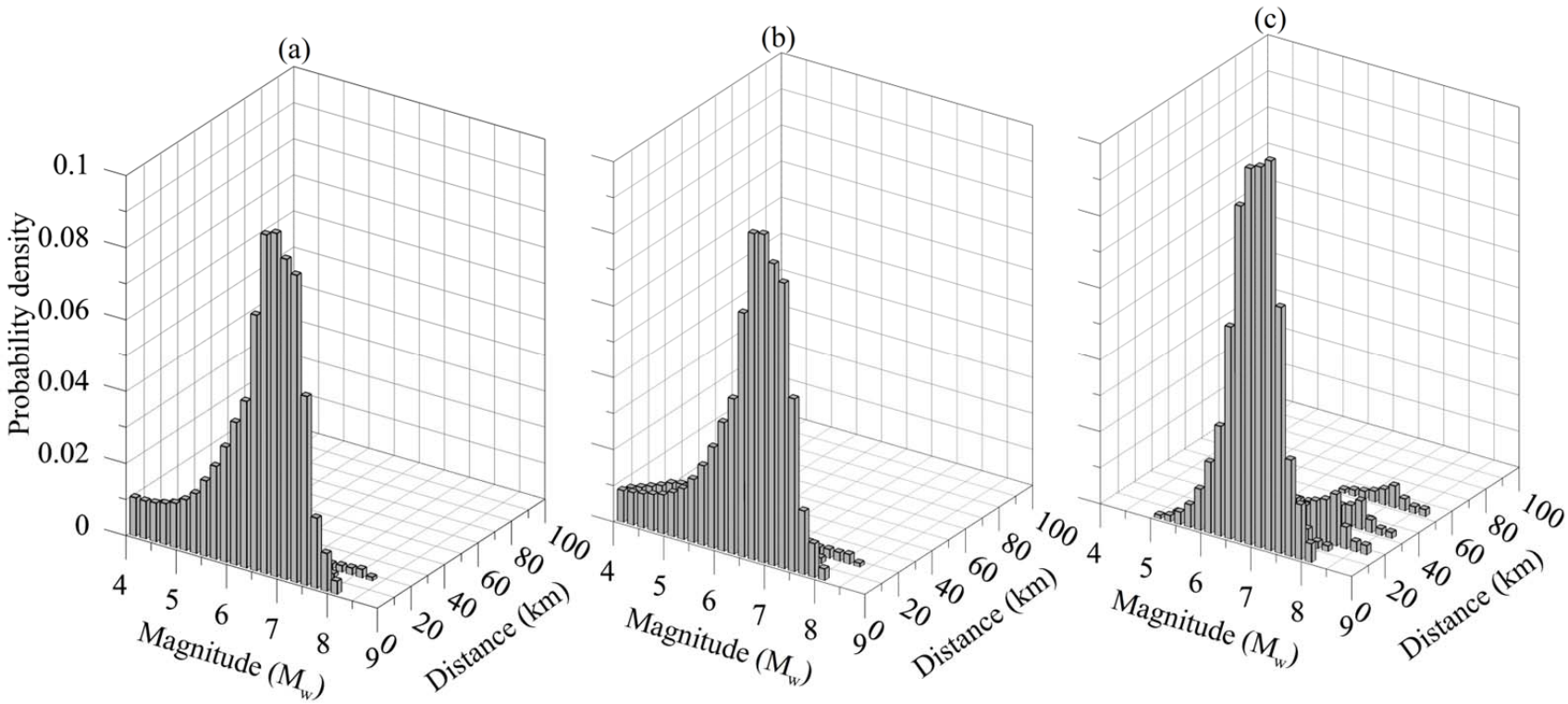

Figure 5-4 Deaggregation of seismic hazard for Muzaffarabad for 475-year return period at three spectral periods of (a) 0.05 sec, (b) 0.2 sec, and (c) 1.0 sec.

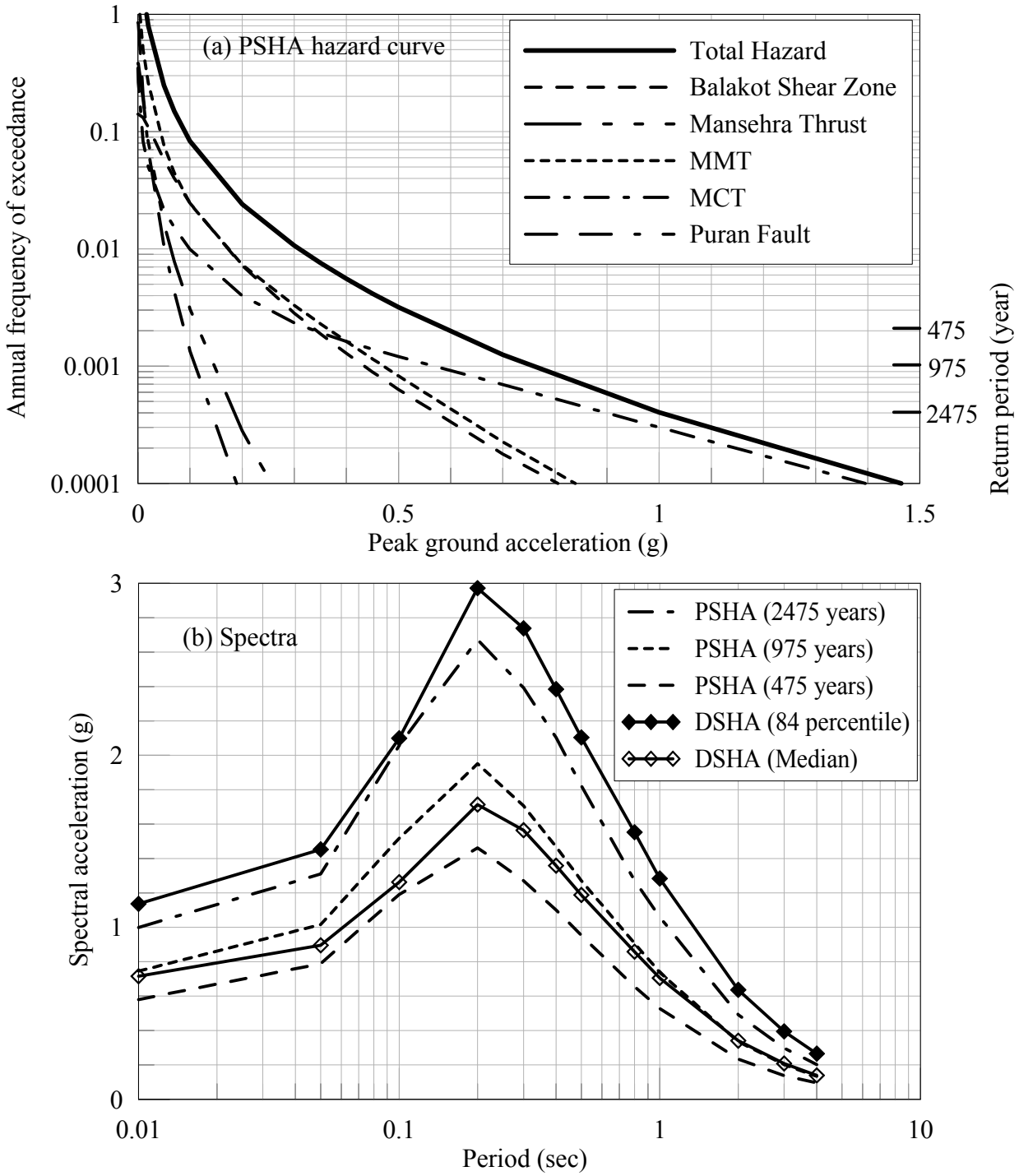

Figure 5-5 Seismic hazard analysis results for Kaghan for an assumed bedrock with $V_{s,30}$ of 760 m/sec. (a) PSHA hazard curves for PGA at 5% damping. The hazards by the top five contributing faults are shown; (b) PSHA uniform hazard spectra (UHS) and DSHA hazard spectra.

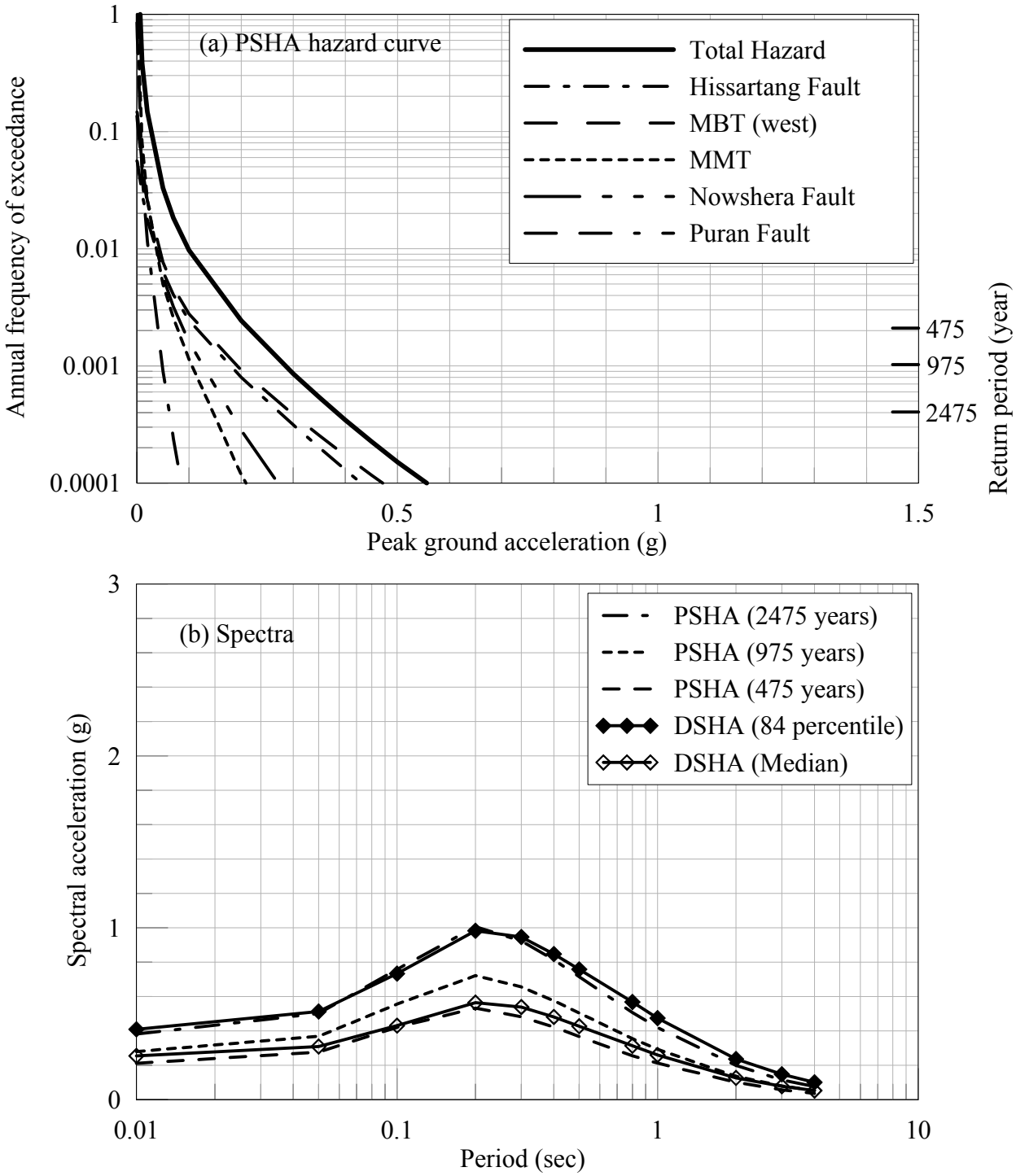

Figure 5-6 Seismic hazard result for Peshawar for an assumed bedrock with $V_{s,30}$ of 760 m/sec. (a) PSHA hazard curves for PGA at 5% damping. The hazards by the top five contributing faults are shown; (b) PSHA uniform hazard spectra (UHS) and DSHA hazard spectra.

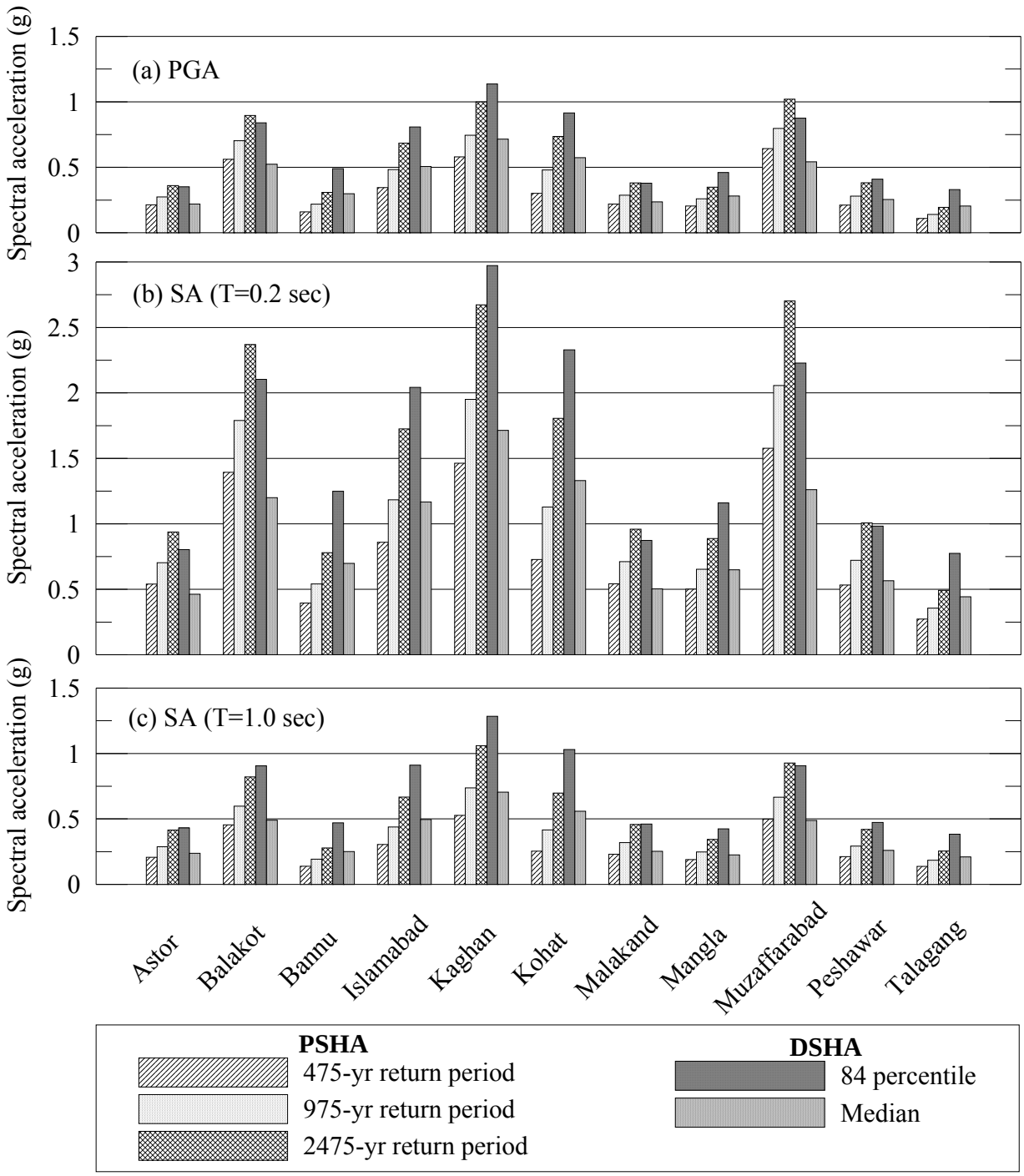

Figure 5-7 Comparisons of spectral accelerations computed by PSHA at 475-, 975-, and 2475-year return periods with median and 84th percentile spectral accelerations computed by DSHA for 11 cities in NW Pakistan for an assumed bedrock with $V_{s,30}$ of 760 m/sec. (a) PGA; (b) SA (T = 0.2 sec); and (c) SA (T = 1.0 sec)

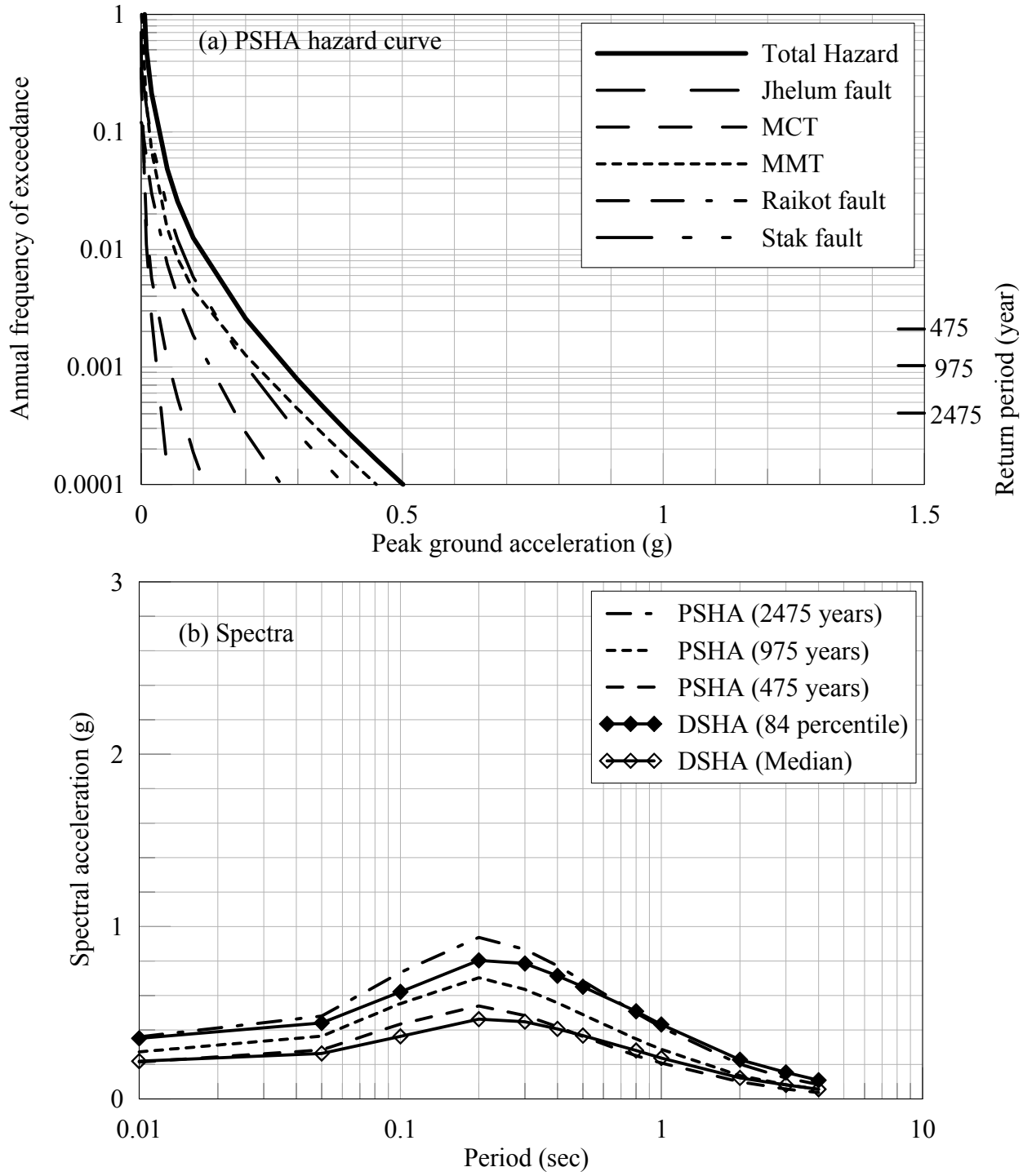

Figure 5-8 Seismic hazard result for Astor for an assumed bedrock with $V_{s,30}$ of 760 m/sec. (a) PSHA hazard curves for PGA at 5% damping. The hazards by the top five contributing faults are shown; (b) PSHA uniform hazard spectra (UHS) and DSHA hazard spectra.

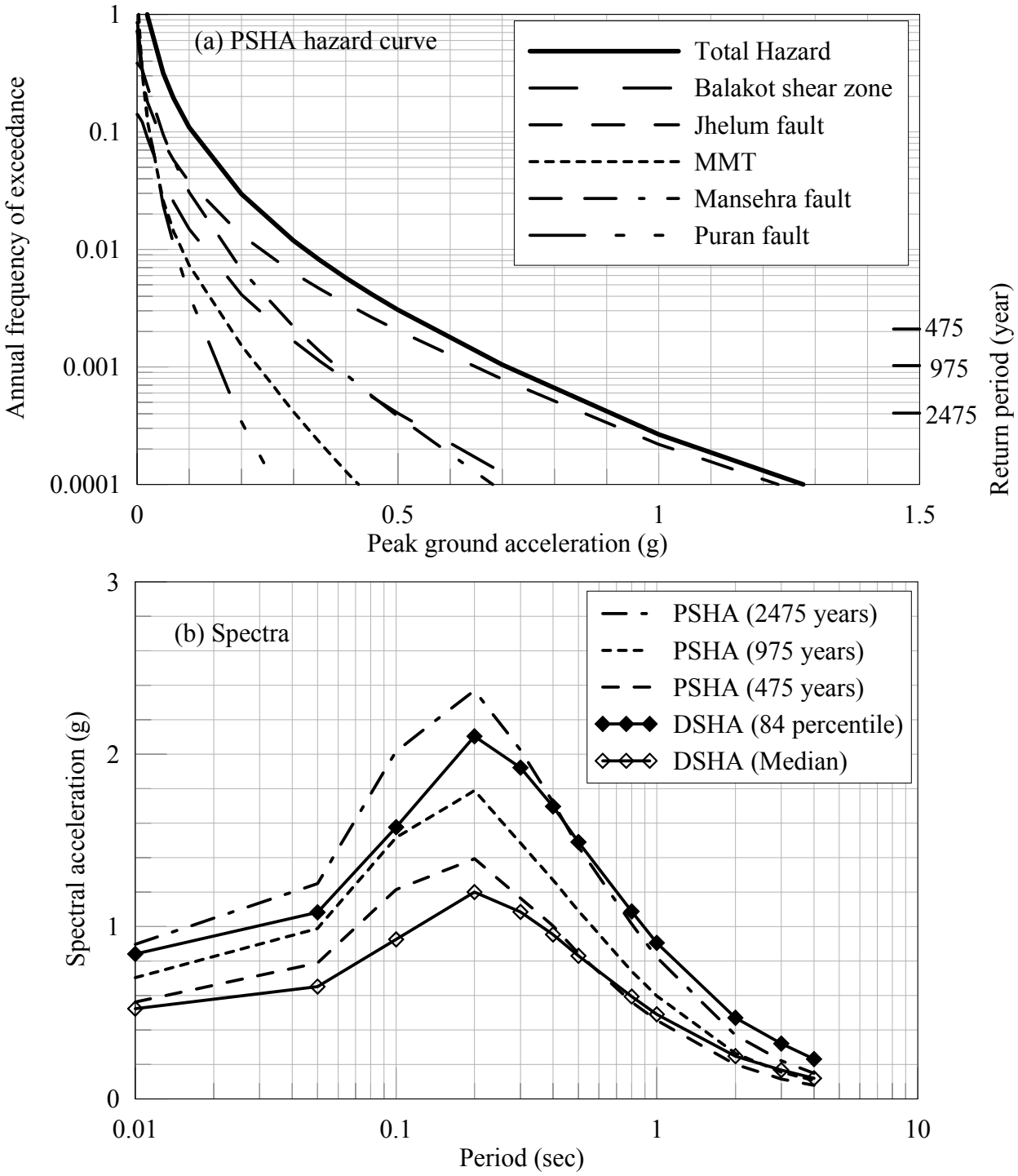

Figure 5-9 Seismic hazard result for Balakot for an assumed bedrock with $V_{s,30}$ of 760 m/sec. (a) PSHA hazard curves for PGA at 5% damping. The hazards by the top five contributing faults are shown; (b) PSHA uniform hazard spectra (UHS) and DSHA hazard spectra.

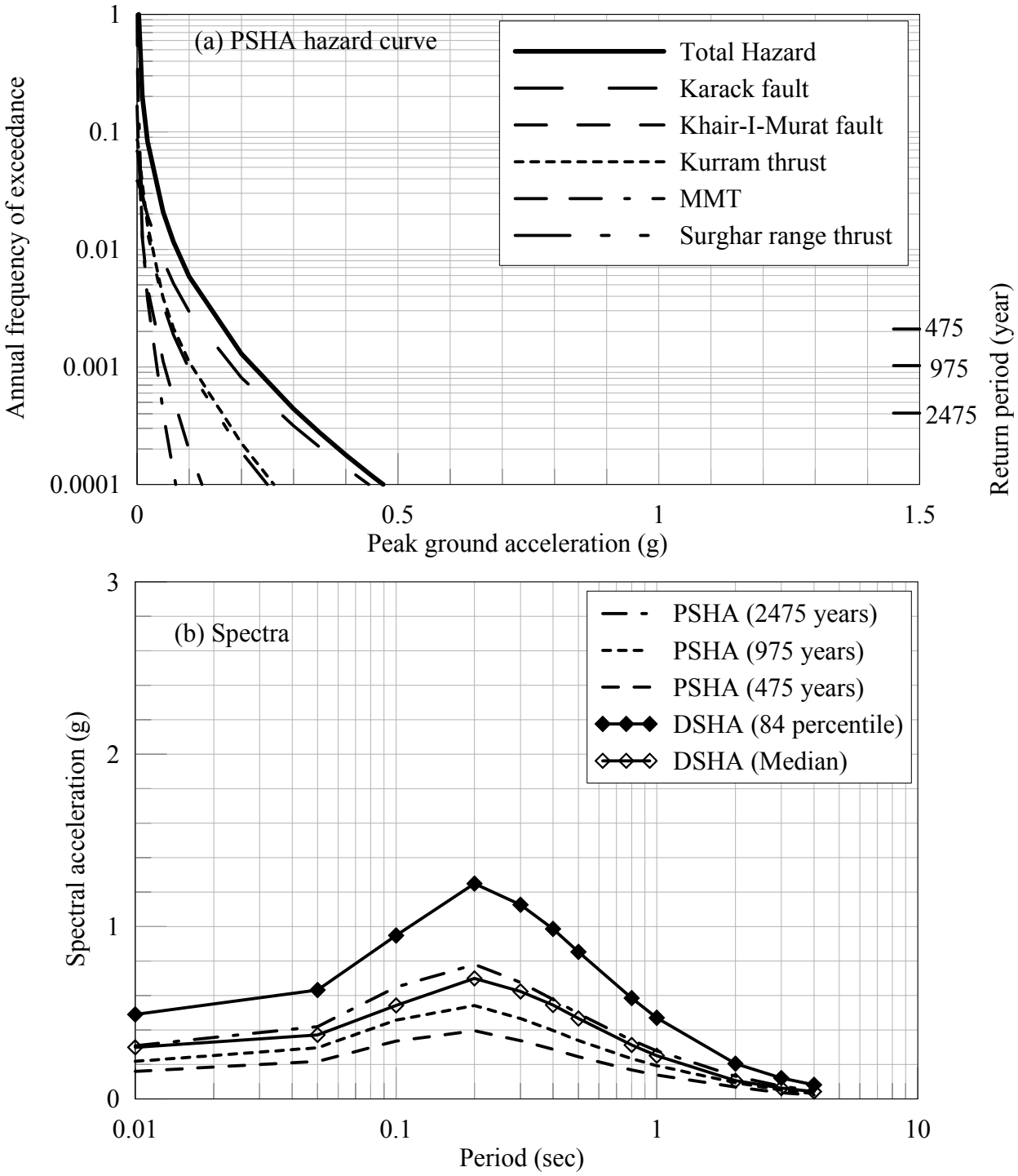

Figure 5-10 Seismic hazard result for Bannu for an assumed bedrock with $V_{s,30}$ of 760 m/sec. (a) PSHA hazard curves for PGA at 5% damping. The hazards by the top five contributing faults are shown; (b) PSHA uniform hazard spectra (UHS) and DSHA hazard spectra.

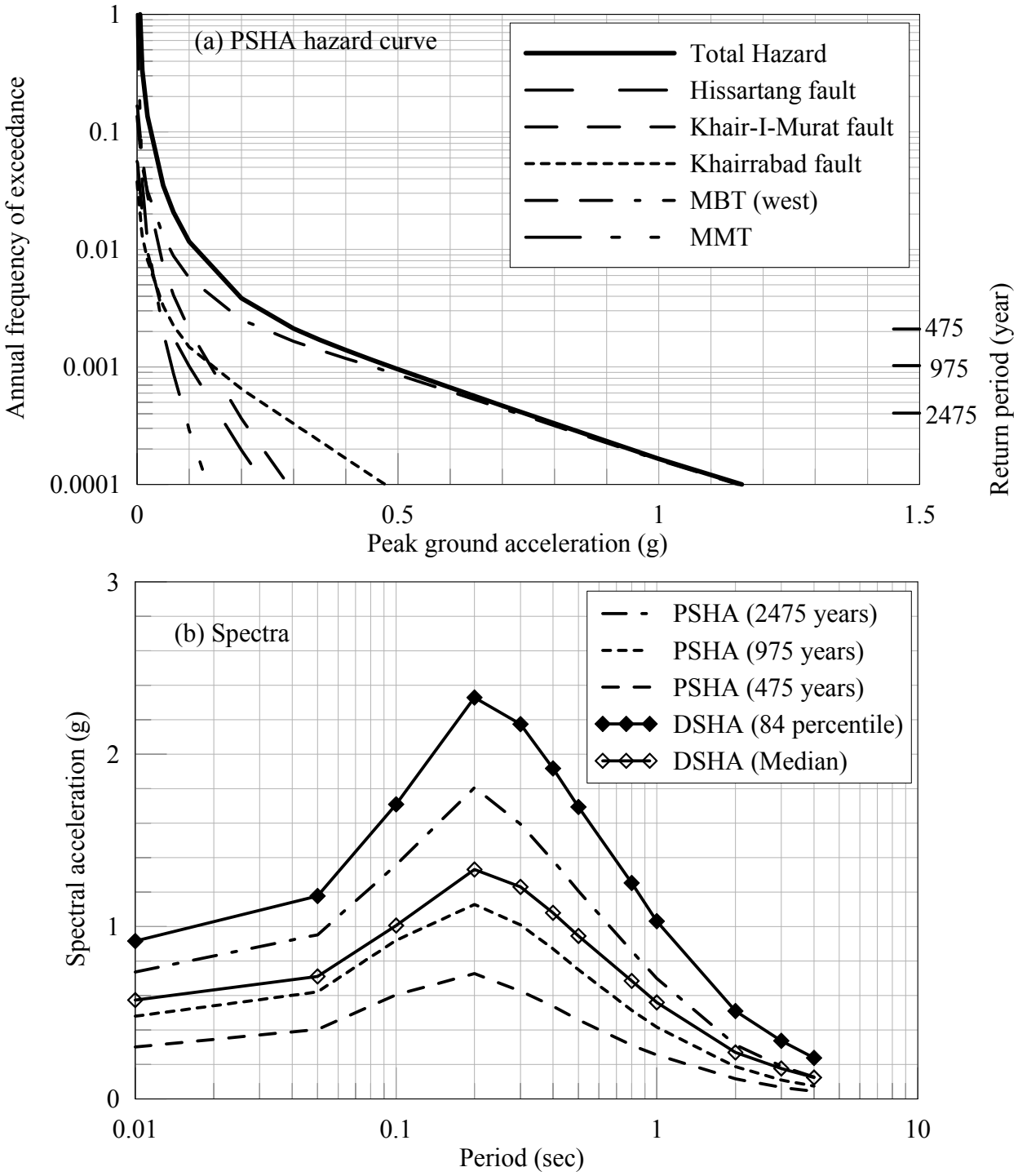

Figure 5-11 Seismic hazard result for Kohat for an assumed bedrock with $V_{s,30}$ of 760 m/sec. (a) PSHA hazard curves for PGA at 5% damping. The hazards by the top five contributing faults are shown; (b) PSHA uniform hazard spectra (UHS) and DSHA hazard spectra.

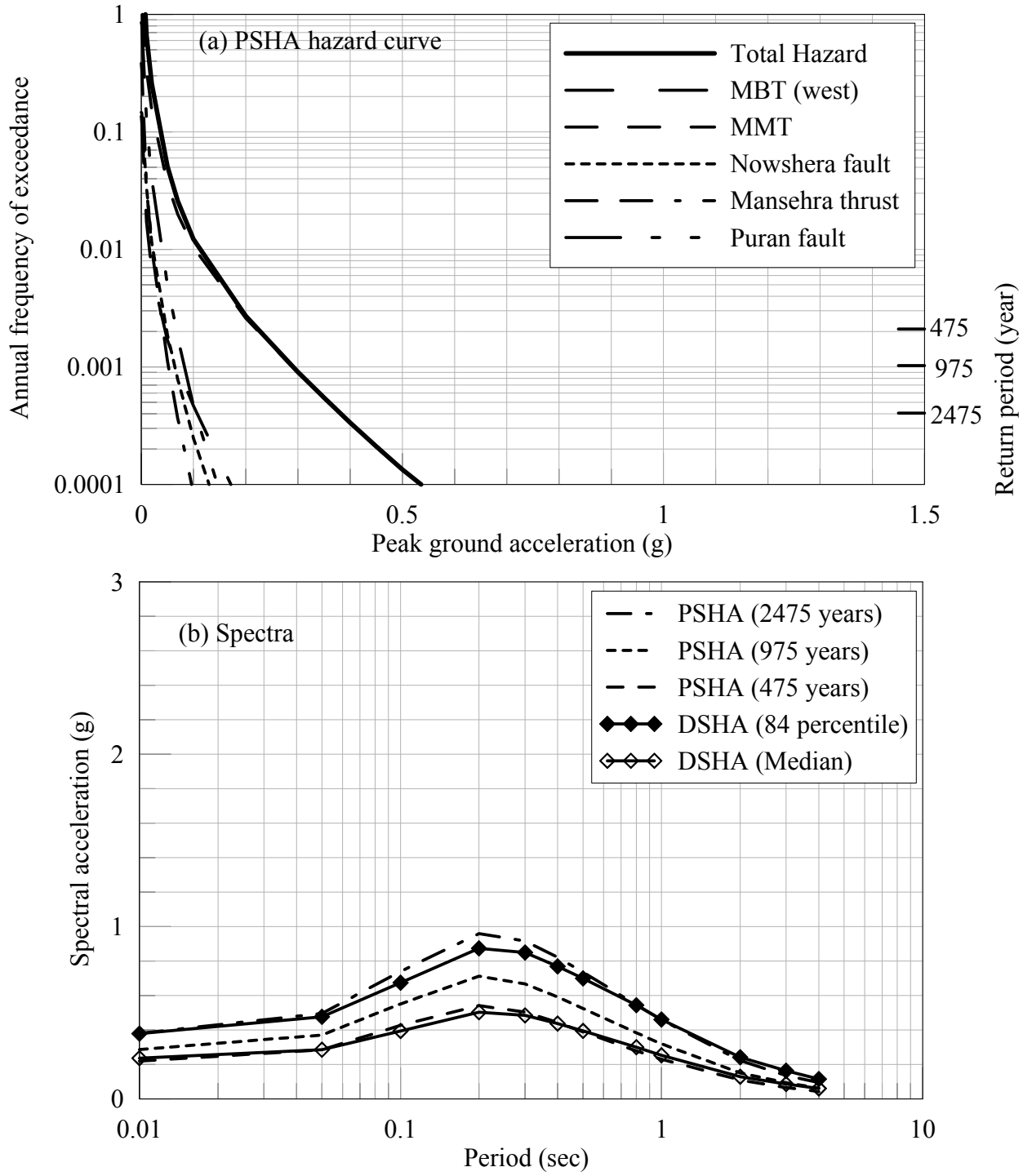

Figure 5-12 Seismic hazard result for Malakand for an assumed bedrock with $V_{s,30}$ of 760 m/sec. (a) PSHA hazard curves for PGA at 5% damping. The hazards by the top five contributing faults are shown; (b) PSHA uniform hazard spectra (UHS) and DSHA hazard spectra.

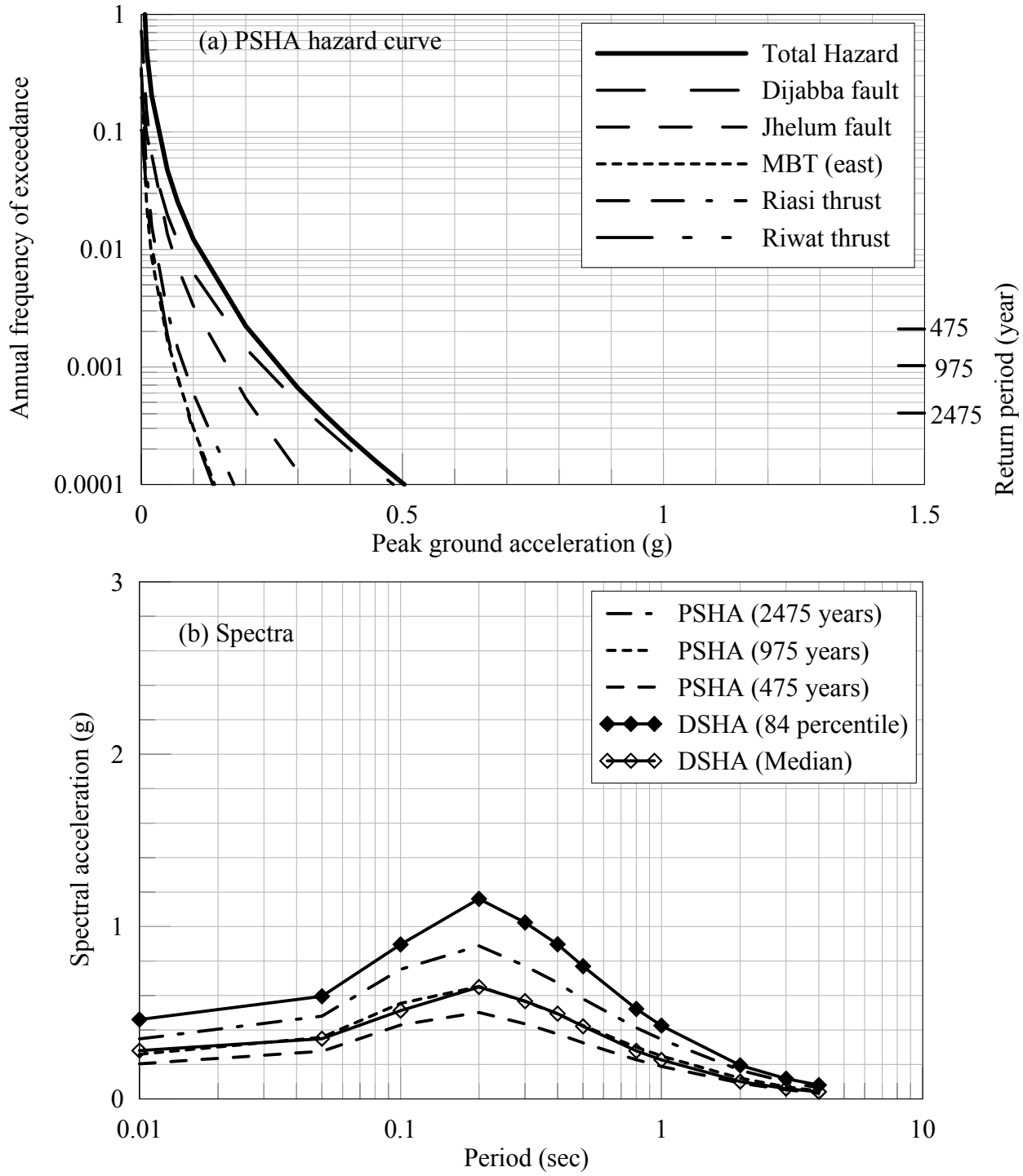

Figure 5-13 Seismic hazard result for Mangla for an assumed bedrock with $V_{s,30}$ of 760 m/sec. (a) PSHA hazard curves for PGA at 5% damping. The hazards by the top five contributing faults are shown; (b) PSHA uniform hazard spectra (UHS) and DSHA hazard spectra.

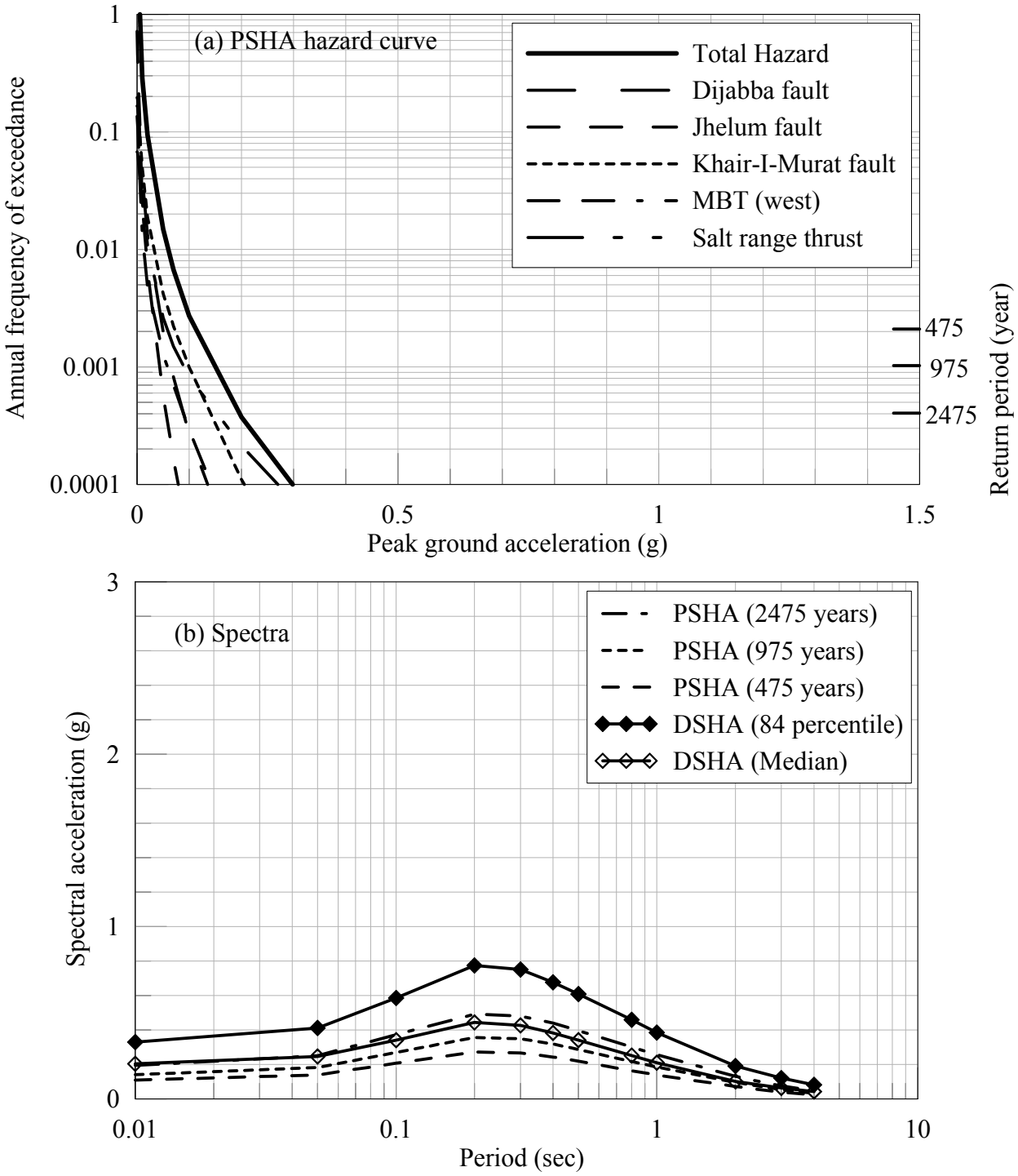

Figure 5-14 Seismic hazard result for Talagang for an assumed bedrock with $V_{s,30}$ of 760 m/sec. (a) PSHA hazard curves for PGA at 5% damping. The hazards by the top five contributing faults are shown; (b) PSHA uniform hazard spectra (UHS) and DSHA hazard spectra.

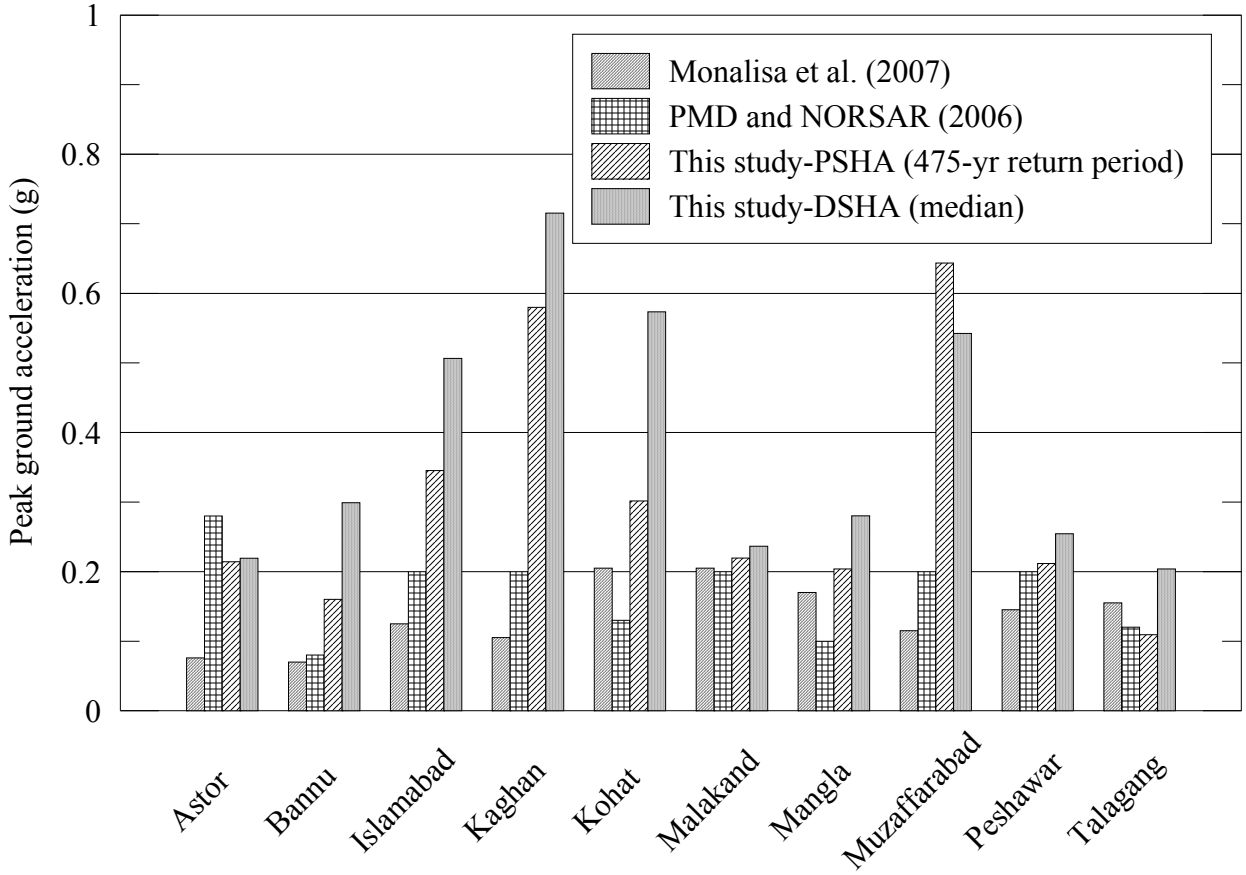

Figure 5-15 PGAs computed by PSHA and DSHA for an assumed bedrock with $V_{s,30}$ of 760 m/sec, compared to those computed by others (PMD and NORSAR 2006; Monalisa et al. 2007). PGAs estimated by Monalisa et al. (2007) correspond to a 475-year return period, while PMD and NORSAR (2006) values correspond to a 500-year return period.

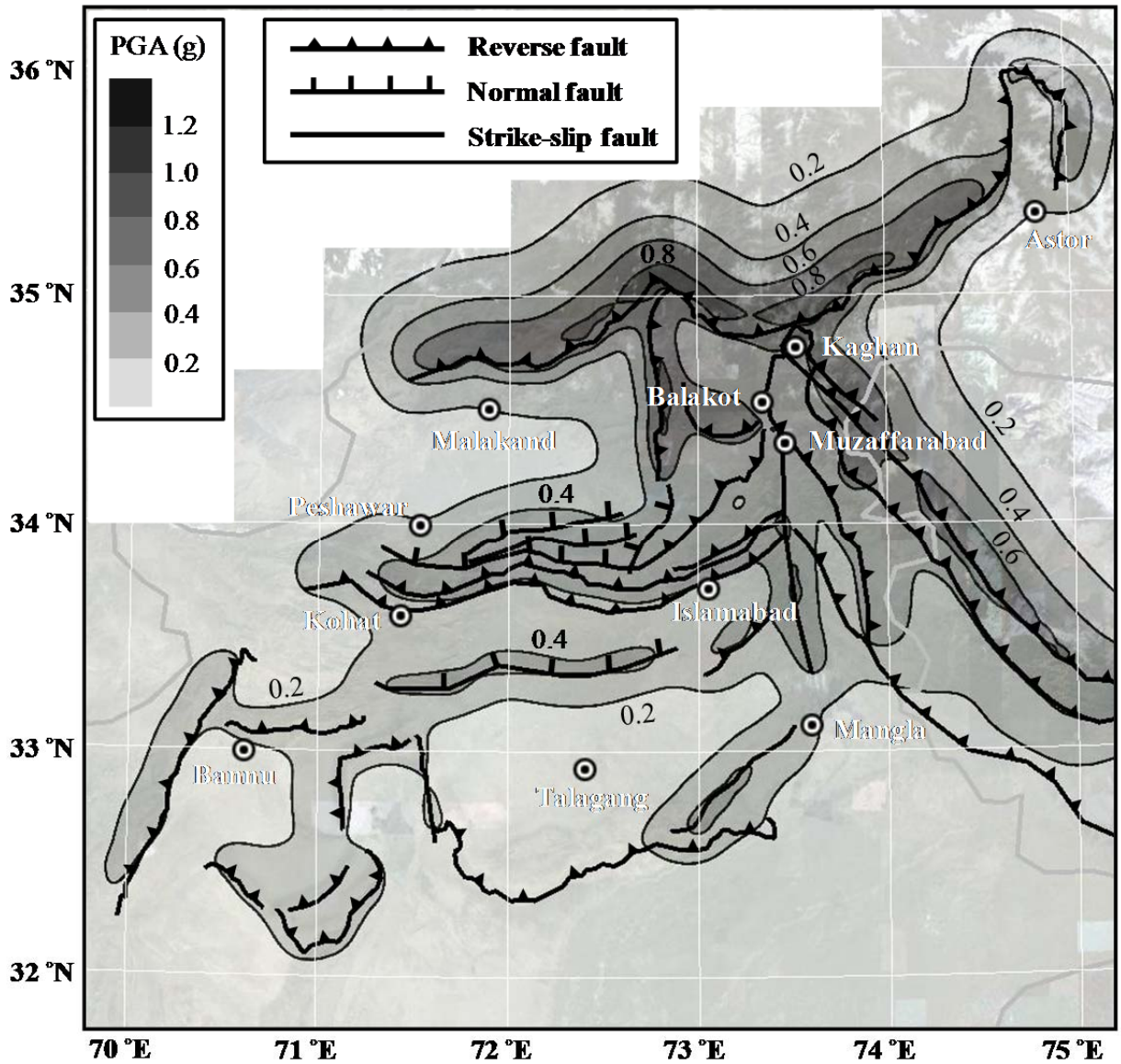

Figure 5-16 Seismic hazard map of NW Pakistan for PGA at a 475-year return period. A 0.1° × 0.1° grid was analyzed using PSHA for an assumed bedrock with $V_{s,30}$ of 760 m/sec. The contour interval is 0.2g.

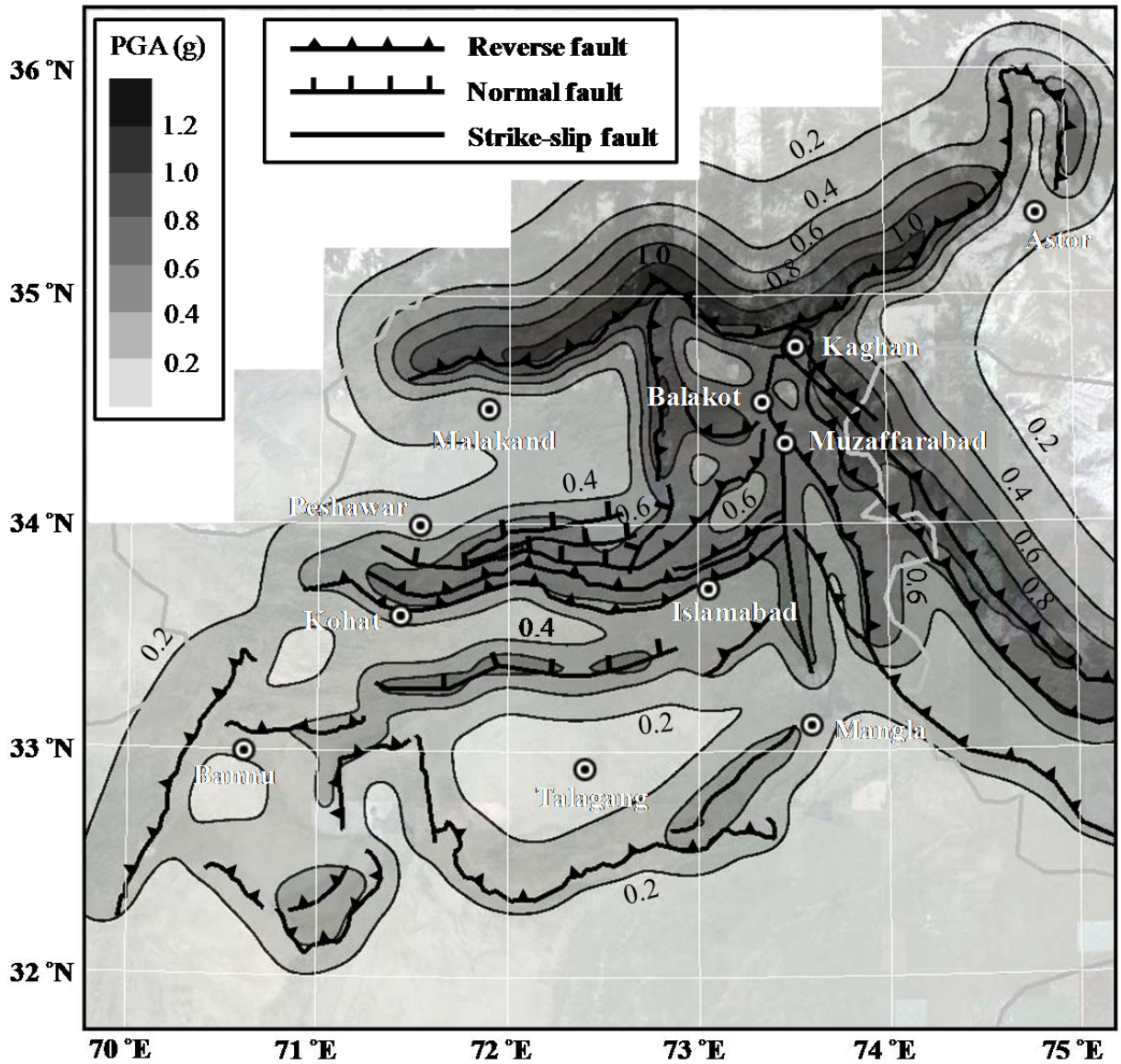

Figure 5-17 Seismic hazard map of NW Pakistan for PGA at a 975-year return period. A 0.1° × 0.1° grid was analyzed using PSHA for an assumed bedrock with $V_{s,30}$ of 760 m/sec. The contour interval is 0.2g.

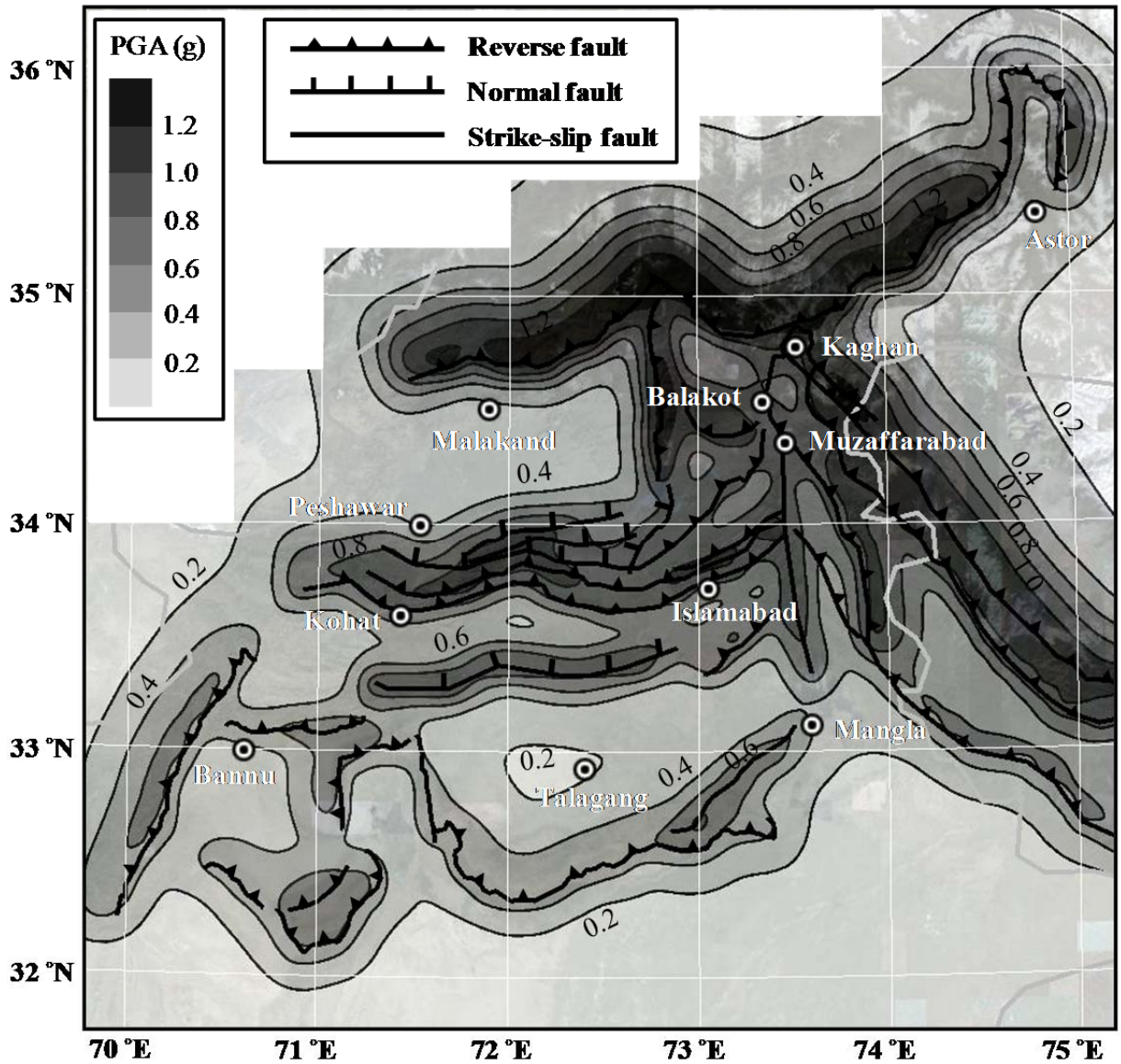

Figure 5-18 Seismic hazard map of NW Pakistan for PGA at a 2475-year return period. A 0.1° × 0.1° grid was analyzed using PSHA for an assumed bedrock with $V_{s,30}$ of 760 m/sec. The contour interval is 0.2g.

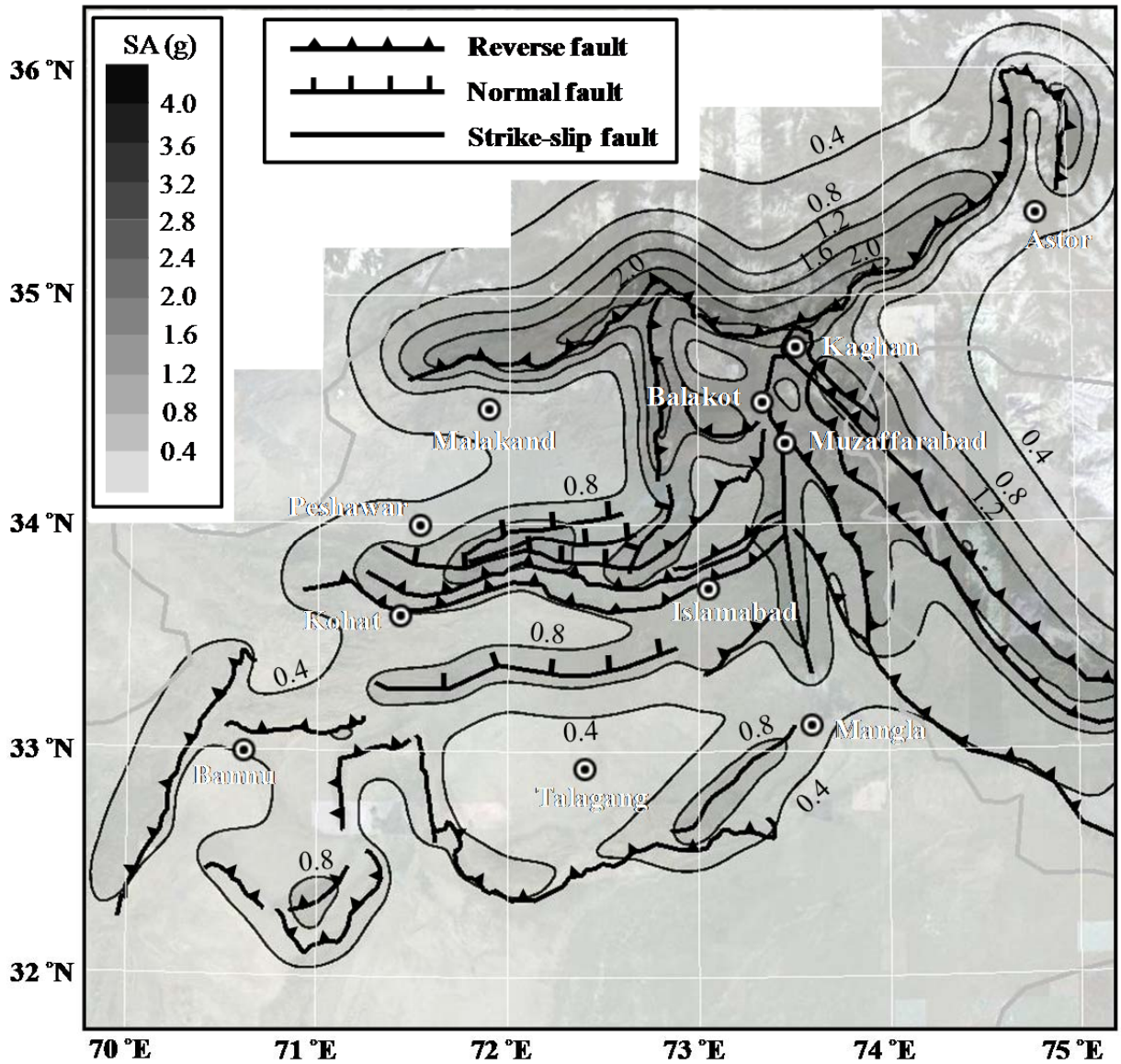

Figure 5-19 Seismic hazard map of NW Pakistan for SA (T=0.2 sec) at a 475-year return period. A 0.1° × 0.1° grid was analyzed using PSHA for an assumed bedrock with $V_{s,30}$ of 760 m/sec. The contour interval is 0.4g.

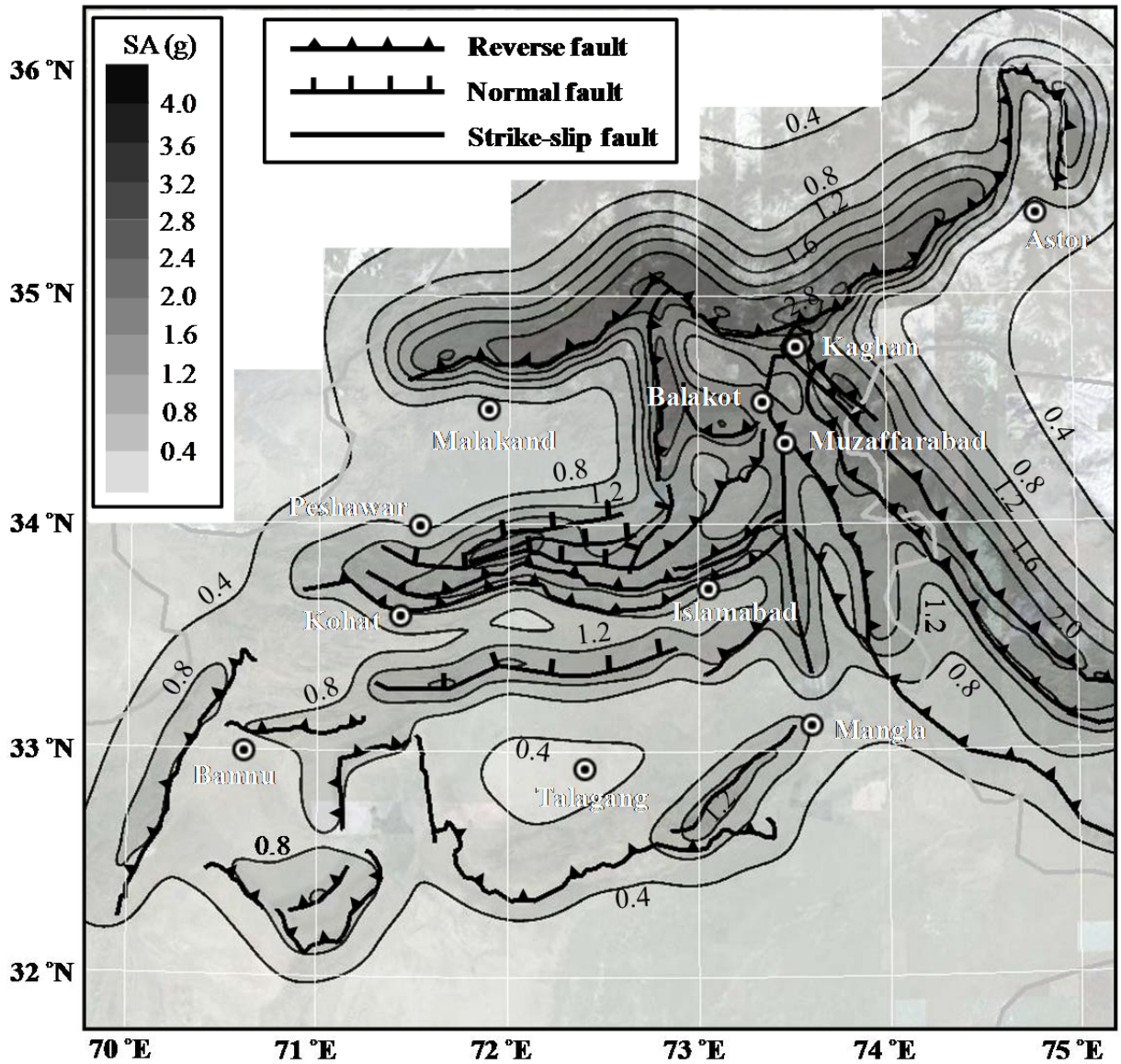

Figure 5-20 Seismic hazard map of NW Pakistan for SA (T=0.2 sec) at a 975-year return period. A 0.1° × 0.1° grid was analyzed using PSHA for an assumed bedrock with $V_{s,30}$ of 760 m/sec. The contour interval is 0.4g.

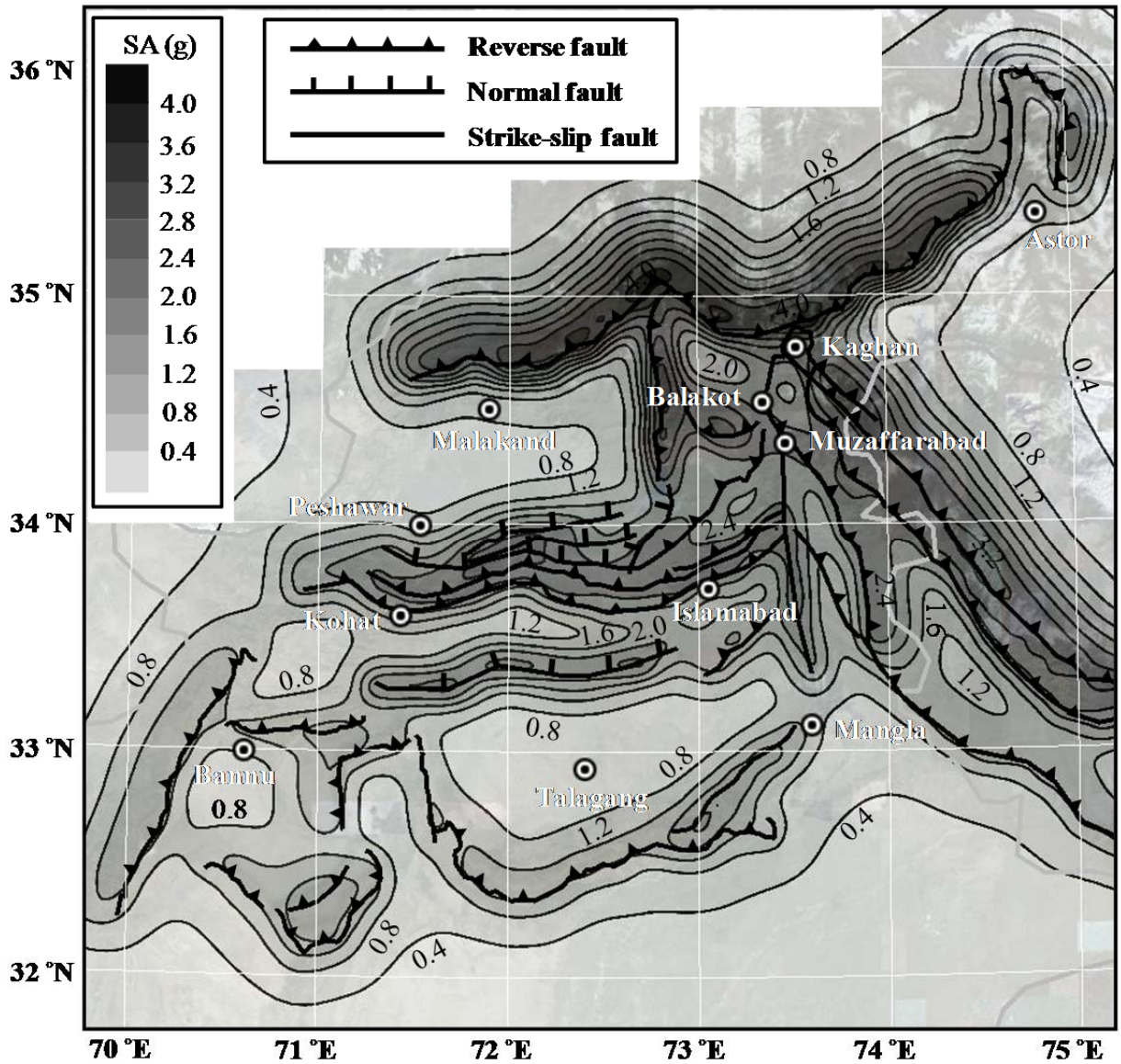

Figure 5-21 Seismic hazard map of NW Pakistan for SA (T=0.2 sec) at a 2475-year return period. A 0.1° × 0.1° grid was analyzed using PSHA for an assumed bedrock with $V_{s,30}$ of 760 m/sec. The contour interval is 0.4g.

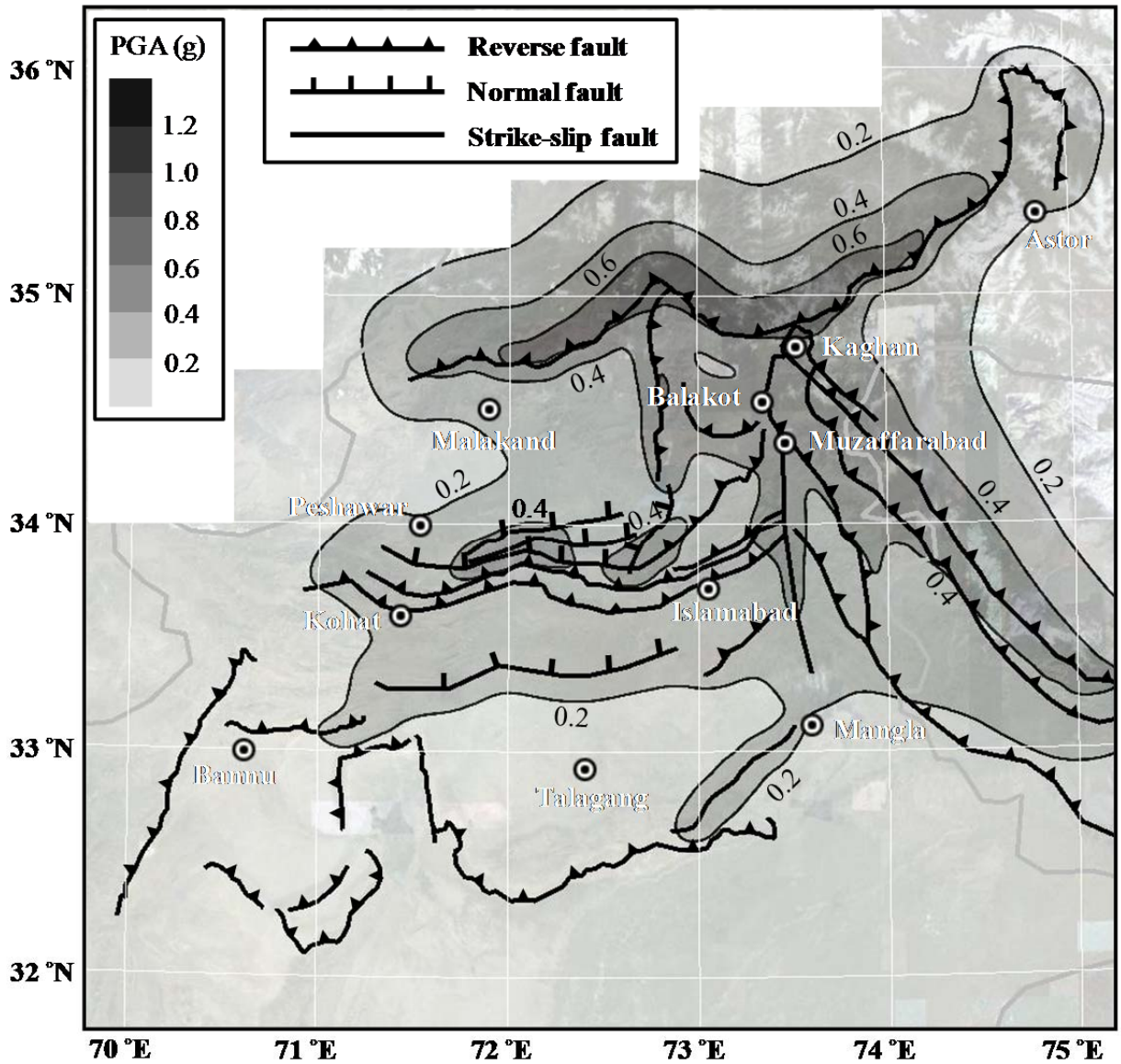

Figure 5-22 Seismic hazard map of NW Pakistan for SA (T=1.0 sec) at a 475-year return period. A 0.1° × 0.1° grid was analyzed using PSHA for an assumed bedrock with $V_{s,30}$ of 760 m/sec. The contour interval is 0.2g.

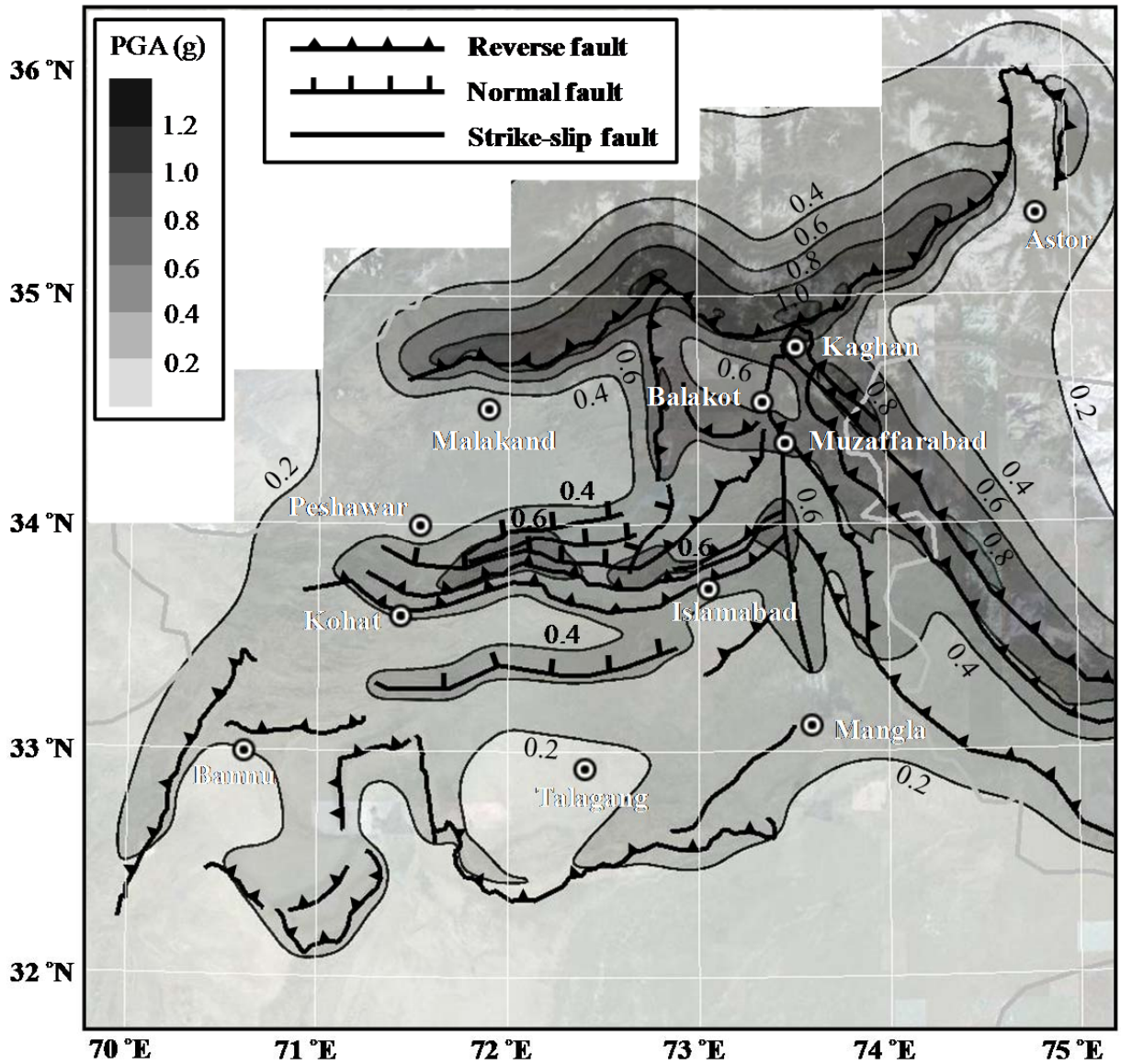

Figure 5-23 Seismic hazard map of NW Pakistan for SA (T=1.0 sec) at a 975-year return period. A 0.1° × 0.1° grid was analyzed using PSHA for an assumed bedrock with $V_{s,30}$ of 760 m/sec. The contour interval is 0.2g.

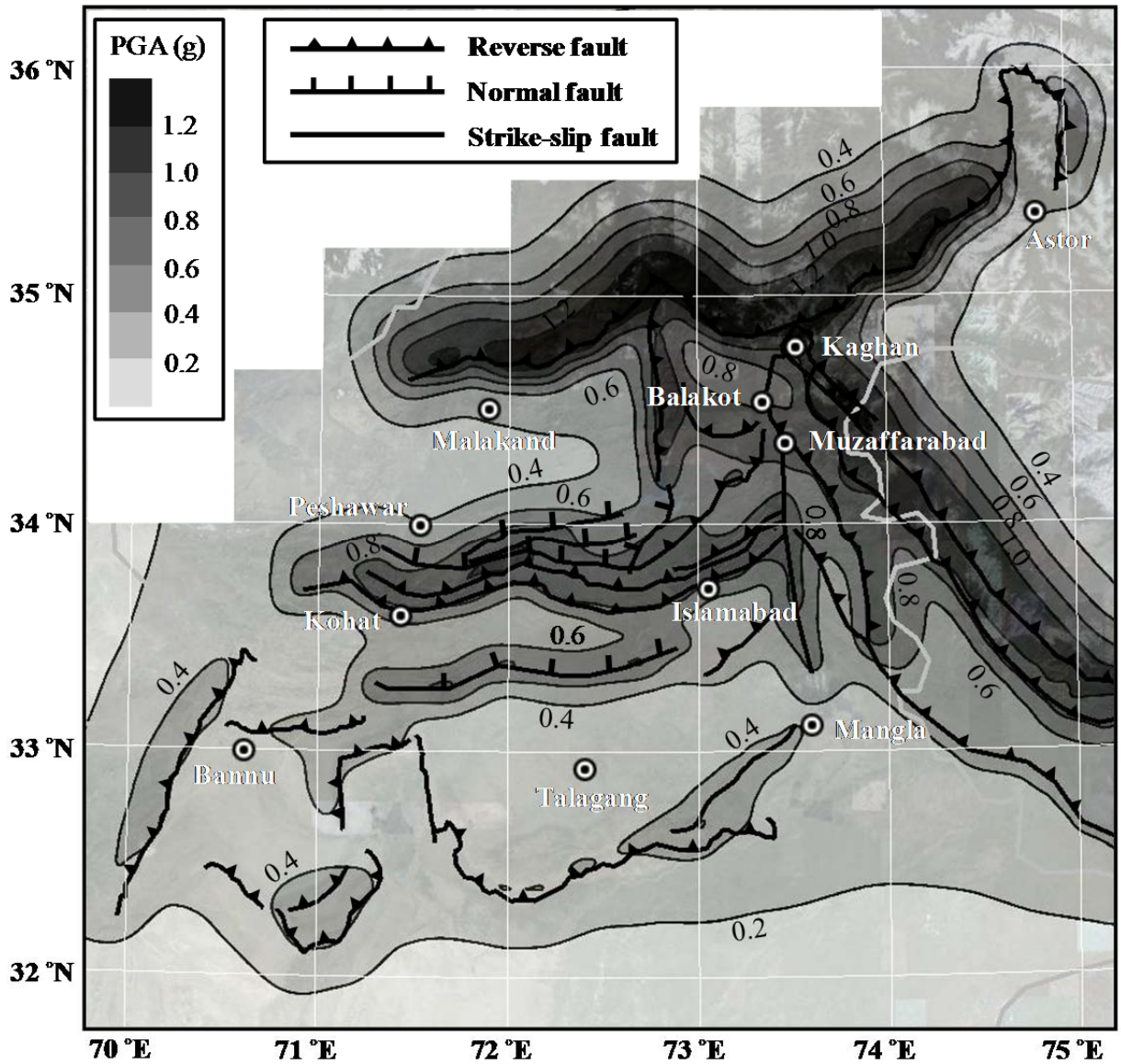

Figure 5-24 Seismic hazard map of NW Pakistan for SA (T=1.0 sec) at a 2475-year return period. A 0.1° × 0.1° grid was analyzed using PSHA for an assumed bedrock with $V_{s,30}$ of 760 m/sec. The contour interval is 0.2g.

CHAPTER 6. CONDITIONAL MEAN SPECTRA (CMS)

6.1 The CMS framework

The uniform hazard spectrum from a PSHA is often used to develop spectrum-compatible ground motions for engineering analysis. This UHS is constructed by enveloping the spectral amplitudes at all periods. The amplitude has a corresponding "standard" normal random variable, or ε parameter, computed as:

$$\varepsilon(T) = \frac{\ln Sa(T) - \mu_{\ln Sa}(M, R, T)}{\sigma_{\ln Sa}(T)} \qquad \text{Eq. (9)}$$

where $\ln Sa(T)$ is the natural logarithm of the spectral acceleration at the period of interest; and $\mu_{\ln Sa}(M, R, T)$ and $\sigma_{\ln Sa}(T)$ are the predicted mean and standard deviation, respectively, of $\ln Sa(T)$ (McGuire 1995).

No single earthquake will produce a response spectrum as high as the UHS throughout the frequency range considered (Baker and Cornell 2006) For example, the high- and low-frequency portions of a UHS often correspond to different events (i.e., the high-frequency portion of the UHS is often dominated by small nearby earthquakes, while the low-frequency portion of the UHS is often dominated by larger, more distant earthquakes), Therefore, using a UHS as a target or design spectrum can be conservative if the structures at a site have a narrow range of natural frequencies. A conditional mean spectrum (CMS) can take into account the variation of SA amplitudes and ε for periods of interest, while maintaining the rigor of PSHA. The CMS yields a spectrum that is smaller than the UHS, allowing a more efficient seismic design. The procedure for computing CMS is summarized as follows (Baker 2008).

1) Determine the target SA and the associated M_w, R, and ε at the period of interest (T*).
2) Compute the median and standard deviation of the response spectrum, given M_w and R.
3) Compute ε at other periods, given ε(T*).
4) Compute the CMS.

6.2 Application of CMS to two Cities in NW Pakistan

Step 1: Determine the target SA and the associated M_w, R, and ε at T*. The UHS for Islamabad and Muzaffarabad were developed using PSHA (Figure 5-1b and Figure 5-3b). For this example, we selected periods of interest, T* = 0.05 sec, 0.2 sec, and 1.0 sec. Since the target SA(T*) was obtained from PSHA, the associated M_w, R, and ε values can be taken as the mean values from deaggregation. These values are provided in Table 5-1 for return periods of 475, 975, and 2475 years.

Step 2: Compute the median and standard deviation of the response spectrum, given M_w and R. The Next Generation Attenuation (NGA) models of ground motions used for the seismic hazard analysis were employed in this step. The relation used here are Abrahamson-Silva (2008), Boore-Atkinson (2008), Campbell-Bozorgnia (2008), and Idriss (2008). The CMS were developed separately using each attenuation relation and later combined using equal weights.

Step 3: Compute ε at other periods, given ε(T*). Baker (2008) indicated that conditional mean ε at other periods can be computed as:

$$\mu_{\varepsilon(T_i)/\varepsilon(T^*)} = \rho(T_i, T^*)\varepsilon(T^*) \qquad \text{Eq. (10)}$$

where $\mu_{\varepsilon(T_i)/\varepsilon(T^*)}$ is the mean value of $\varepsilon(T_i)$, given $\varepsilon(T^*)$; and $\rho(T_i, T^*)$ is the correlation coefficient between the ε values at the two periods. Baker (2008) proposed the following relation to define the correlation coefficient:

$$\rho(T_{\min}, T_{\max}) = 1 - \cos\left(\frac{\pi}{2} - \left(0.359 + 0.163 I_{(T_{\min}<0.189)} \ln\frac{T_{\min}}{0.189}\right)\ln\frac{T_{\max}}{T_{\min}}\right) \qquad \text{Eq. (11)}$$

where $T_{\min}$ and $T_{\max}$ are the smaller and larger of the two periods of interest, respectively, and $I_{(T_{\min}<0.189)}$ is a binary function equal to 1 if $T_{\min} < 0.189\text{sec}$ and equal to 0 otherwise.

Equation (3) is valid only for the 0.05 < T (sec) < 5. Baker and Jayaram (2008) proposed a refined correlation model that is valid over a wider period range of 0.01 to 10 seconds as:

$$\begin{aligned} &\text{if } T_{\max} < 0.109 \text{ sec}, \quad \rho_{\varepsilon(T_1),\varepsilon(T_2)} = C_2 \\ &\text{else if } T_{\min} > 0.109 \text{ sec}, \quad \rho_{\varepsilon(T_1),\varepsilon(T_2)} = C_1 \\ &\text{else} \quad \rho_{\varepsilon(T_1),\varepsilon(T_2)} = C_4 \end{aligned} \qquad \text{Eq. (12)}$$

$$C_1 = 1 - \cos\left(\frac{\pi}{2} - 0.366 \ln\left(\frac{T_{\max}}{\max(T_{\min}, 0.109)}\right)\right) \qquad \text{Eq. (13)}$$

$$C_2 = \begin{cases} 1 - 0.105\left(1 - \dfrac{1}{1+e^{100T_{\max}^{-5}}}\right)\left(\dfrac{T_{\max} - T_{\min}}{T_{\max} - 0.0099}\right) & \textit{if} \quad T_{\max} < 0.2\,\text{sec} \\ 0 & \textit{otherwise} \end{cases} \qquad \text{Eq. (14)}$$

$$C_3 = \begin{cases} C_2 & \text{if} \quad T_{\max} < 0.109\,\text{sec} \\ C_1 & \text{otherwise} \end{cases} \qquad \text{Eq. (15)}$$

$$C_4 = C_1 + 0.5\left(\sqrt{C_3} - C_3\right)\left(1 + \cos\left(\frac{\pi T_{\max}}{0.109}\right)\right) \qquad \text{Eq. (16)}$$

where $T_{\min} = \min(T_1, T_2)$, and $T_{\max} = \max(T_1, T_2)$.

Figure 6-1 compares these two correlation coefficients.

Step 4: Compute CMS. Using the relationship of Baker and Jayaram (2008), the CMS at three target periods (T* = 0.05 sec, 0.2 sec, and 1.0 sec) corresponding to the UHS for 2475-, 975-, and 475-year return periods for Islamabad and Muzaffarabad were constructed as shown in Figure 6-2 and Figure 6-3, respectively. For Islamabad, when SA at 0.05 sec with 475-year return period is selected, the computed CMS is similar to the UHS. There is only a small reduction of acceleration (approximately 0.1 g) at longer periods. When SA at 0.2 sec with 475-year return period is targeted, the CMS becomes slightly smaller than the UHS at periods of 0.05 sec and 1.0 sec. However the CMS becomes similar to the UHS for PGA and SA at periods > 3.0 sec. The CMS becomes significantly smaller than the UHS at periods < 1.0 sec when the SA at 1.0 sec is targeted. The SA at 0.2 sec and the PGA are reduced by approximately 0.35g and 0.13 g, respectively. A similar trend can be observed when the UHS for 975-year return period is targeted at periods of 0.05 sec, 0.2 sec, and 1.0 sec, but the difference between the CMS and the UHS becomes larger. When the CMS is generated for SA at 1.0 sec, the SA at 0.2 sec and the PGA are reduced by approximately 0.46g and 0.27g, respectively when the CMS is used. For the UHS with 2475-year return period, the difference between the UHS and the CMS is substantial. Especially when the SA at 1.0 sec is targeted, the SA at 0.2 sec and the PGA are reduced to approximately 0.86g and 0.33g, respectively. The CMS for Muzaffarabad show greater

differences than that for Islamabad (Figure 6-3). When the SA at 1.0 sec for 2475-year return period is targeted, the SA at 0.2 sec and the PGA are reduced by a factor of approximately 2. When the SAs at 0.05 sec and 0.2 sec were targeted, the SA at longer period is significantly reduced.

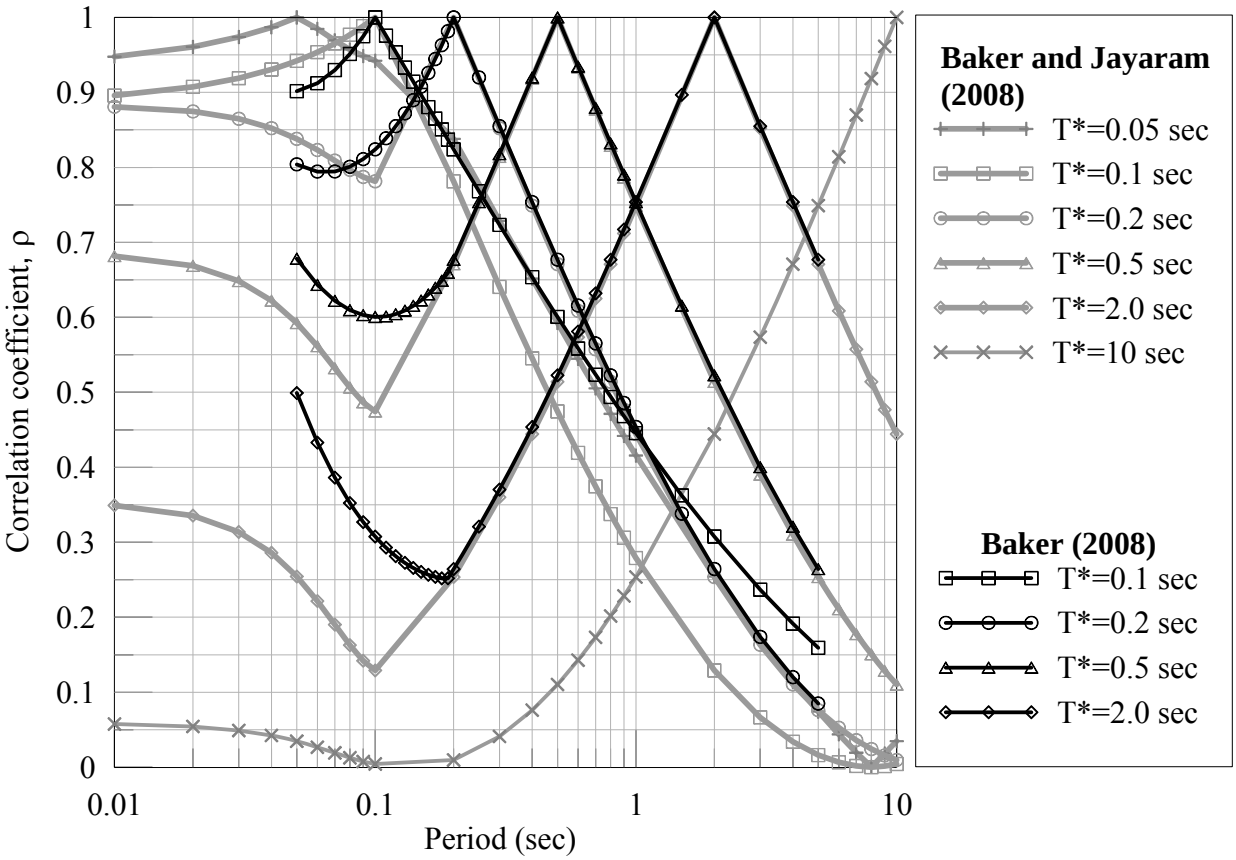

Figure 6-1 Correlation coefficient suggested by Baker (2008) and Baker and Jayaram (2008).

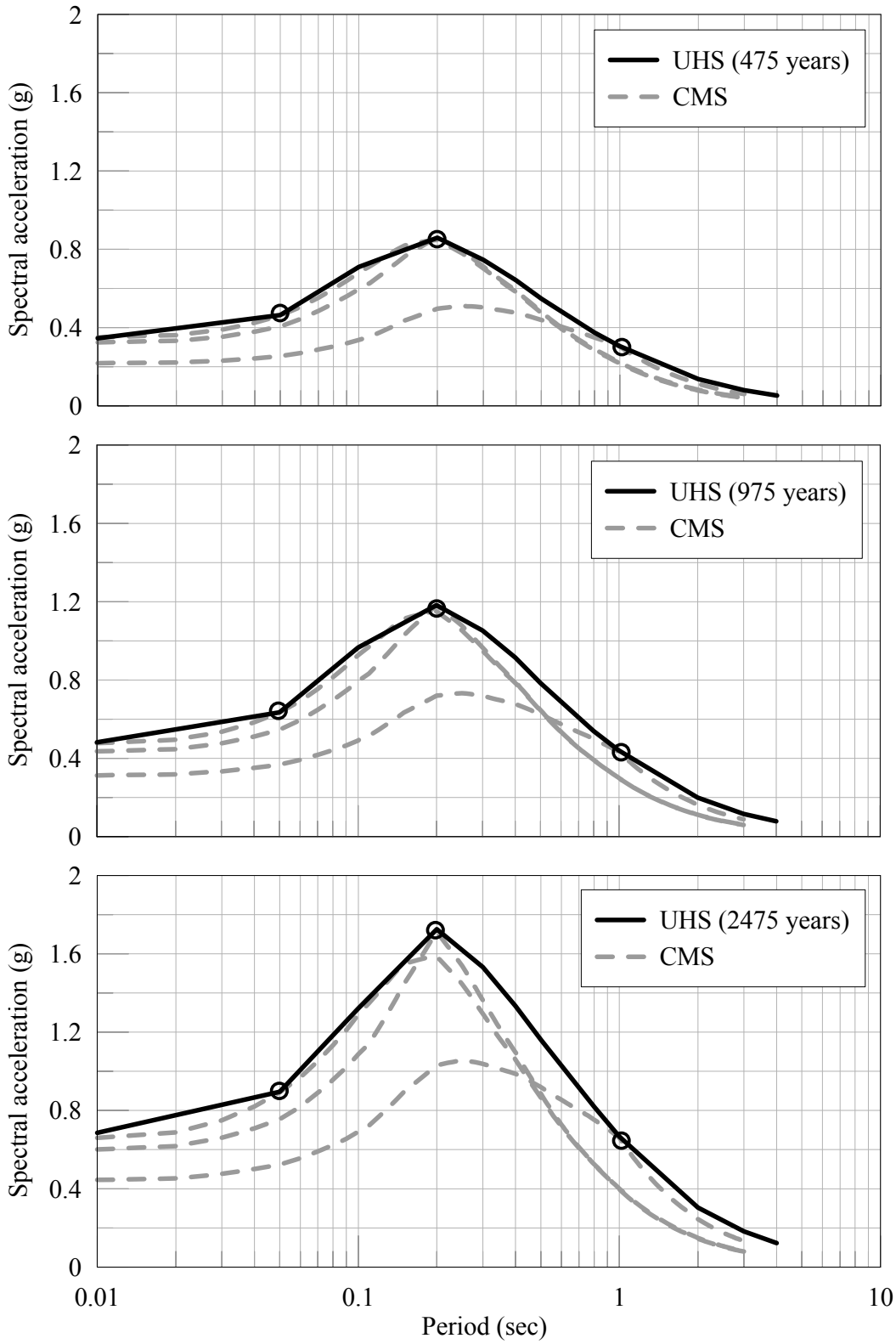

Figure 6-2 CMS at various periods for 475-, 975-, and 2475-year return periods in Islamabad.

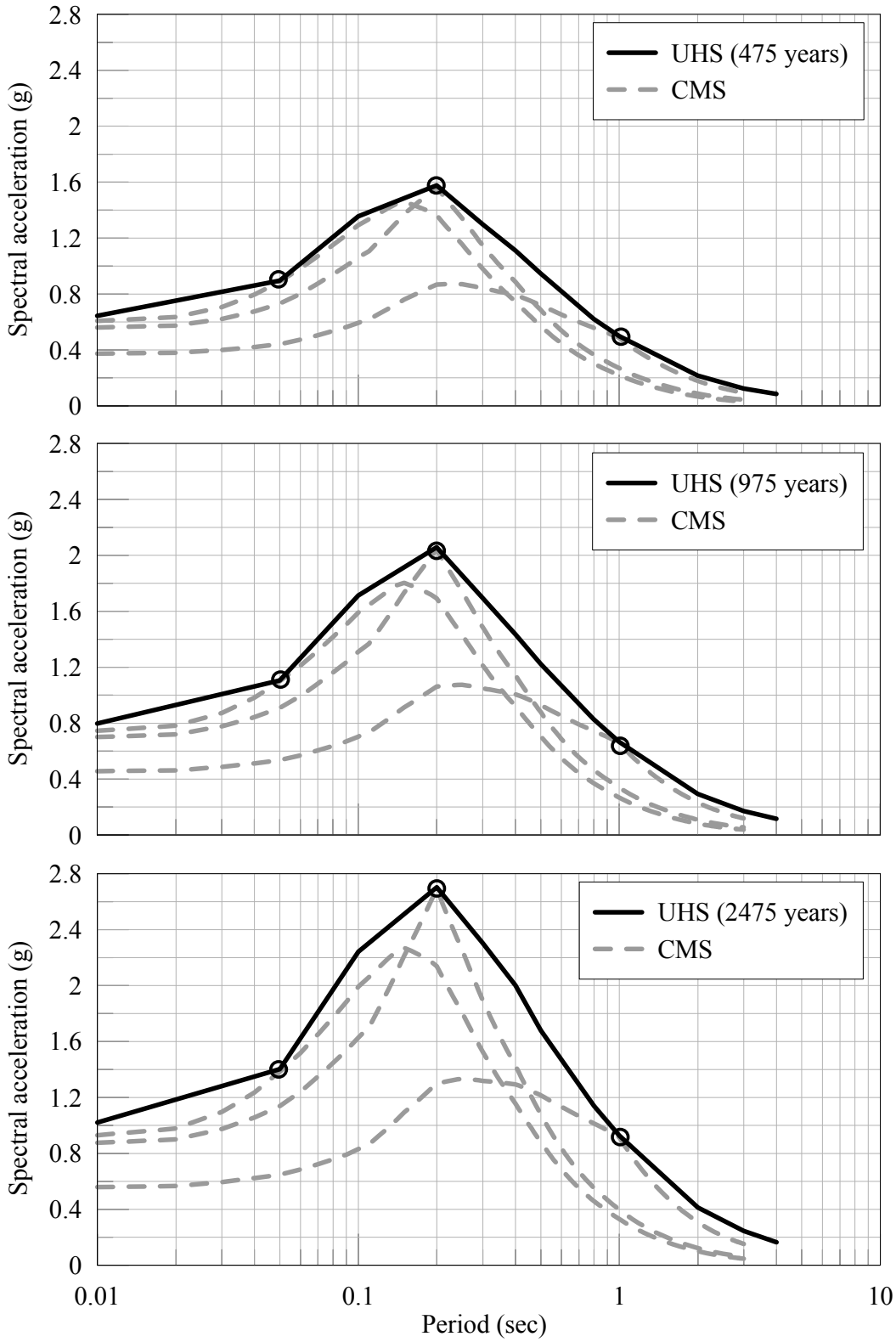

Figure 6-3 CMS at various periods for 475-, 975-, and 2475-year return periods in Muzaffarabad.

CHAPTER 7. SEISMIC SLOPE STABILITY APPROACH

Earthquake-induced landslides can cause numerous fatalities and can create massive disruption following earthquakes as a result of blocking critical transportation routes in mountainous terrain, damming waterways, and triggering seiches. For example, the 2008 Wenchuan earthquake (M_w=7.9) in China triggered more than 15,000 landslides, rockfalls, and debris flow, resulting in approximately 20,000 deaths (Yin et al. 2009). The 2005 Kashmir, Pakistan, earthquake (M_w 7.6) triggered more than 2,400 landslides (Sato et al. 2007), including the 68×10^6 m^3 Hattian Bala rock avalanche which destroyed an entire village and caused about 1,000 fatalities (Dunning et al. 2007). The 1999 Chi-chi, Taiwan, earthquake (M_w 7.6) triggered more than 9,200 landslides throughout a region of approximately 128 km^2 (Liao 2000). The largest of these was the Tsaoling landslide involved 125×10^6 m^3 of rock and caused 39 fatalities (Tang et al. 2009). The 1989 Loma Prieta, California, earthquake (M_w 6.9) triggered thousands of landslides over an area of about 15,000 km^2, damaging more than 200 residences, numerous roads, and other structures, with damage estimates exceeding US$30 million (Keefer and Manson 1998).

Since earthquake-induced landslides cause significant damage, the distribution of landslide has been of interest for many scientists and engineers. One of the pioneering researches were conducted by Keefer (1984). He proposed the relation between earthquake magnitude and area affected by landslides based on historical earthquake data. According to his relation, the area of approximately 100,000 km^2 can be possibly affected by landslides induced by the earthquake of M_w = 8.0. Some researchers have studied the distribution of landslides in terms of landslide concentration along the distance from the fault (Keefer 2000; Khazai and Sitar 2004; Sato et al. 2007; Dai et al. 2011). The results from these researches show the common trend; the

landslides are highly concentrated near the fault, which cannot be well captured by the existing slope stability analysis methods.

Although more sophisticated analyses (i.e., 2D and 3D limit equilibrium, 2D and 3D finite element, and 3D discrete element analyses) are available for accurate slope stability analysis for individual slopes, these are not practical to assess regional performance of slopes. Therefore the present study will conduct the simplified seismic slope stability analysis using the best estimated rock properties and slope geometries in the affected areas. This report will propose possible factors that are not commonly incorporated in the current practice, but can affect the landslide distribution and explain the high concentration of landslides near fault.

7.1 General approaches to analyze seismic slope stability

Several simplified methods are available to estimate the factor of safety (FS) against sliding and displacements during earthquake-induced landslides. These methods include pseudo-static analysis, the Newmark (1965) sliding block method, modified Newmark method, simplified displacement charts, and energy-based methods. Terzaghi (1950) first applied a pseudo-static approach to analyze seismic slope stability. This approach is based on conventional limit equilibrium slope stability analysis with horizontal and vertical pseudo-static forces that act on the critical failure mass. This approach results in prediction of factor of safety against sliding, and can be also used to determine a yield acceleration (a_y) for use in a Newmark sliding block analysis.

The pseudo-static method of analysis does not provide information on deformations associated with seismically-induced slope failures. The Newmark (1965) sliding block analysis was first proposed to estimate permanent displacements of a sliding mass. In this method, the sliding mass is represented as a rigid block on a uniform slope and displacements are integrated

from base acceleration pulses that exceed the block's yield acceleration. If the acceleration does not exceed the yield acceleration, there is no computed sliding block displacement.

Makdisi and Seed (1978) proposed a simple method for the seismic design of small embankments that uses the concept originally proposed by Newmark (1965). They used a finite element analysis to compute the variation of permanent displacement with a_y/PGA (where PGA is the peak ground acceleration) and earthquake moment magnitude (M_w) based on several real and hypothetical dams with heights in the range of 30-60 m and constructed of compacted cohesive soils and very dense cohesionless soils, and several recorded and synthetic ground motions scaled to represent different earthquake magnitudes. The displacement was normalized by the peak base acceleration and fundamental period of the embankment. Yegian et al. (1991) and Bray et al. (1998) proposed variations of this method to estimate seismic slope displacement.

Many researchers later modified the Newmark method to deal with compliant slope materials (e.g., Lin and Whitman 1983; Kramer and Smith 1997; Rathje and Bray 2000). When seismic waves propagate through a slope, different parts of the slope will move by different amount and with different phases (Kramer and Smith 1997). This phenomenon is most significant for thick, soft materials and short wavelengths. To accommodate these factors, Kramer and Smith (1997) replaced the single rigid block of the conventional Newmark method by two or more blocks connected by springs and dashpots.

The Newmark method and its modifications, using force equilibrium, can evaluate a displacement of a rigid soil block along a fixed slip surface. However, in actual slopes failures, sliding mass may not always behave as a rigid body, especially for deep landslides. Sometimes the landslides become destructive because the soil strength decreases significantly after the initiation of failure. In order to evaluate slope failure including flow failures from their initiation

to termination, Kokusho and Kabasawa (2003) proposed an energy approach, and Kokusho and Ishizawa (2007) further developed it. In their method, the driving energy for slope failure is considered to be the earthquake energy and the gravitational potential energy. They performed shaking table tests to quantify the earthquake energy required to initiate slope failure. Then four energies (potential energy changed by gravity, earthquake energy contributing to slope failure, dissipated energy in a sliding soil mass, and kinematic energy) were correlated to evaluate the slope displacement.

Displacement occurred during earthquake-induced landslides is not the interest of this study, but we rather focus on whether the slope failed or not due to earthquake by checking the factor of safety. Therefore, this study will use the pseudo-static slope stability analysis to evaluate the regional performance of slopes during earthquake.

7.2 Pseudo-static slope stability analysis

Terzaghi (1950) first applied a pseudo-static approach to analyze seismic slope stability. This approach uses a single, monotonically-applied horizontal and/or vertical acceleration to represent earthquake loading. (Although the vertical acceleration can be included in a pseudo-static analysis, it is rarely used in practice, as explained below.) The horizontal and vertical pseudo-static forces, F_h and F_v, respectively, act through the sliding mass centroid and are defined as:

$$F_h = \frac{a_h W}{g} = k_h W \quad and \quad F_v = \frac{a_v W}{g} = k_v W \qquad \text{Eq. 17}$$

where a_h and a_v = horizontal and vertical accelerations, respectively; k_h and k_v = dimensionless horizontal and vertical pseudo-static coefficients, respectively; and W = weight of the failure mass. Using an infinite slope analysis with this approach has the benefits of being simple and able to reasonably model real shallow slope failures. This condition reasonably approximates many earthquake-induced shallow, disrupted landslides. For an infinite slope where horizontal and vertical pseudo-static seismic loadings act through the sliding mass centroid, the factor of safety can be calculated as:

$$F.S = \frac{\left[(1-k_v)\cos i - k_h \sin i\right]\tan\phi' + \dfrac{c'}{\gamma' D}}{(1-k_v)\sin i + k_h \cos i} \qquad \text{Eq. 18}$$

where c' and ϕ' = Mohr-Coulomb strength parameters that describe the shear strength on the failure plane; γ' = unit weight of failure mass; i = slope and failure plane angle; and D = failure mass thickness.

The horizontal pseudo-static force has a larger influence on the FS than the vertical pseudo-static force, as F_h reduces the resisting force and increases the driving force. Thus, selecting appropriate values for k_h is important for estimating meaningful values of FS. Many investigators have suggested values for these pseudo-static coefficients. For example, Terzaghi (1950) proposed the use of k_h = 0.1 for "severe" earthquakes (Rossi-Forel intensity IX); k_h = 0.2 for "violent, destructive" earthquakes (Rossi-Forel X); and k_h = 0.5 for "catastrophic" earthquakes. Seed (1979) suggested k_h = 0.10 (M = 6.5) to 0.15 (M = 8.25) for earth dams constructed of ductile soils with crest accelerations less than 0.75g. Later, Pyke (1991) proposed a relation between pseudo-static coefficient and M_w, where k_h approaches 0.5 for $M_w > 8.0$.

Other researchers have proposed pseudo-static coefficients that vary with anticipated maximum horizontal acceleration, $a_{h,max}$. For example, Marcuson and Curro (1981) suggested k_h = (1/3 to 1/2)×($a_{h,max}$ /g). Hynes-Griffin and Franklin (1984) suggested k_h = 0.5×($a_{h,max}$ /g). Nozu et al. (1997) proposed a slightly different form [k_h=1/3 ($a_{h,max}$ /g)$^{1/3}$], which gives higher pseudo-static coefficient than the former two approaches for $a_{h,max} \leq 0.5$g, and falls between the two approaches for $a_{h,max} > 0.5$g. Anderson et al. (2008) pointed out that the pseudo-static coefficient is typically assumed to be less than 50 percent of $a_{h,max}$, but are a function of the slope height and frequency content of the ground motion. In this study, we employed two horizontal pseudo-static coefficients, k_h=1/2 ($a_{h,max}$ /g) and k_h=1/3 ($a_{h,max}$ /g) and assigned these values equal weights in the analysis.

Many researchers have discounted the vertical acceleration in computing FS because, as noted by Kramer (1996), the vertical pseudo-static force reduces both the driving and resisting forces. The effect of discounting the vertical pseudo-static force is examined subsequently.

7.3 2005 Kashmir, Pakistan, earthquake using existing pseudo-static slope stability analysis

The 2005 Kashmir earthquake (M_w=7.6) occurred in the northern Pakistan where thrust movements dominant due to the Indian plate colliding with the Eurasian plate. The Balakot-Garhi fault which ruptured during the earthquake is a 50-km-long thrust fault with a dip of 30°NE and rupture depth of 26 km. Sato et al. (2007) reported that 2,424 landslides occurred in their 55 km x 51 km study area. As shown in Figure 7-1, the landslides are highly concentrated along the fault. Sato et al. (2007) performed a statistical analysis of the distribution of landslides triggered by the earthquake. Based on these data, we expressed the landslide distribution as a landslide concentration (LC), which is defined as the number of landslides per square kilometer

of surface area (Keefer 2000). The rock slopes in the area affected by the earthquake are mainly sedimentary, igneous, and metamorphic rocks of Precambrian to Quaternary ages (Sato et al. 2007). Landslides occurred most frequently in the Tertiary-age Murree Formation (Tmm) which consists of hard sandstone and siltstone with thin intraformational conglomerate lenses (Sato et al. 2007). Kamp et al. (2008) described the failed sedimentary rocks as undeformed to tightly-folded, highly-cleaved and fractured.

To perform a pseudo-static slope stability analysis, a number of rock properties are needed, as well as geometric properties of the slope. For individual slopes, these values are evaluated as part of a site characterization program. However, for this study, we are interested in the regional performance of rock slopes; therefore, we are characterizing these parameters in terms of typical mechanical and geometric properties that apply to the affected region as a whole. The rock properties needed for the analysis are unit weight, γ'; and shear strength (characterized in terms of Mohr-Coulomb parameters ϕ' and c'). The geometric parameters needed are D and i (defined above). Because Mohr-Coulomb strength properties for rock specimens are rarely measured directly (other than for joints), we opted to use the Hoek-Brown strength criterion (Hoek et al. 2002) to estimate the Mohr-Coulomb strength parameters. The Hoek-Brown criterion requires the following parameters (Hoek et al. 2002): rock uniaxial compressive strength (σ_c); a material constant for intact rock, m_i; the Geological Strength Index, GSI; and a disturbance factor, DF, that accounts for the degree of disturbance to the rock mass from blasting and/or stress relief. We estimated these parameters from the reported geologic and geotechnical conditions in the affected region. The Hoek-Brown strength parameters were then converted to equivalent Mohr-Coulomb shear strength parameters over the appropriate effective confining stress range for use in the pseudo-static slope stability analysis.

As discussed by Hoek et al. (2002), the degree of weathering plays an important role in estimating rock strength parameters. Sato et al. (2007) reported that 79% of the landslides were shallow, disrupted rockslides, and Owen et al. (2008) observed that these shallow landslides typically involved the top few meters of weathered bedrock, regolith, and soil. From these descriptions, Table 7-1 includes the estimated geometric parameters for this landslide.

Based on the observation by Owen et al. (2008), we considered D = 2, 3, and 4 m. Figure 7-2(a) shows the distribution of slope angles for slope that failed during the 2005 Kashmir earthquake (Kamp et al. 2008). We considered a normal distribution with a mean slope angle of 28.1° and a standard deviation of 10° to represent the failed slope data. Table 7-1 summarizes the geometric parameters for this case. For subsequent statistical analysis, we used normal distributions for all of these parameters; therefore, mean (μ) and standard deviation (σ) listed in Table 7-1 were assigned weights of 0.2 (μ - σ), 0.6 (μ), and 0.2 (μ + σ), respectively. For the Mohr-Coulomb strength parameters, we assumed that the values computed using the Hoek-Brown criterion were mean values, and standard deviations were estimated using coefficient of variation (COV) of 5%, 30%, and 15% for γ, c', and ϕ', respectively, as suggested by Lee et al. (1983). Therefore, the Hoek-Brown parameters in Table 7-1 for the Kashmir earthquake case yield $\phi' = 40.3 \pm 6.0°$ and $c' = 26.6 \pm 8.0$ kPa.

Figure 7-3 shows the horizontal ground accelerations predicted using four attenuation relationships released by Next Generation Attenuation (NGA) projects (Abrahamson and Silva 2008; Boore and Atkinson 2008; Campbell and Bozorgnia 2008; Idriss 2008). Figure 7-4 compares the mean factor of safety against sliding using all material properties and slope geometries, and predicted horizontal ground accelerations for 2005 Kashmir earthquake with the LC data by Sato et al. (2007). The static FS was calculated to be approximately 2.7. When the

horizontal acceleration was incorporated, the FS becomes 1.5 at distances close to the fault. The mean FS did not become smaller than unity even when the horizontal acceleration was at its maximum. Although some combinations of material properties and slope geometries cause the FS to become smaller than unity, this mean FS distribution cannot explain the high LC near the fault. We observed similar disparity between the LC data and pseudo-static FS when using mean strength and geometry parameters for the 1989 Loma-Prieta, U.S.; 1999 Chi-Chi, Taiwan; and 2008 Wenchuan, China, earthquakes.

Table 7-1 Hoek-Brown parameters and geometry parameters for four cases.

Parameter	Selected values				Notes	References
	2005 Kashmir	1989 Loma-Prieta	1999 Chi-Chi	2008 Wench-uan		
γ (kN/m^3)	21 ± 1	21 ± 1	24 ± 1.2	24 ± 1.2	Estimated from rock type and degree of weathering	Hoek and Bray (1981)
σ_c (MPa)	2	0.8	2	2	Estimated from rock type and degree of weathering	Hoek et al. (1998)
m_i	14	14	14	10	Estimated from rock type	Hoek et al. (1998)
GSI	30	30	30	30	Estimated from rock type, rock mass structure, and joint surface conditions	Hoek (2005)
DF	0	0	0	0	No evidence of blasting or stress relief	Hoek et al. (1998)
ϕ' (°)	40.3 ± 6.0	32.8 ± 5.0	51.1 ± 7.7	40.3 ± 6.0	Estimated using Hoek-Brown criterion	Hoek et al. (2002)
c' (kPa)	26.6 ± 8.0	19.9 ± 6.0	10.6 ± 3.2	26.6 ± 8.0	Estimated using Hoek-Brown criterion	Hoek et al. (2002)
σ_t (kPa)	0.73 ± 0.15	0.36 ± 0.07	0.73 ± 0.15	0.73 ± 0.15	Estimated using Hoek-Brown criterion	Hoek et al. (2002)
D (m)	3 ± 1	3 ± 1	0.7 ± 0.3	3 ± 1	Based on generalized description of typical depths of disrupted slides in rock slopes	Keefer (1984) Khazai and Sitar (2003) Owen et al. (2008) Yin et al. (2010)
i (°)	28.1 ± 10	27.0 ± 10	65.0 ± 15	32.5 ± 12	See Figure 2	Khazai and Sitar (2004) Kamp et al. (2008) Yin et al. (2010)

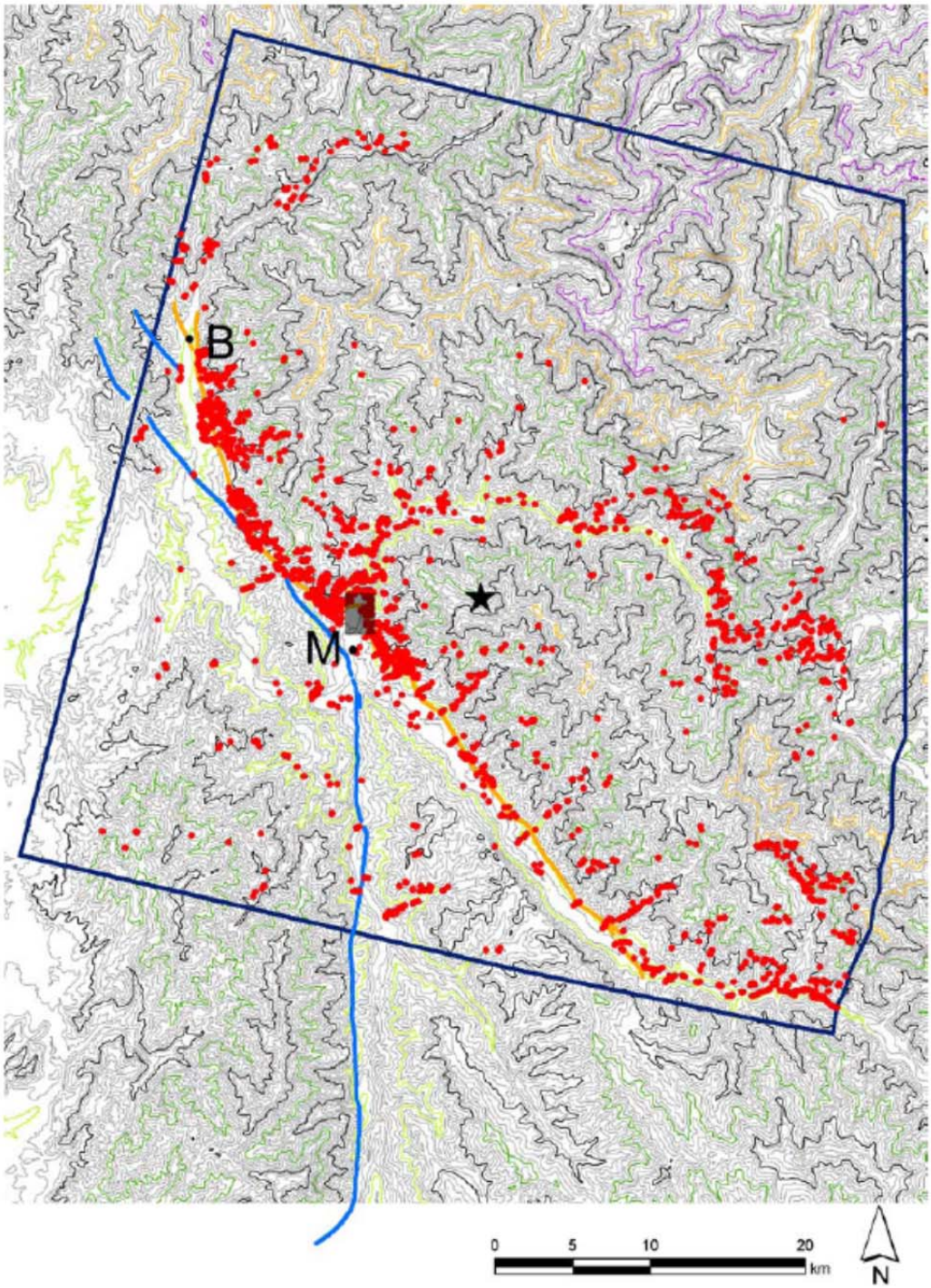

Figure 7-1 Distribution of landslides triggered by the 2005 Kashmir earthquake, shown as red dots. Epicenter (star mark), Balokot-Garhi fault (Green line), Jhelum fault (blue line), and cities of Muzaffarabad (M) and Balakot (B) are also shown. (Sato et al. 2007).

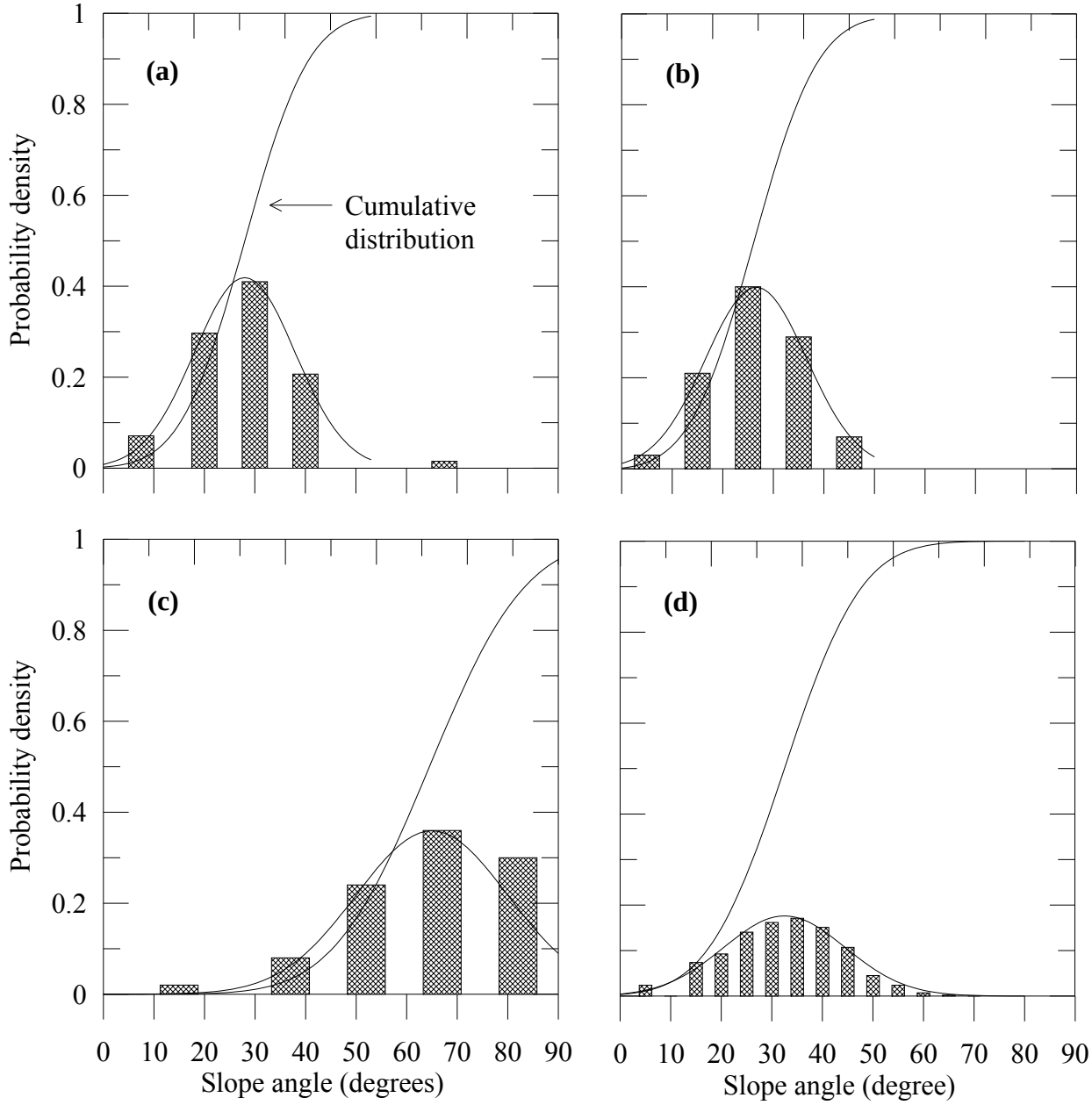

Figure 7-2 Distribution of slope angles for (a) 2005 Kashmir, Pakistan, earthquake (Kamp et al. 2008), (b) 1989 Loma Prieta earthquake (Khazai and Sitar 2004), (c) 1999 Chi-Chi, Taiwan, earthquake (Khazai and Sitar 2004), and (d) 2008 Wenchuan, China, earthquake (Yin et al. 2010).

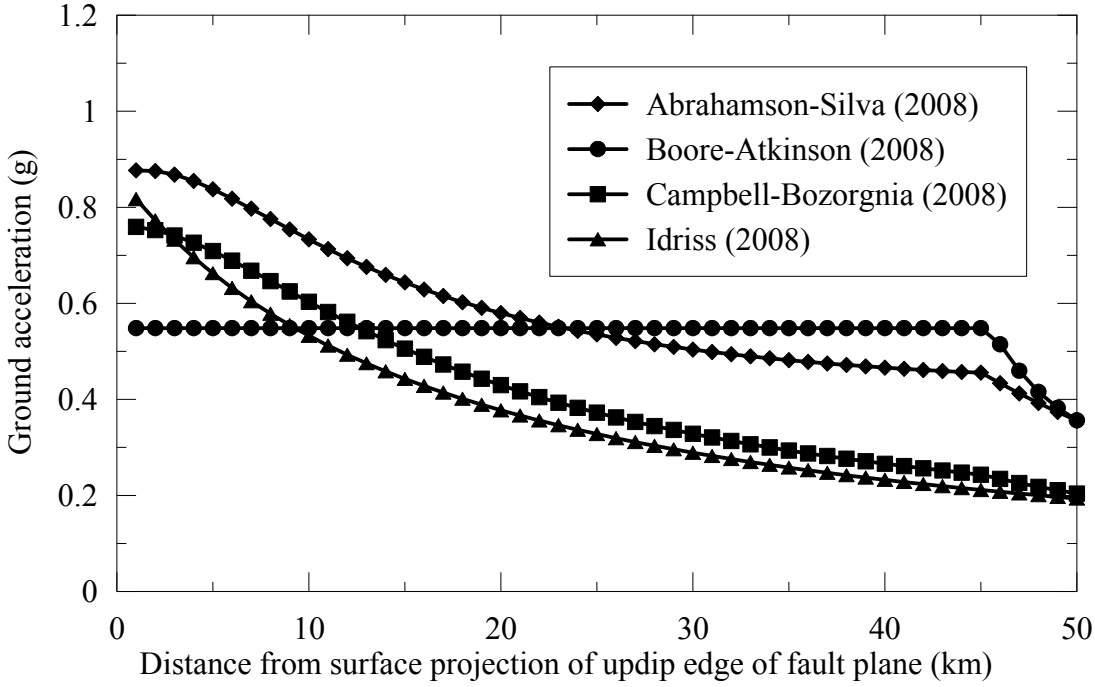

Figure 7-3 Horizontal accelerations with respect to source-to-site distance predicted using the NGA GMPEs for the M_w 7.6 Kashmir, Pakistan, earthquake.

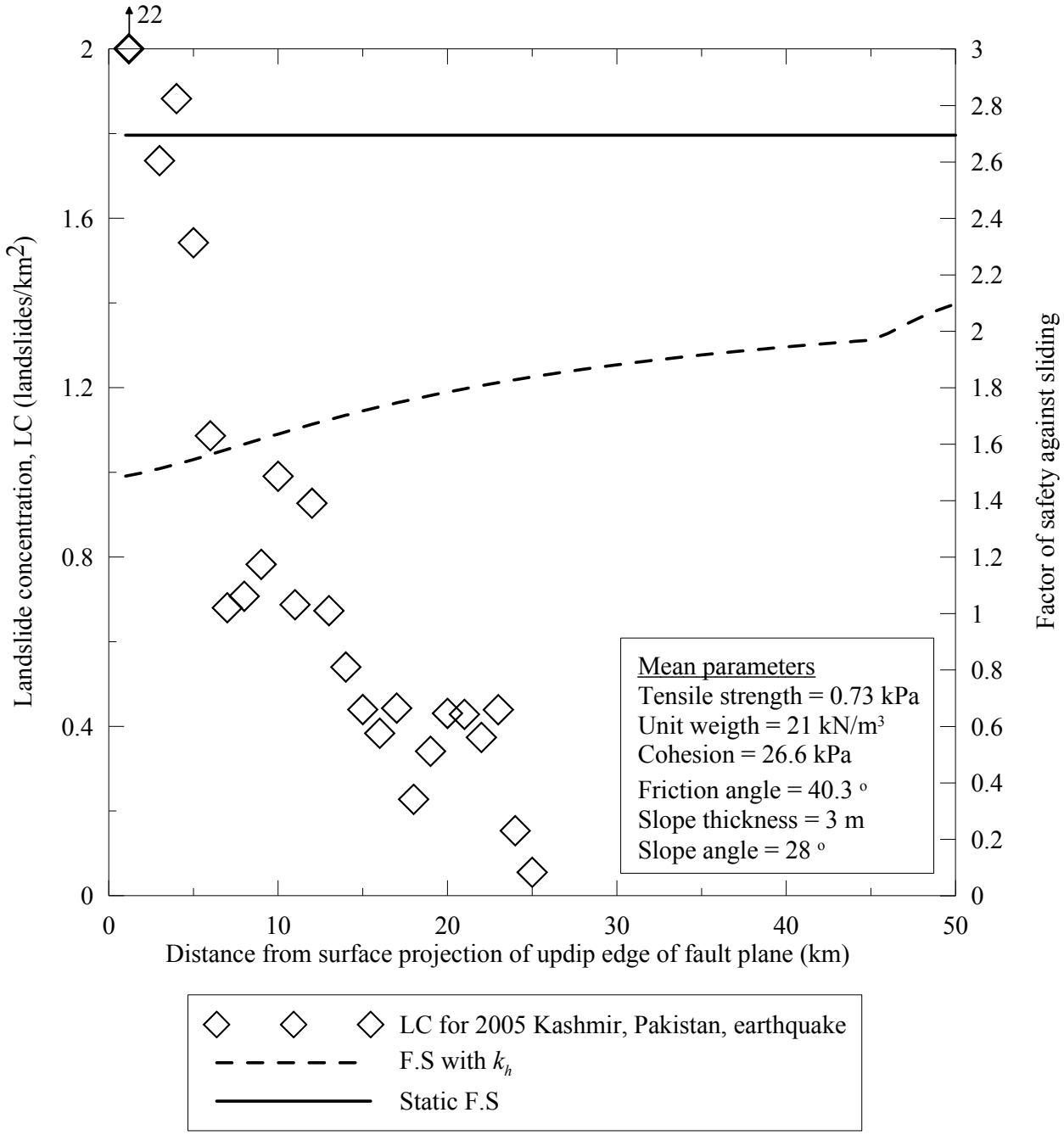

Figure 7-4 Landslide concentration data for the 2005 Kashmir, Pakistan, earthquake by Sato et al. (2007) and the mean factor of safety calculated by using existing pseudo-static method.

CHAPTER 8. FACTORS THAT AFFECT PSEUDO-STATIC SLOPE STABILITY

We examined three factors that potentially would affect LC near earthquake source zones in addition to the horizontal acceleration: vertical ground acceleration, topographic effects, and "bond break" effect.

8.1 Incorporating vertical acceleration into pseudo-static analysis

Vertical accelerations traditionally have been ignored in pseudo-static slope stability analyses because it is believed to have little influence on slope stability because it reduces both the driving and resisting forces. For a typical set of strength and geometric properties, Figure 8-1 shows that the vertical pseudo-static coefficient (k_v) actually increases the FS when k_h is smaller than 0.2. However, when k_h exceeds 0.2, k_v decreases the FS. In addition, k_v tends to increase the FS when the sliding mass is thinner and the slope is steeper, regardless of k_h, while k_v decreases the FS when the sliding mass is thicker and the slope is gentler (assuming constant strength parameters with depth).

In addition to the direct effect of k_v, many researchers have reported that the maximum vertical acceleration can equal or exceed the horizontal acceleration close to the causative fault, particularly for large magnitude earthquakes. To evaluate vertical accelerations, some researchers, e.g, Campbell and Bozorgnia (2003) and Ambraseys et al. (2005), have proposed vertical acceleration attenuation relationships; however, these methods are limited by a lack of recorded ground motions. Despite this limitation, they used available strong-motion data for shallow crustal earthquakes recorded throughout the world (Campbell and Bozorgnia 2003) and in Europe and the Middle East (Ambraseys et al. 2005). Other researchers have proposed relationships between horizontal and vertical accelerations. For example, Figure 8-2 presents vertical-to-horizontal acceleration ratios proposed by Ambraseys and Simpson (1996) and

Elnashai and Papazouglou (1997). The Ambraseys and Simpson (1996) relation is based on 110 near-field recordings (d < 15 km) relatively large (surface wave magnitude, Ms > 6), shallow (h < 20 km), interplate earthquakes. They suggested that V/H slightly exceeds 1 for source-to-site distances less than about 5 km for large thrust fault ruptures and for moderate-to-strong strike-slip events. We linearly extrapolate their relations for reverse fault to a distance of 50 km. Elnashai and Papazouglou (1997) proposed relations that adopted Ambraseys and Simpson (1995) for distances to the fault less than 15 km, Abrahamson and Litehiser (1989) for distances larger than 30 km, and a linear interpolation for distances between 15 km and 30 km. (see Figure 8-2). The V/H ratio slightly exceeded 1.0 for near-field stations and $M_s \geq 7.5$ earthquakes. These studies illustrate that vertical motions can significantly decrease pseudo-static slope stability in the near vicinity of a fault capable of producing large magnitude earthquakes.

8.2 Topographic effects

It is well known that seismic waves can be amplified or deamplified when propagated through a soil column, depending on soil properties. This is termed 1D site effects. Seismic waves can also be either amplified or deamplified due to constructive and destructive interference when the waves encounter surface topographic irregularities such as valleys, peaks, and plateaus. This phenomenon is termed topographic effects or 2D site effects.

In many settings, waves constructively interfere near the crest of a slope. For example, during the 1971 San Fernando, California earthquake (M_w 6.6), severe ground cracking was observed in a very restricted area at the top of a ridge while no significant slope failures occurred (Nason 1971). Similarly, Castellani et al. (1982) observed that during the Irpinia, Italy, earthquake (M_w 6.9), building damage was concentrated around the top of a hill, while the village at the foot of the hill was only slightly damaged.

These observations led to several full-scale field studies evaluating topographic effects where aftershocks were monitored along particular hills or ridges (e.g., Celebi 1987; Hartzell et al. 1994; Graizer 2009). Recently Hough et al. (2010) investigated the topographic effect using the aftershocks of 2010 M7.0 Haiti earthquake. However, in many of these cases 1D site effects cannot be conclusively distinguished from topographic effects. Therefore, some laboratory shaking table and centrifuge studies have been performed to evaluate topographic effects, (e.g., Kovacs et al. 1971; Stamatopoulos et al. 2007).

Many numerical studies have been conducted to investigate topographic effects, including studies by Idriss and Seed (1967), Boore (1972), Smith (1975), Sanchezsesma et al. (1982), Sitar and Clough (1983), Ashford et al. (1997), Ashford and Sitar (1997), and Bouckovalas and Papadimitrious (2005). Many recent studies have addressed specific observations or recordings. For example, Gazetas et al. (2002), Assimaki and Gazetas (2004), and Assimaki et al. (2005) evaluated topographic effects observed during the 1999 Athens, Greece, earthquake (M_w 5.9). Lungarini et al. (2005) used the finite element method to simulate topographic effects observed at Mt. Etna, Italy and observed that the maximum computed displacement occurred at or near the peak of the mountain.

The topographic horizontal amplification factors observed in these field and numerical studies are summarized in Figure 8-3. Results reported in terms of velocity and displacement were not included in Figure 8-3. Some studies defined the amplification factor as the ratio of $a_{h,\max}$ at crest to $a_{h,\max}$ at free field beyond the crest. The others used the ratio of $a_{h,\max}$ at crest to $a_{h,\max}$ at toe. We made no distinction between these two definitions of amplification factors assuming that $a_{h,\max}$ at free filed beyond the crest and $a_{h,\max}$ at toe are the same for a rigid homogeneous rock. Figure 8-3 also includes the topographic amplification factors recommended

by the European Seismic Code provision (EC8 2000) and French Seismic Code provision (French Association for Earthquake Engineering (AFPS) 1995).

Some of the studies mentioned above also examined topographic amplification factors for vertical accelerations (e.g., Idriss and Seed 1967; Smith 1975; Sitar and Clough 1983; Ashford and Sitar 1997; Ashford et al. 1997; Assimaki et al. 2005; Bouckovalas and Papadimitriou 2005). However, all of these studies considered the response of vertical acceleration that was transformed from a horizontal input motion (i.e., no vertical input acceleration was included). Celebi (1991) reported vertical topographic amplification factors from 0.91 to 1.86 during aftershocks of the 1983 Coalinga, California, earthquake (M_w=6.5). Based on numerical simulations, Zhao and Valliappan (1993) reported topographic amplification factors of 1.5 to 1.8 for the response of various topographies to vertically-incident P-waves, These values are reasonably consistent with the horizontal topographic amplification factors reported in Figure 8-3; therefore, we assumed that vertical topographic amplification factors equaled horizontal topographic amplification factors.

Most of the shallow, disrupted landslides examined in this study were initiated near slope crests, we considered topographic amplification factors near the crest only. As illustrated in Figure 8-3, horizontal (and assumed vertical) topographic amplification factors range from about 1.1 to 1.9, depending on slope height, slope angle, and incident wave angle, with a median value of about 1.5. To account for variability, we used horizontal and vertical topographic factors of 1.3, 1.5, and 1.7 in the statistical analyses (described subsequently) with weights of 0.2, 0.6, and 0.2, respectively.

8.3 Potential bond break effect associated with vertical acceleration

Figure 8-4 (a) schematically illustrates the forces involved in a static infinite slope (side forces were assumed to be equal and opposite, and therefore were not included). When an earthquake occurs, the P-waves result in vertical surface accelerations and potentially can "break" weak bonds (i.e., cementation or cohesion) if the pseudo-static vertical acceleration exceeds the slice weight and tensile force along the base of the slice (Figure 8-4 b).

Using force equilibrium (Figure 8-4 b), bond break occurs when:

$$F_v \geq \sigma_t \times l \times \cos i + W \qquad \text{Eq. 19 (1)}$$

$$a_{v,\max} / g \geq \frac{\sigma_t \times \cos i}{\gamma \times D} + 1 \qquad \text{Eq. 19 (2)}$$

where F_v is the vertical pseudo-static force, equal to $k_{bond} \times a_{v,max} \times W$. The term k_{bond}, is taken as 1.0 based on the assumption that the maximum acceleration will progressively occur at a slope and potentially break any bond forces along the entire base of the sliding mass. As discussed earlier, we considered topographic amplification factors near the crest only because most of the shallow, disrupted landslides examined in this study were initiated near slope crests. If the bond forces within the rock mass are broken, the rock cohesion is considered to be zero for the pseudo-static stability calculations.

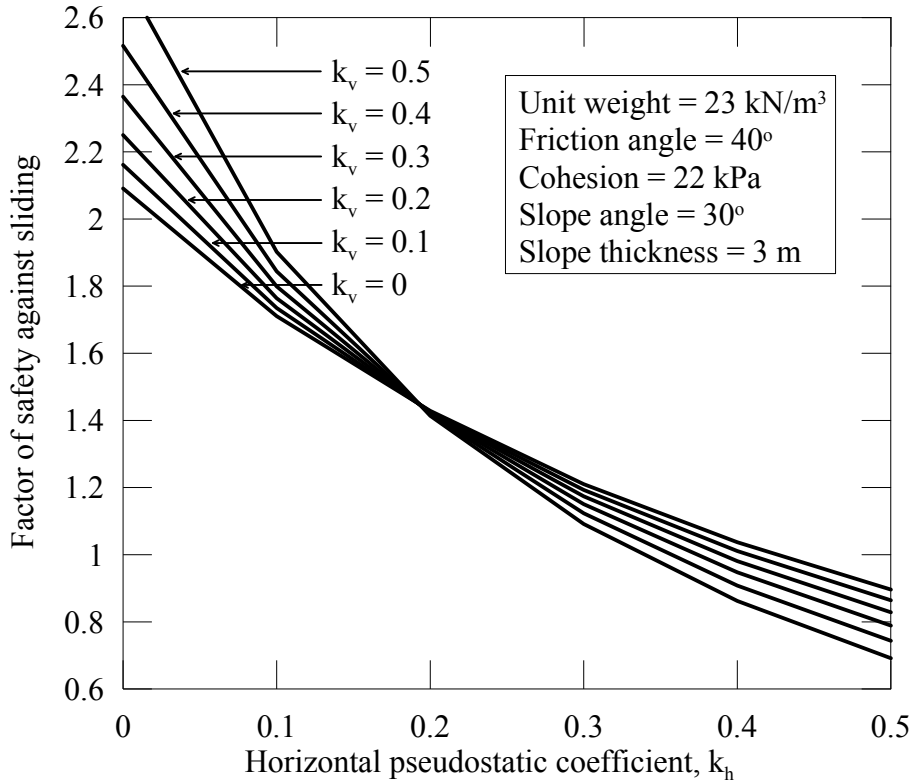

Figure 8-1 Pseudo-static FS computed using various combinations of horizontal and vertical pseudo-static coefficient, k_h and k_v. Strength and geometric properties represent typical values listed in Table 7-1.

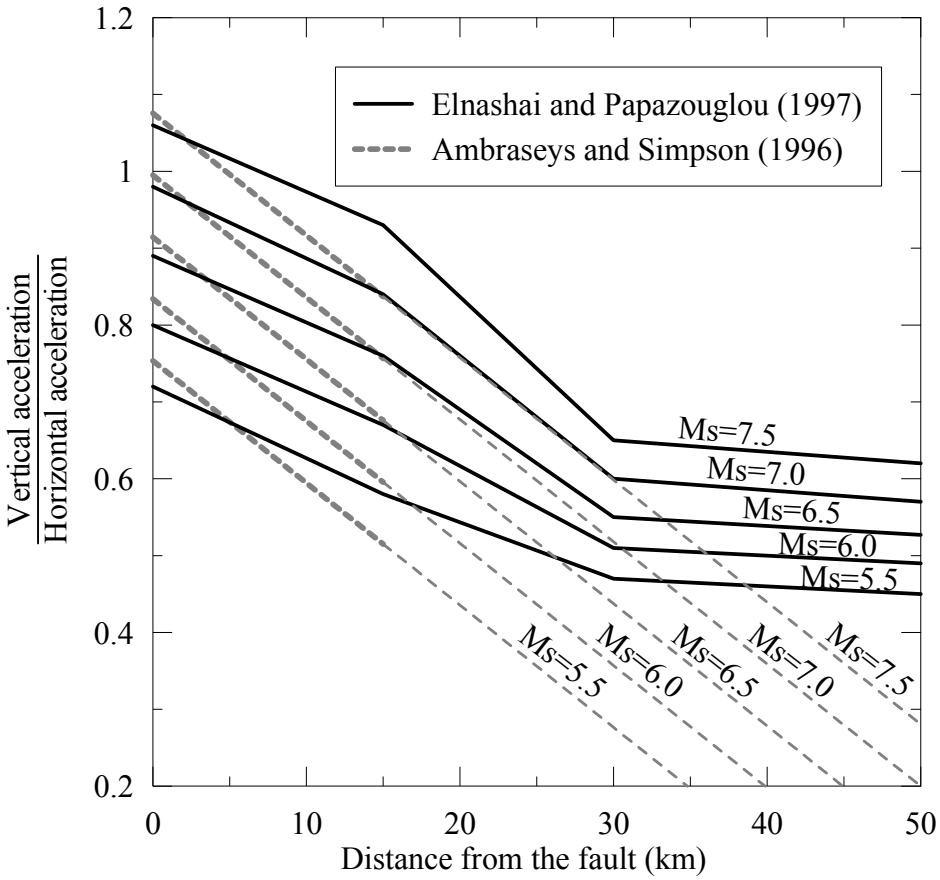

Figure 8-2 Vertical-to-horizontal acceleration ratio for thrust faults by Elnashai and Papazouglou (1997) and Ambraseys and Simpson (1996). Extrapolated portion from Ambraseys and Simpson (1996) is shown in thinner lines.

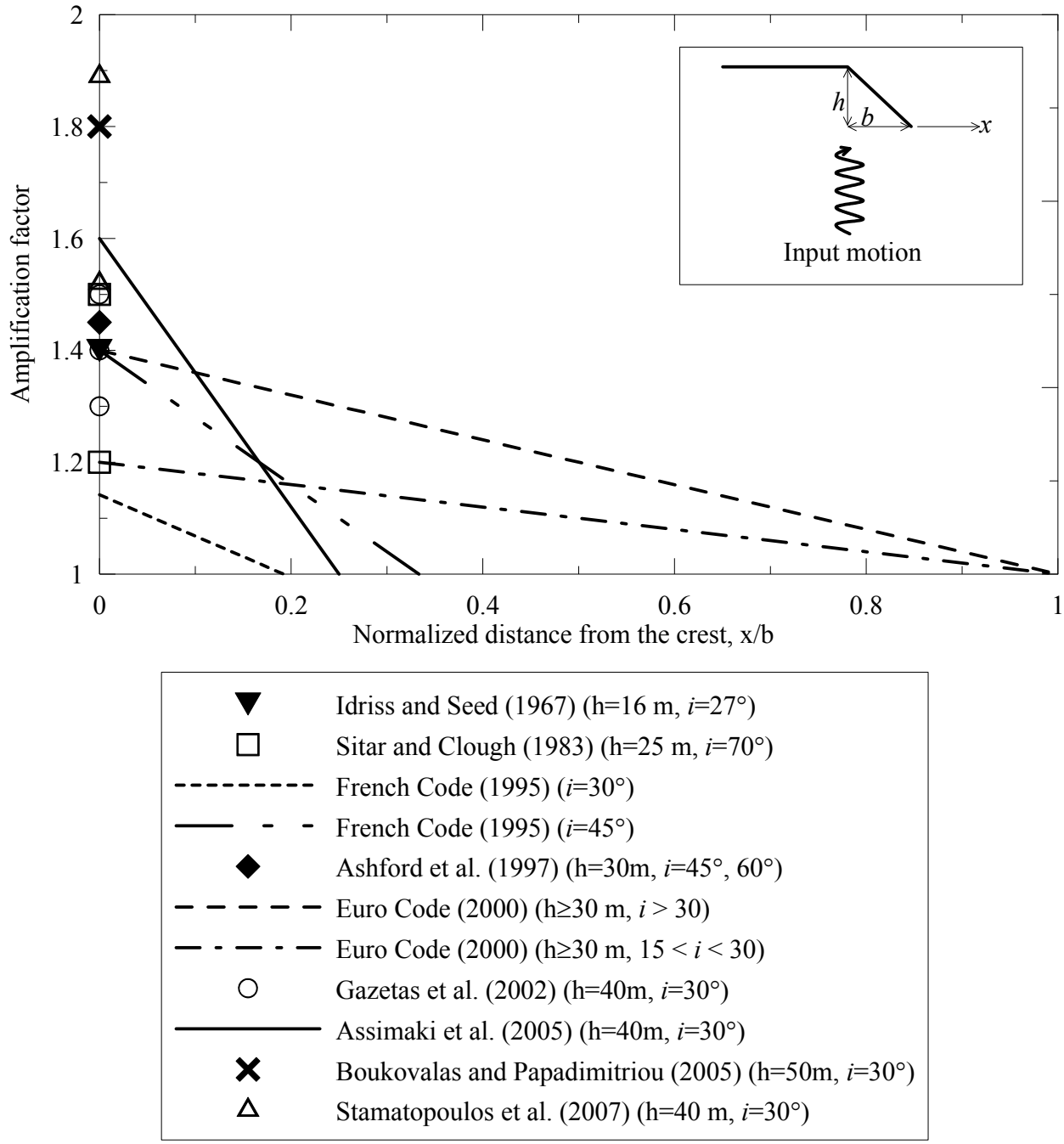

Figure 8-3 Topographic factors proposed by various researchers.

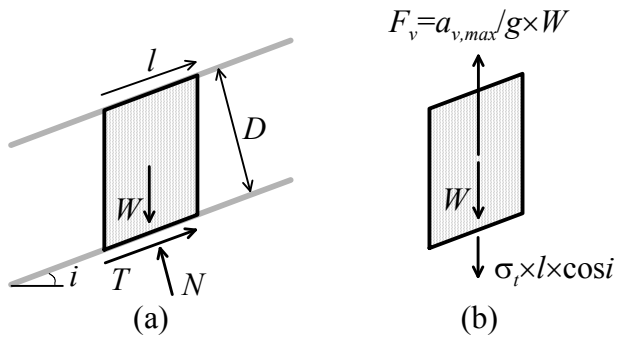

Figure 8-4 Illustration showing procedure of slope stability analysis taking account bond break effect. (a) Dimensions and forces involved in static stability, where W = slice weight; N = normal force; and T = shear force. Side forces are assumed to be equal and opposite, and therefore were not included. (b) Evaluation of "bond break" where $a_{v,max}$ = maximum vertical acceleration; σ_t = tensile strength.

CHAPTER 9. PROPOSED NEW APPROACH TO PSEUDO-STATIC SLOPE STABILITY ANALYSIS AND VERIFICATION USING EARTHQUAKE CASES

The proposed procedure for pseudo-static slope stability analysis is presented in Figure 9-1. This procedure accounts for potential vertical accelerations, topographic effects, and bond break effects. The following sections compare factors of safety predicted using the proposed pseudo-static slope stability analysis to landslide concentration data from four earthquakes. A logic tree approach was employed to perform all the calculations incorporating the uncertainties in each of the parameters. This logic tree is described below for the Loma Prieta earthquake analysis.

9.1 2005 Kashmir, Pakistan, earthquake

As mentioned earlier, vertical accelerations were predicted using two attenuation relationships (Campbell and Bozorgnia 2003; Ambraseys et al. 2005) and two vertical-to-horizontal acceleration ratios (Ambraseys and Simpson 1996; Elnashai and Papazoglou 1997). These predicted vertical accelerations for the 2005 Kashmir earthquake are shown in Figure 9-2. Table 7-1 summarizes the geometries and rock properties used in the analysis. Figure 9-3 shows the logic tree employed for the 2005 Kashmir earthquake case. The logic tree incorporates mean (μ) values and mean values ± 1 standard deviation (σ) for material properties (γ, c', ϕ', and σ_t), and slope geometry parameters (i and D). The standard deviations for material properties were estimated using coefficients of variation (COV) suggested by Lee et al. (1983), while standard deviations for the geometric parameters were based on reported slope failures (see Figure 7-2) and typical disrupted rock slide depths. For statistical analysis, we assumed that these parameters followed normal distributions. The weights assigned to each parameter are shown in parentheses in Table 7-1. The logic tree incorporates the four horizontal and four vertical acceleration attenuation relations described above, three topographic factor values, and two values of

horizontal and vertical pseudo-static coefficients. This results in 139,968 branches in the logic tree. The logic tree allows us to calculate FS for each branch individually and estimate the mean FS using the weights assigned to each branch.

Figure 9-4 shows the result of seismic slope stability analysis using the proposed procedure and logic tree approach. The mean static FS was calculated to be about 2.7, and the mean FS decreased to 1.5 near the fault when horizontal acceleration was included. The horizontal acceleration (which increases for source-to-site distances, R) clearly reduces the FS, but is not sufficient to drop the mean FS below unity. Vertical accelerations and topographic effects also did not decrease the FS below unity. However, when bond break effects were applied, the FS first decreased abruptly at R ~ 15 km, roughly consistent with the first abrupt increase in LC. At R ~ 9 km, the FS (with bond break effects) becomes smaller than unity, consistent with the second abrupt increase in LC. Finally, the mean FS becomes ~ 0.4 as R approaches zero, consistent with the large LC near the fault.

Figure 9-4 also includes the FS ± 1 standard deviation. Given the large number of variables in the logic tree, the considerable uncertainty in FS was unavoidable. To illustrate the effects of individual variable uncertainty, Figure 9-5 presents mean FS and mean FS ± 1σ for several variables involved in the FS calculation. The standard deviation for the static FS is about 1.09. However, when horizontal acceleration was considered, the standard deviation decreased to 0.51. When vertical acceleration, topographic effect, and bond break effect were included in the analysis, the standard deviation was slightly reduced. Thus, the uncertainties in the pseudo-static FS calculation do not appear to overshadow the observed trends in mean FS.

Similarly, Figure 9-6 shows the results of a sensitivity analysis for the following rock and geometric parameters: γ, ϕ', c', i, and D. Since the failed rock slopes in this study are consistently

highly weathered, the tensile strengths are estimated to be very small. Therefore, the uncertainty in tensile strength did not have much effect on FS in this study, thus the result for tensile strength is not shown here. It is notable that the variation in slope angle results in the largest standard deviation, whereas the variation of unit weight produces minor standard deviation. Another observation is that variation in FS resulting from rock and geometric parameter uncertainties decreases as R decreases. This occurs because ground accelerations have more influence on the FS as ground accelerations become larger. Figure 9-7 shows the results of a sensitivity analysis considering horizontal and vertical pseudo-static coefficients, horizontal and vertical ground accelerations, and the topographic factor. The vertical pseudo-static coefficient and vertical ground acceleration do not have much influence on the FS, while the horizontal pseudo-static coefficient, horizontal ground acceleration, and the topographic factor more significantly impact FS, especially at near-fault distances.

9.2 1989 Loma-Prieta earthquake

In 1989, a M_w 6.9 earthquake occurred in the San Francisco Bay-Monterey Bay region of California. The rupture occurred on the San Andreas Fault system with a rupture depth of 3 km to 18 km. The faulting mechanism was oblique reverse with a dip of 60° SW. The region affected by the earthquake includes a variety of sedimentary, igneous, and metamorphic rocks and unconsolidated sedimentary deposits from Jurassic through Holocene-aged (Keefer and Manson 1998). Keefer (2000) performed a statistical analysis of the distribution of 1046 landslides in the southern Santa Cruz Mountains triggered by the earthquake over an area of 192.41 km^2. The fault location and landslide distribution are shown in Figure 9-8. Approximately 74% of the 1046 landslides studied by Keefer (2000) were disrupted slides and falls, and the

majority of the 1046 landslides occurred in the Purisima Formation, a weakly-cemented sandstone and siltstone.

Keefer (2000) reported that the Purisima Formation in which most of landslides occurred consists of weakly cemented sandstones and siltstones, and the rocks are poorly to moderately indurated, and structurally deformed by pervasive folding and local faulting. Keefer and Manson (1989) also reported that disrupted landslides in all units occurred in materials that typically were weakly cemented, closely fractured, intensely weathered, and broken by joints. Based on these descriptions, Table 7-1 summarizes the Hoek-Brown parameters that we assigned for this case.

As discussed by Keefer (1984), disrupted slides and falls typically involve only the upper few meters of overburden. Therefore, we considered D = 2, 3, and 4 m. Figure 7-2 (b) shows the distribution of slope angles for slope that failed during the 1989 Loma Prieta earthquake (Khazai and Sitar 2004). We considered a normal distribution with a mean slope angle of 27° and a standard deviation of 10° to represent the failed slope data. Table 7-1 summarizes the geometric parameters for this case.

Figure 9-9 shows the result of seismic slope stability analysis using the proposed procedure and logic tree approach. The horizontal acceleration clearly reduces the FS, but is not sufficient to drop the mean FS below unity. As anticipated, the vertical acceleration alone does not have much effect on FS. Incorporating topographic effects on the horizontal acceleration significantly reduces the FS; however, the mean FS does not drop below unity until $R \leq 1$ km. This is inconsistent with the LC data, which show a significant change at $R \leq 8$ km. Incorporating topographic effects on the vertical acceleration also decreases the FS at near-source distances, but the mean FS only drops marginally below unity for $R \leq 6$ km. While the R-value where the mean FS drops below unity is consistent with the significant change in LC, the

marginal change in FS doesn't appear consistent with the abrupt increase in LC. When the bond break effect in incorporated, a fairly significant decrease in FS occurs at R ≤ 6 km. We believe that this significant decrease in mean FS is consistent with the abrupt increase in LC.

9.3 1999 Chi-Chi, Taiwan, earthquake

The 1999 Chi-Chi earthquake (M_w 7.6) occurred in the mountainous terrain of central Taiwan, and triggered more than 10,000 landslides throughout an area of approximately 11,000 km^2 (Hung 2000). The Cher-Long-Pu Fault that ruptured during this event is a thrust fault (dip = 38°, depth to the bottom of rupture = 20 km) trending from south to north (Meunier et al. 2007). Figure 9-10 shows the landslide locations along the fault zone and the geologic setting of affected area. Most of landslides were shallow, disrupted slides and falls in Tertiary sedimentary and submetamorphic rocks (Khazai and Sitar 2004). The landslide masses commonly were dry, highly disaggregated, weakly cemented, closely fractured, intensely weathered, and broken by conspicuous, highly persistent joints (Khazai and Sitar 2004). Estimated rock properties are presented in Table 7-1. Khazai and Sitar (2004) reported that the depth of sliding typically ranged from several decimeters to a meter, and Figure 7-2(c) presents the range of slope angles where the landslides occurred. The resulting geometric parameters are also summarized in Table 7-1. Using the geometric and rock properties in Table 7-1, we computed Mohr-Coulomb strength parameters of: $\phi' = 51°$ and $c' = 10.6$ kPa for the appropriate range of stresses (corresponding to D).

Figure 9-11 shows the mean FS compared to LC data collected by Khazai and Sitar (2004). Here as the result of the fairly steep slopes, the static FS was computed as 1.3, and the FS with the horizontal acceleration approaches 0.8 near the fault. However, this decrease in pseudo-

static FS does not capture the LC data trend. Furthermore, the FS increases when the vertical accelerations are included because the sliding mass is thin and the slope is steep. When topographic effects were considered, the FS decreases to unity for R ~ 25 km, which matches with the location where the first abrupt increase in LC occurs. Finally, when bond break effects were included, the FS drops to unity at R ~ 26 km, again consistent with the first slope change in LC. From R ~ 26 km to R ~ 13 km, LC increases roughly linearly, while mean FS decreases roughly linearly. At R ~ 12 km, a second abrupt change in FS occurs, consistent with the step-change in LC at R ~ 13 km. We anticipate that the LC data does not show a significant increase near the fault (even with the small FS at R < 10 km) is that slopes become gentler and more sparsely located near the fault than at some distance from the fault (Meunier et al. 2007).

9.4 2008 Wenchuan, China, earthquake

On 12 May 2008, the Wenchuan earthquake (M_w 7.9) occurred in the Sichuan Province of China. The earthquake occurred in the compression zone between the Indian and Eurasian plates along the Longmenshan-Beichuan-Yinxiu fault zone (rupture length = 300 km, rupture depth = 14 to 19 km, dip = 60°) (Cui et al. 2009).

Figure 9-12 shows the distribution of over 56,000 earthquake-triggered landslides, distributed over an area of 811 km^2. These were identified by Dai et al. (2011) using aerial photos and high-resolution satellite images. Yin et al. (2009) and Dai et al. (2011) reported that most of the landslides occurred in weathered or heavily fractured sandstone, siltstone, slate, and phyllite. Based on these descriptions, Table 7-1 summarizes the estimated rock properties. The majority of landslides were shallow, disrupted landslides and rock falls from steep slopes, typically involving the top few meters of weathered bedrock, regolith, and colluvium (Dai et al. 2011). Similarly, Yin et al. (2009) reported typical sliding depths of about 1 to 5 m and slope

angles as shown in Figure 7-2(d). From these descriptions, Table 7-1 includes the estimated geometric parameters for these landslides. The equivalent Mohr-Coulomb strength parameters were calculated as $\phi' = 32.5°$ and $c' = 26.6$ kPa for the appropriate range of stresses.

Figure 9-13 compares the mean FS to the LC data collected by Dai et al. (2011). The static FS was calculated to be 2.2, and the FS decreased to about 1.3 near the fault when horizontal accelerations were included. This mean FS is not consistent with the LC data, particularly at short source-to-site distances. While topographic effects decrease the FS below unity within 3 km of the fault, this is inconsistent with the abrupt change in LC that occurs at R ~ 10 km. However, when bond break effects were considered, the FS abruptly decreases at R ~ 15 km, and drops below unity at R ~ 11 km, consistent with the LC data. Furthermore, as R approaches zero, the FS approaches 0.3, consistent with the high LC near the fault.

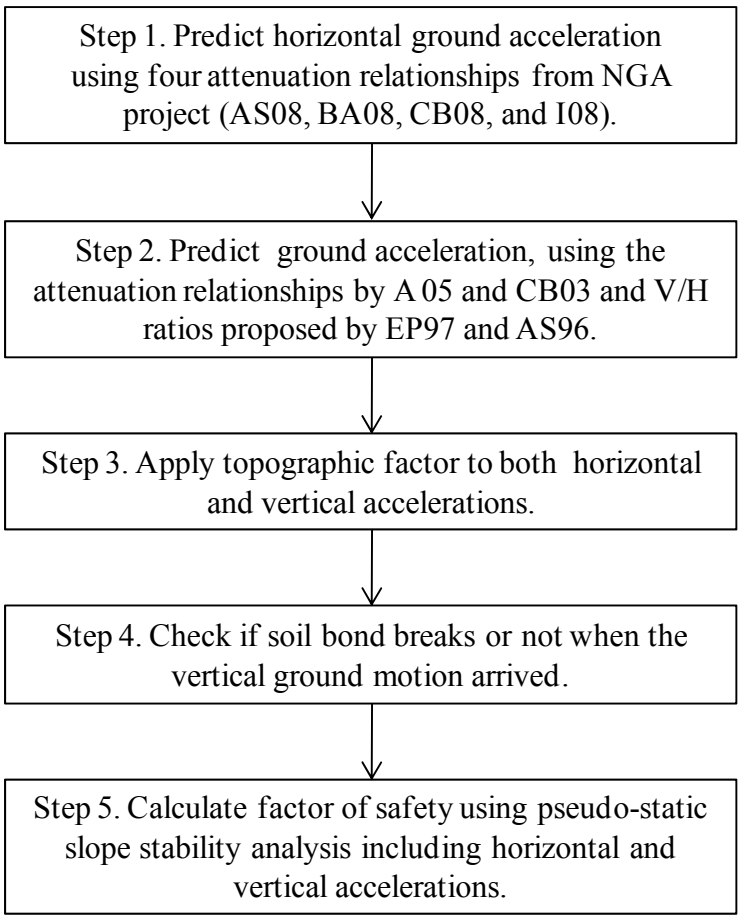

Figure 9-1 Flow chart of new approach for the pseudo-static slope stability analysis. AS08, BA08, CB08, and I 08 represent Abrahamson and Silva (2008), Boore and Atkinson (2008), and Campbell and Bozorgnia (2008), and Idriss (2008), respectively. A 05, CB03, EP97, and AS96 represent Ambraseys et al. (2005), Campbell and Bozorgnia (2003), Elnashai and Papazouglou (1997), and Ambraseys and Simpson (1996), respectively.

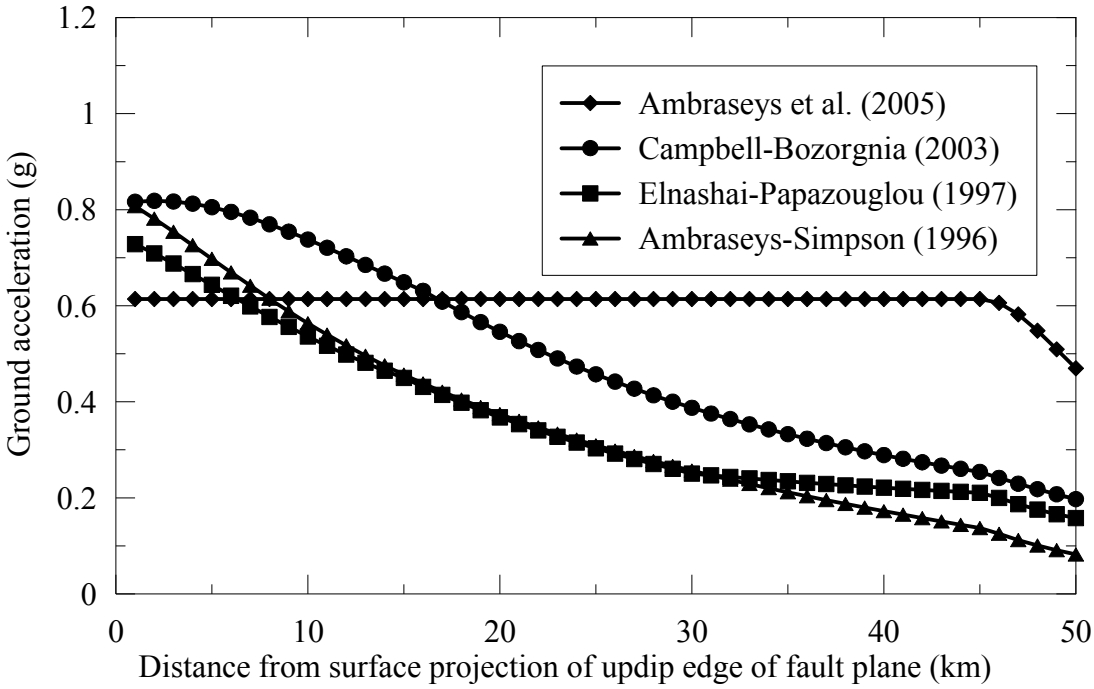

Figure 9-2 Vertical acceleration along the distance from the fault for 1989 Loma-Prieta earthquake.

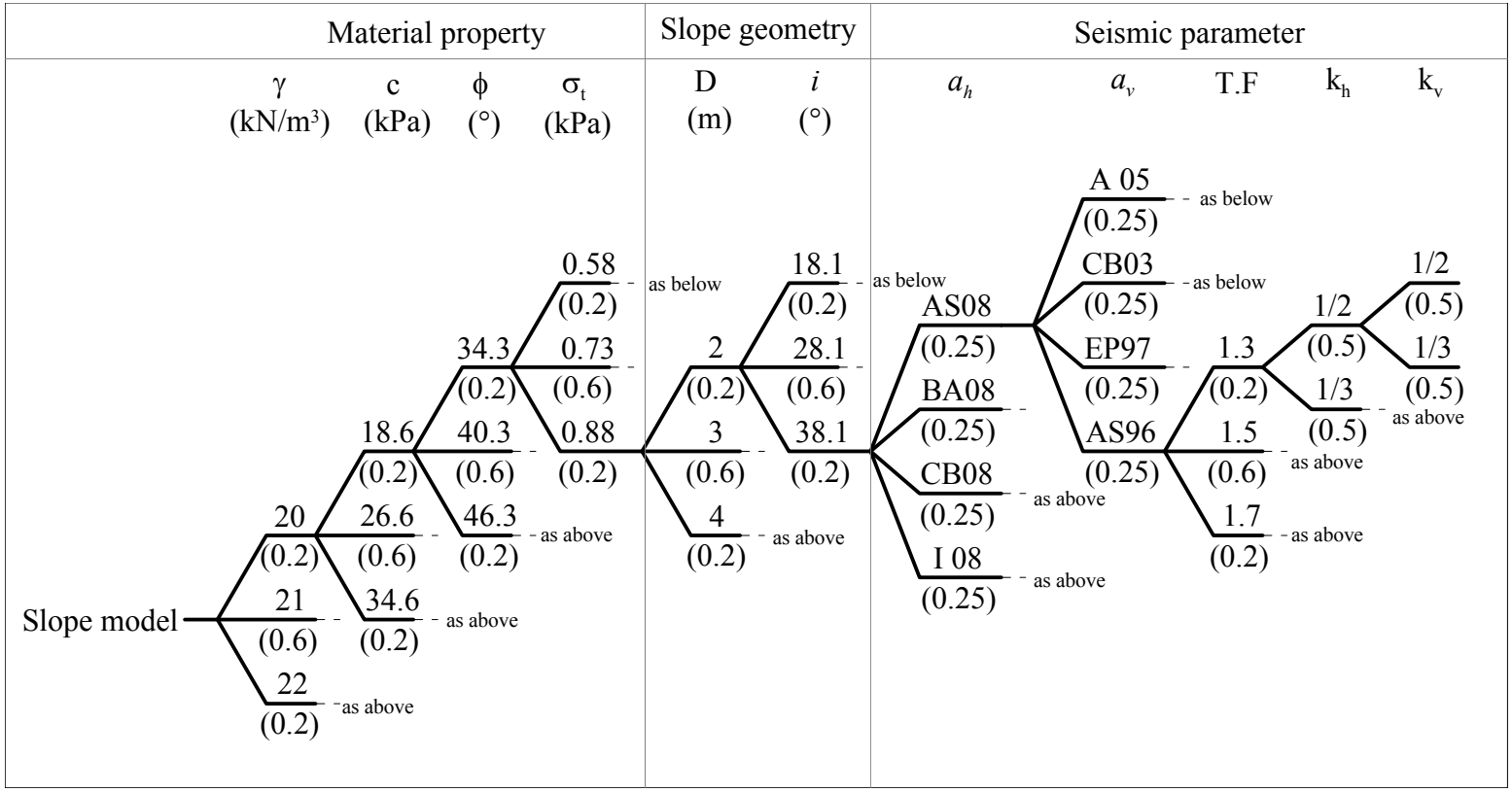

Figure 9-3 Logic tree of slope model for the case of 2005 Kashmir, Pakistan, earthquake.

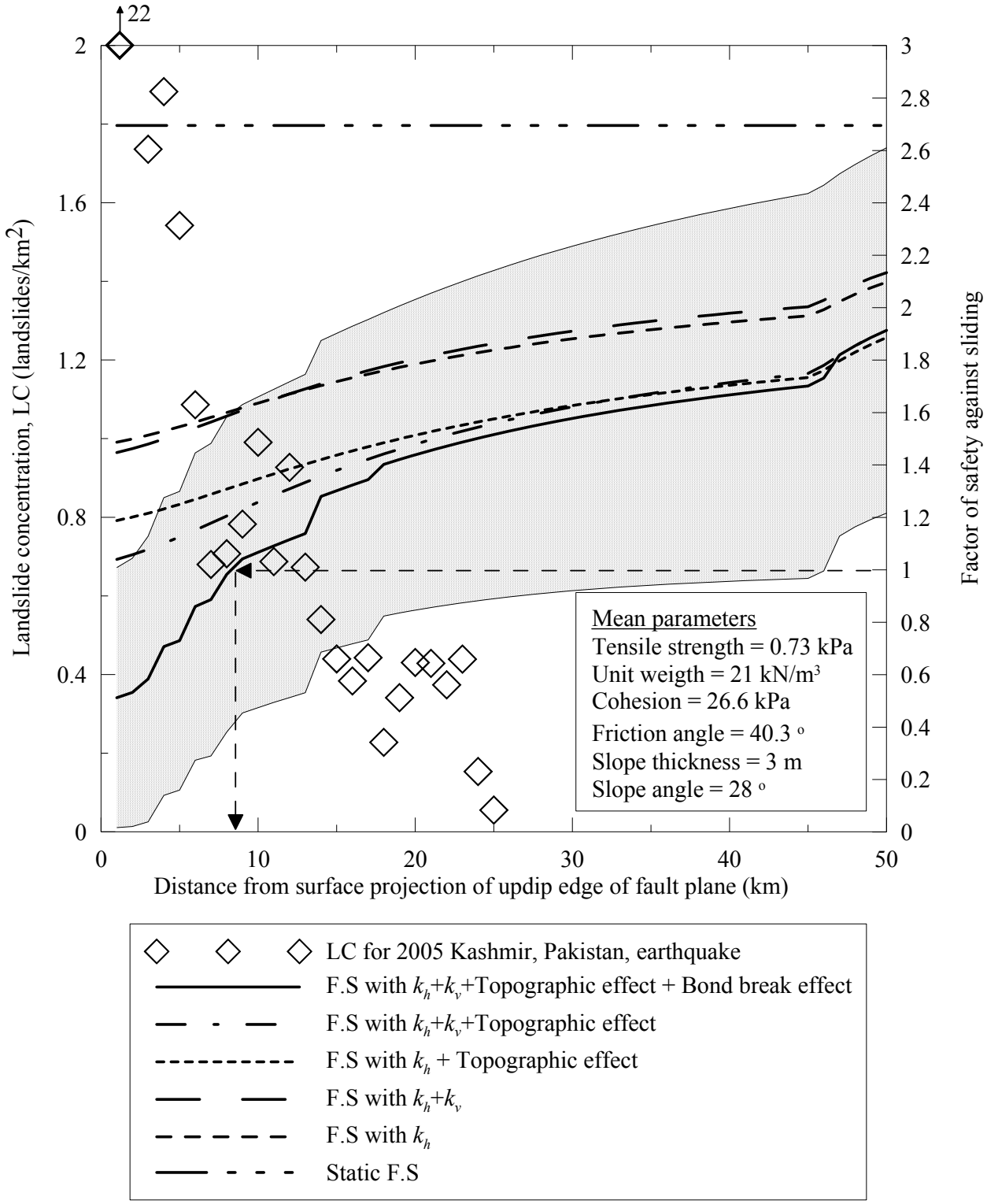

Figure 9-4 Landslide concentration data for the 2005 Kashmir, Pakistan, earthquake (Sato et al. 2007) and factor of safety calculated by using various effects.

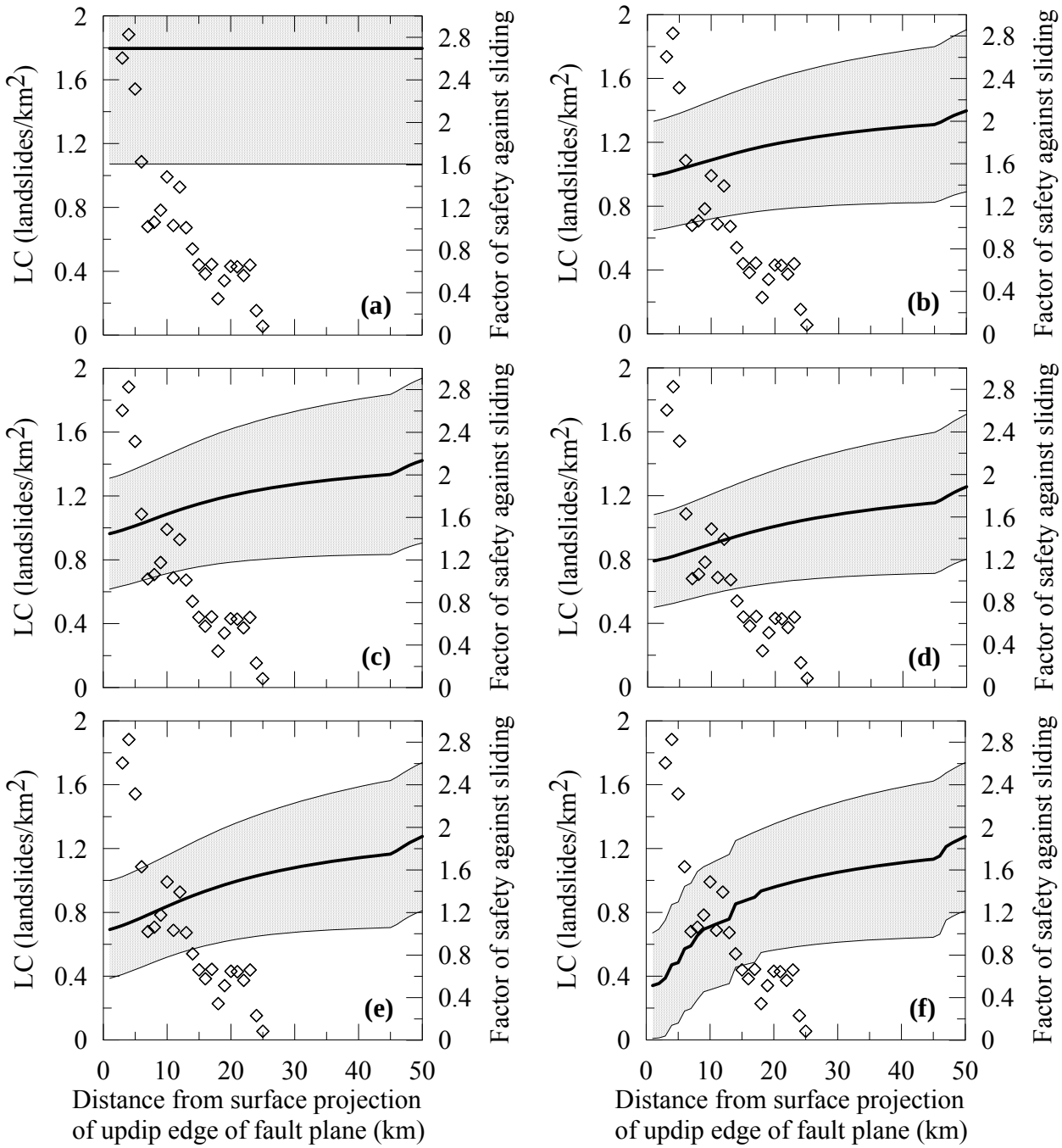

Figure 9-5 Mean factor of safety and mean ± 1 standard deviation for adding each factor: (a) static condition, (b) with horizontal acceleration (a_h), (c) with a_h and vertical acceleration (a_v), (d) with a_h and topographic effect, (e) with a_h, a_v, and topographic effect, and (f) a_h, a_v, topographic effect, and bond break effect.

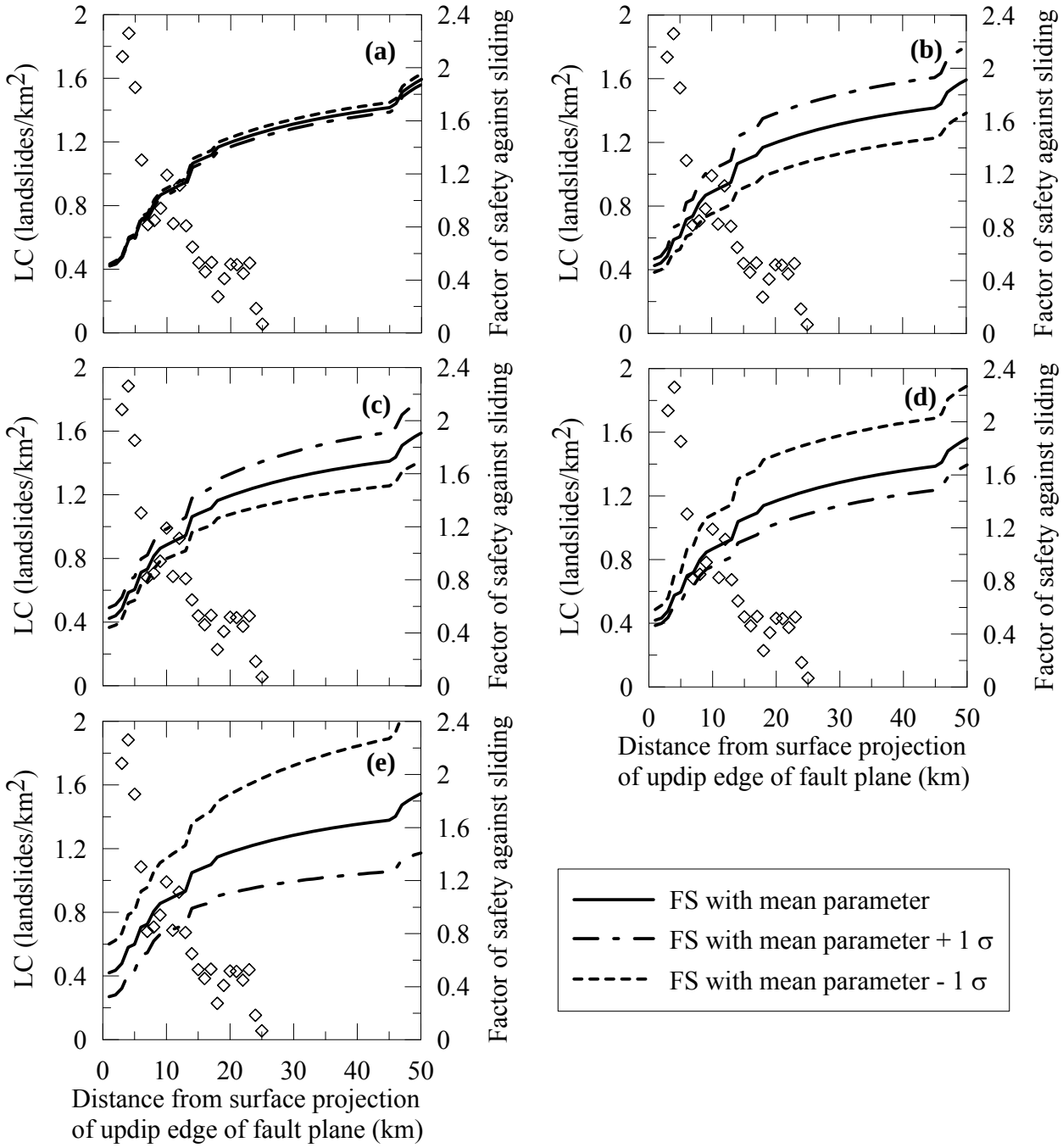

Figure 9-6 Results of sensitivity analysis for material properties and slope geometry parameters: (a) unit weight, (b) cohesion, (c) friction angle, (d) slope thickness, and (e) slope angle. Mean FS and mean FS ± 1 standard deviation (σ) are shown for each parameter.

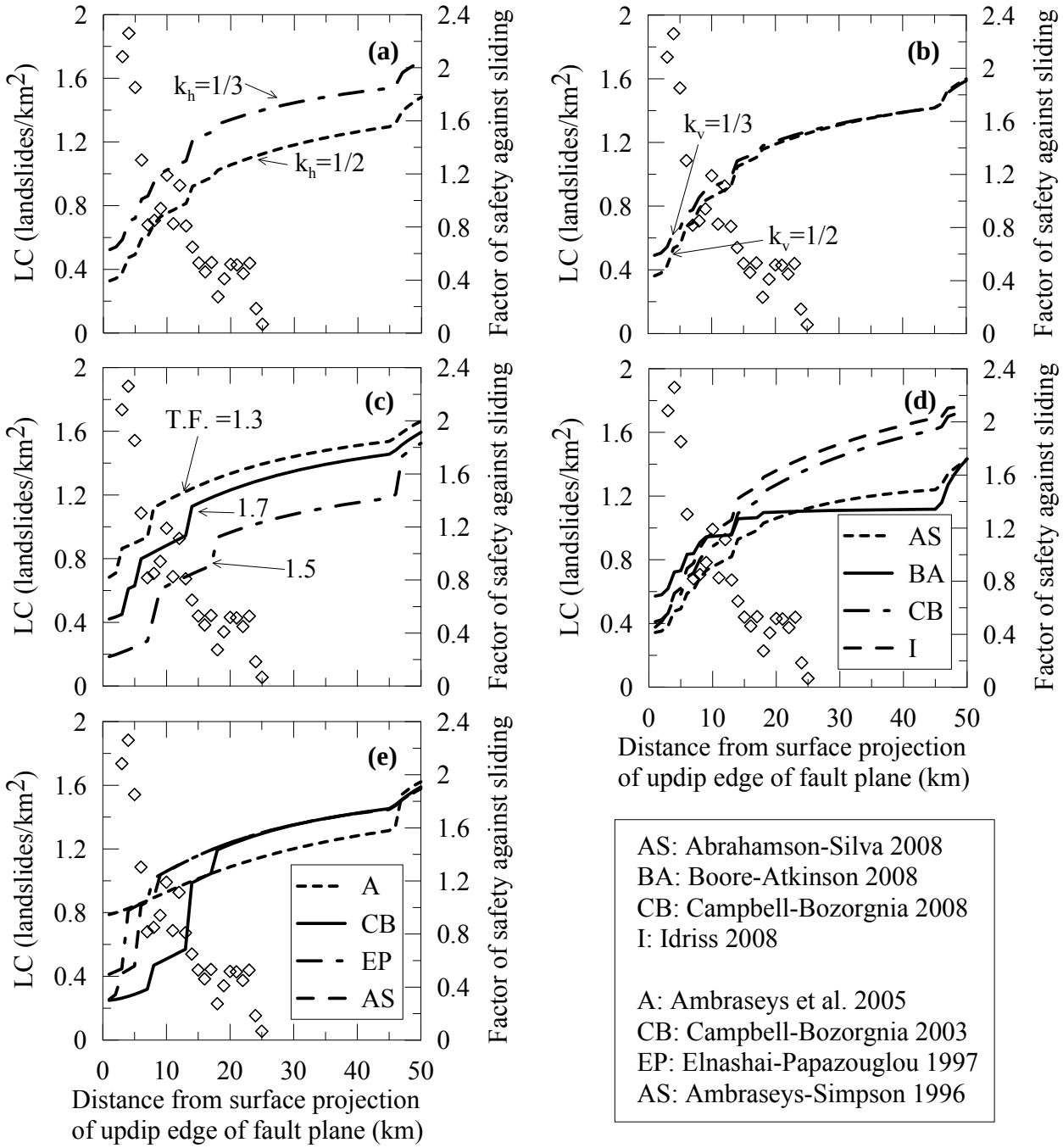

Figure 9-7 Results of sensitivity analysis for (a) k_h, (b) k_v, (c) topographic factor, (d) horizontal acceleration, and (e) vertical acceleration.

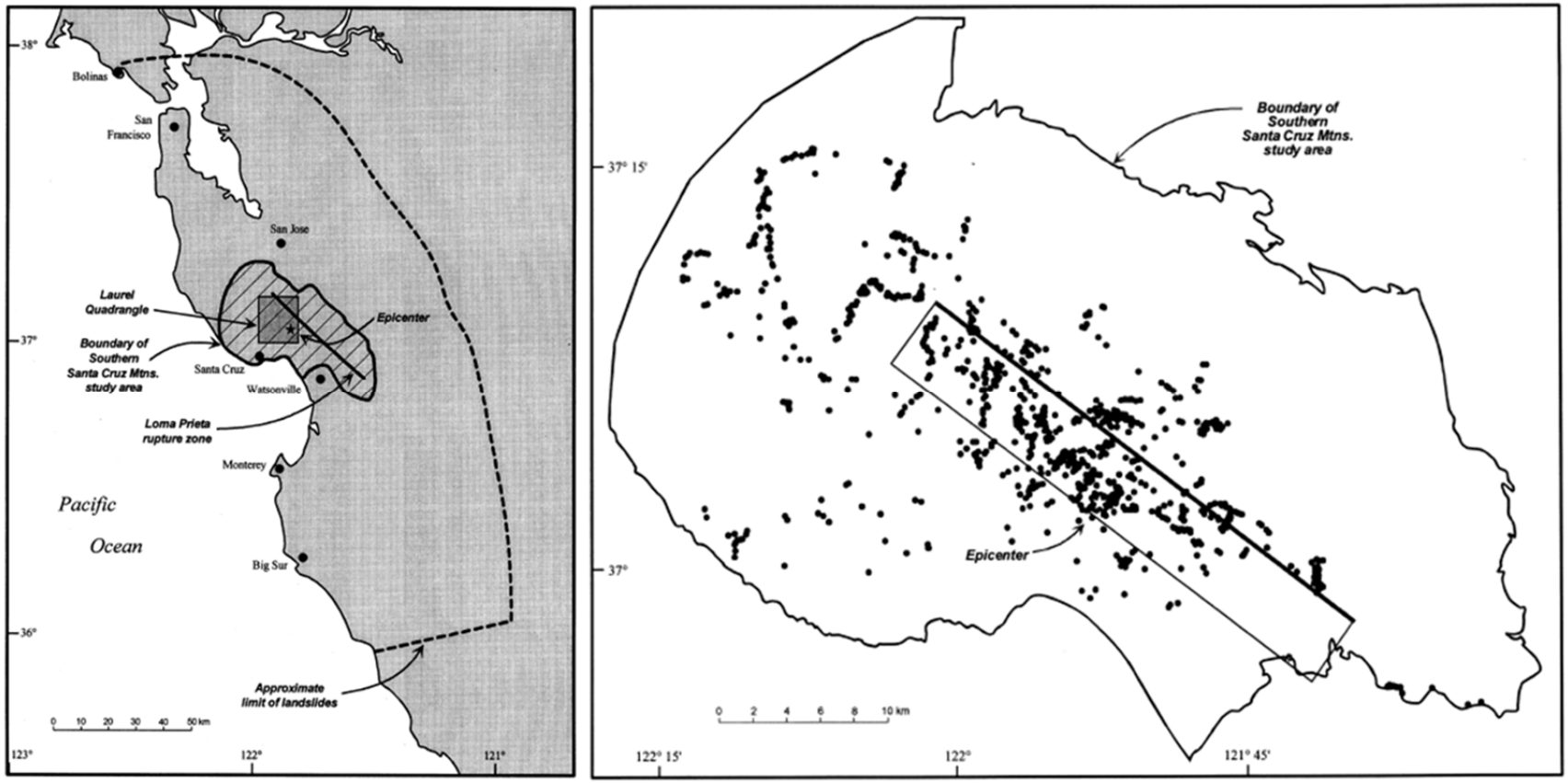

Figure 9-8 Limits of southern Santa Cruz Mountains landslide area (left) and locations of earthquake-induced landslides with the surface projection of fault rupture (right) (Keefer 2000)

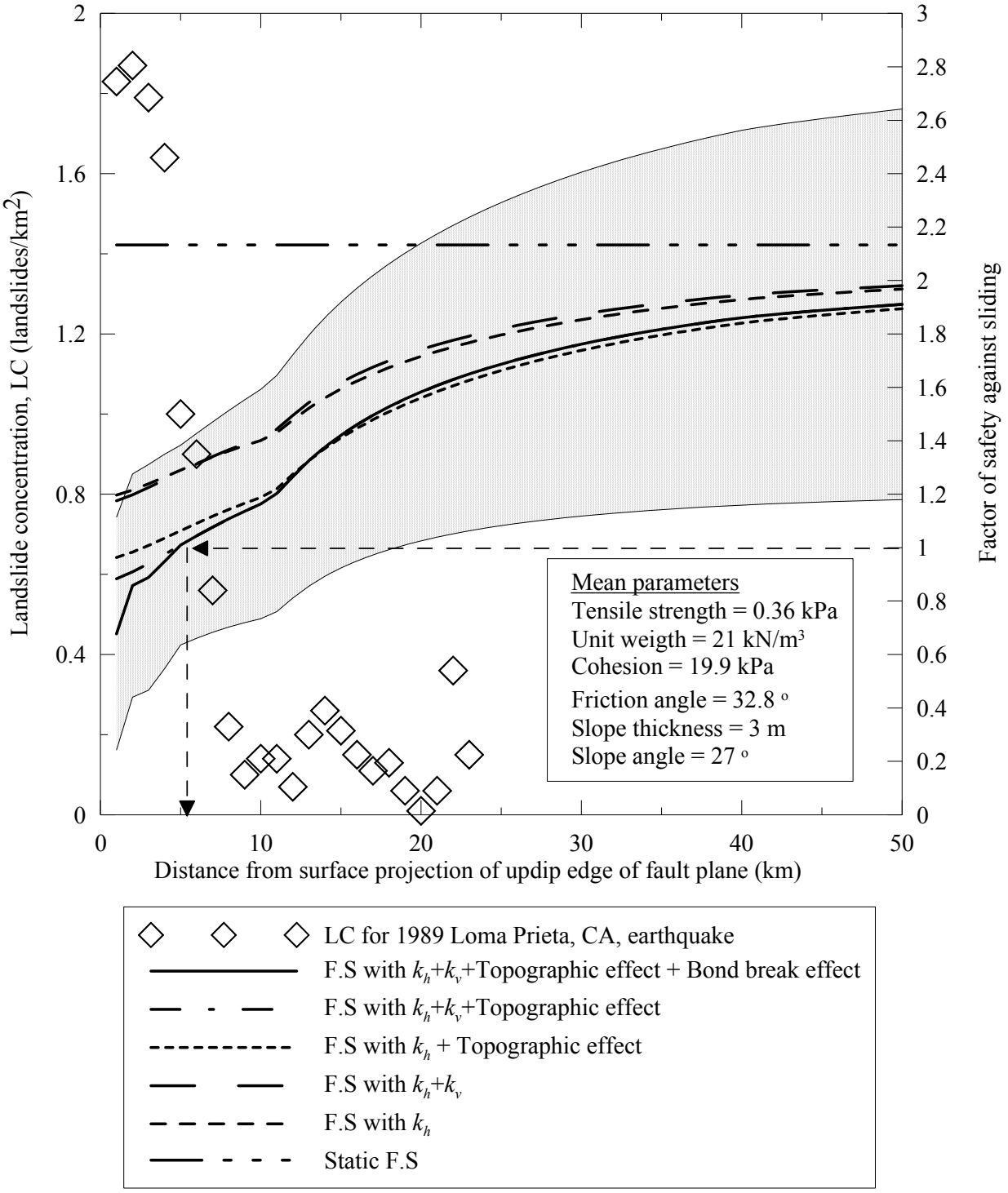

Figure 9-9 Landslide concentration data for the 1989 Loma-Prieta earthquake by Keefer (2000) and factor of safety calculated by using various effects. The mean FS ± 1 standard deviation are shown in a shaded area.

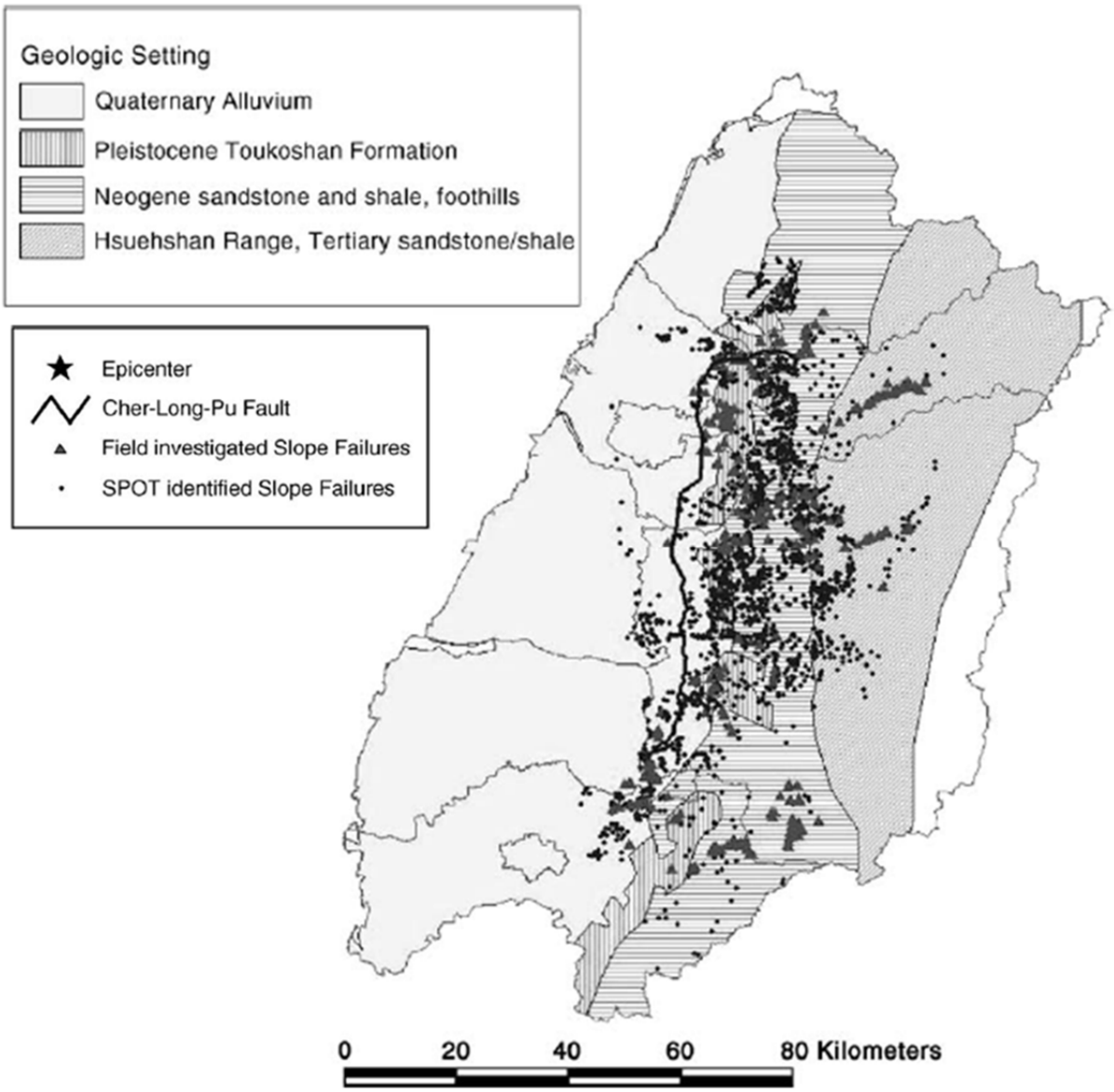

Figure 9-10 Locations of landslides induced by 1999 Chi-Chi, Taiwan, earthquake along the Cher-Long-Pu fault and geological setting of affected area (Khazai and Sitar 2004)

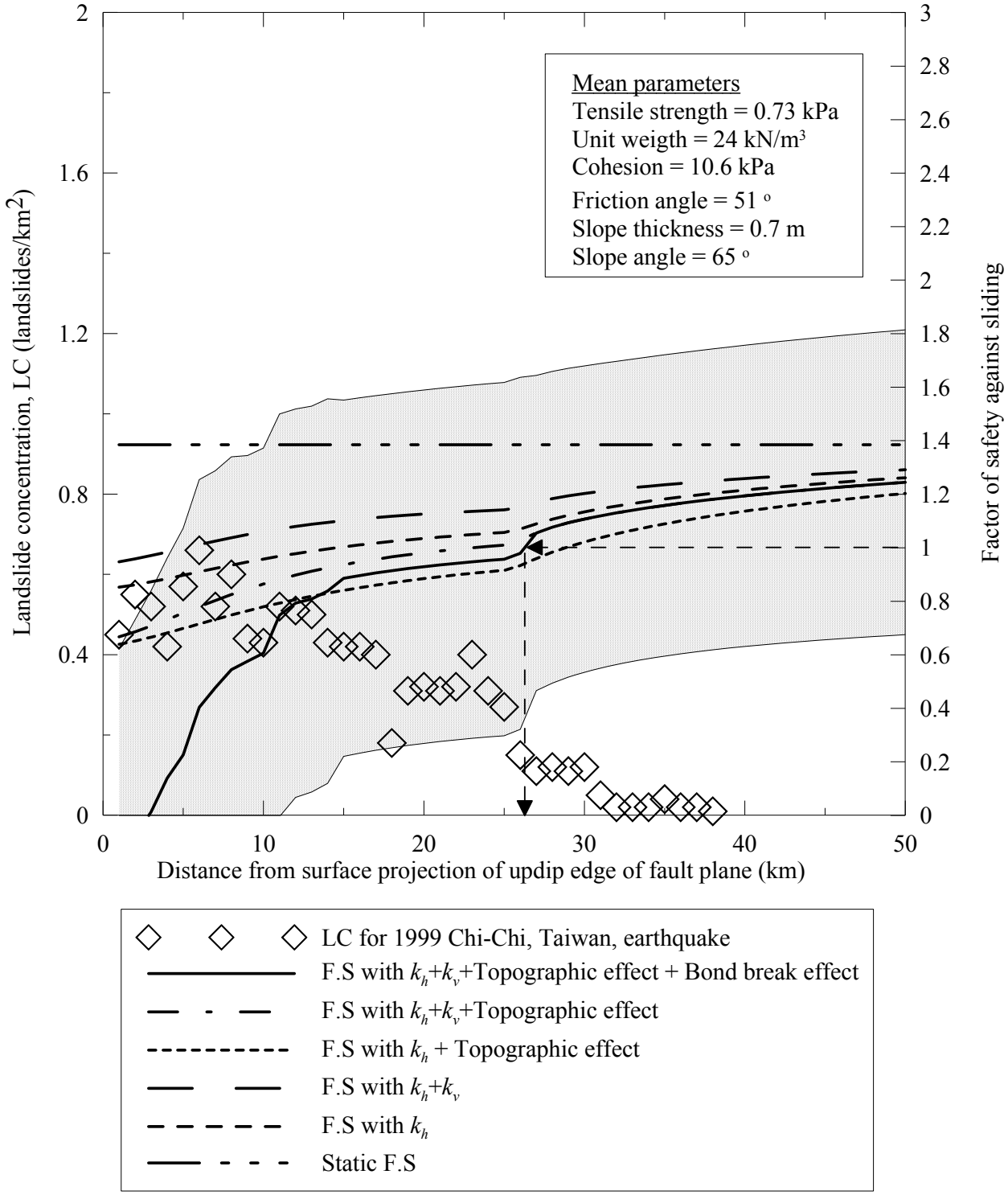

Figure 9-11 Landslide concentration data for the 1999 Chi-chi, Taiwan, earthquake (Khazai and Sitar 2004) and factor of safety calculated by using various effects.

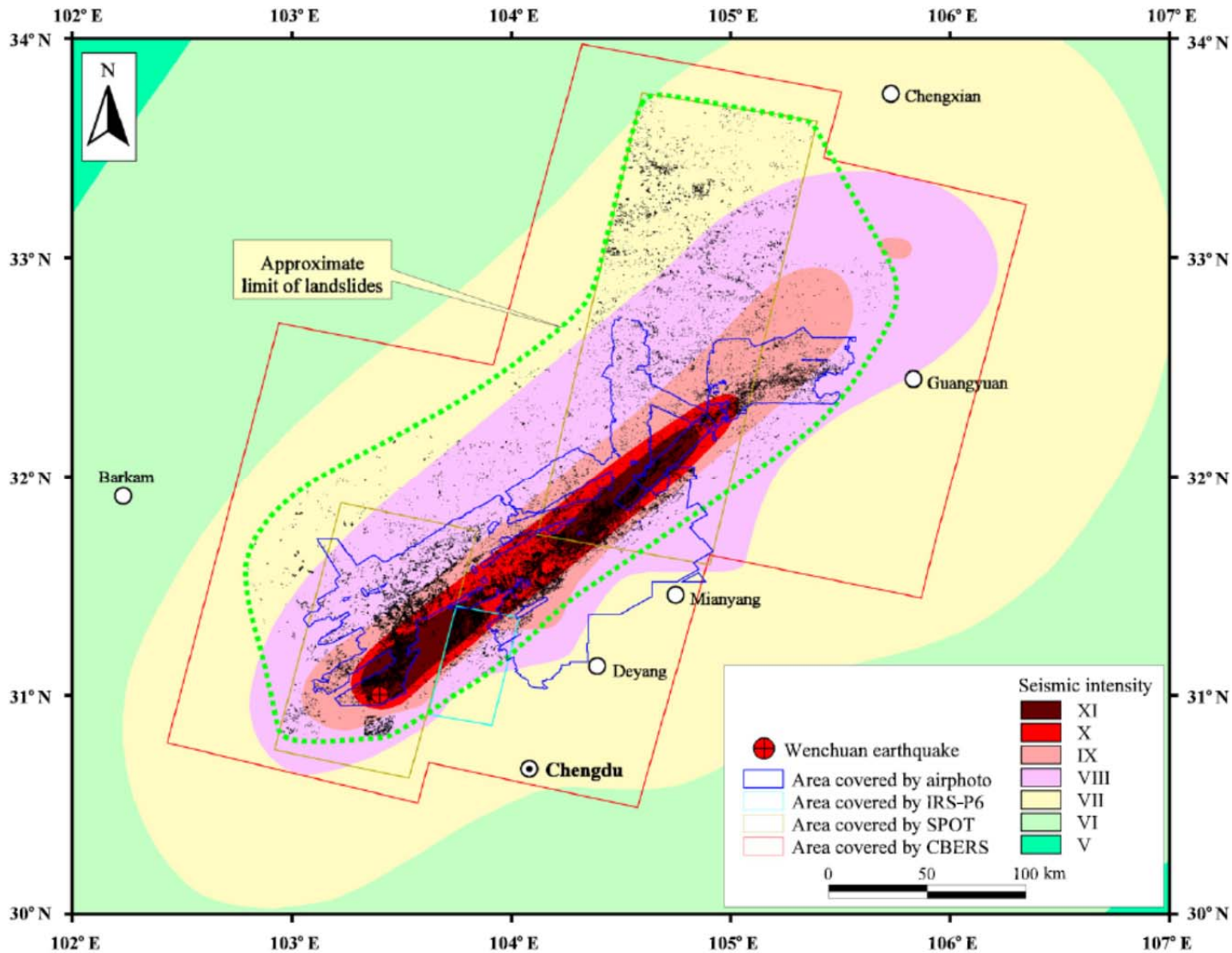

Figure 9-12 Distribution of earthquake-triggered landslides (black polygons) on the isoseismic map (Dai et al. 2010)

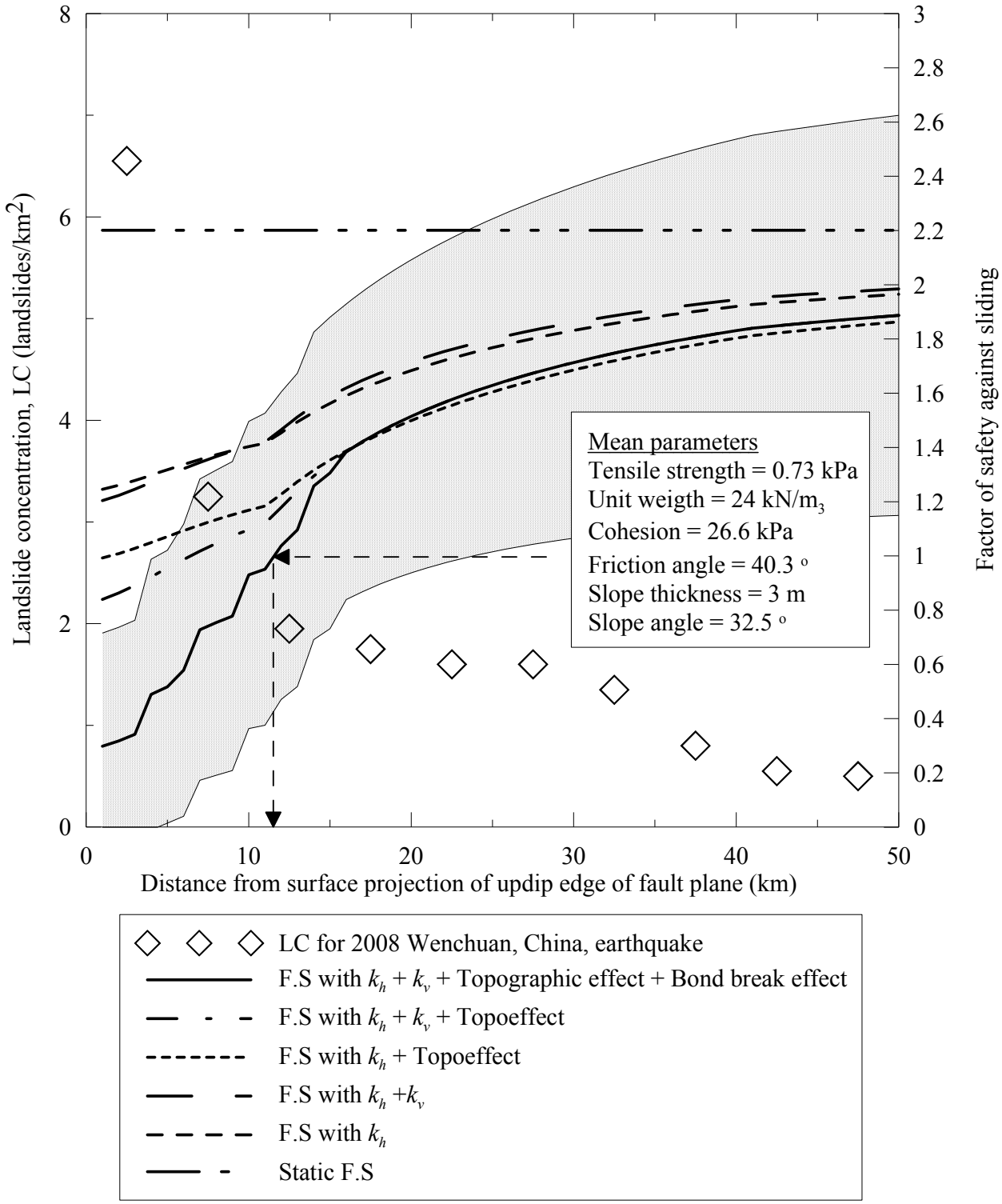

Figure 9-13 Landslide concentration data for the 2008 Wenchuan, China, earthquake (Dai et al. 2010) and factor of safety calculated by using various effects.

CHAPTER 10. CONCLUSIONS

The methodology of seismic hazard analysis in NW Pakistan was proposed in this report. In lieu of using the area source zones proposed by other studies (NORSAR and PMD 2006; PMD and NORSAR 2006; Monalisa et al. 2007), 32 discrete faults were employed with their surface traces, geometries, and faulting mechanisms. Then the earthquake catalog was used to construct the exponential recurrence models. For activity rate of the exponential recurrence model, two different period of earthquake catalogs were used; including and excluding the earthquake event in 2005. This was because of that extremely high amount of foreshocks and aftershocks of 2005 Kashmir earthquake could bias the result. The earthquake data from the recent 30-year interval were used to estimate the activity rate and *b*-value because earthquakes for $4 \leq M_w < 6$ are considered to be incomplete prior to 1975. We found that the large magnitude range of computed recurrence model match with the earthquake data for 100-year interval. In order to estimate characteristic rate of the characteristic recurrence model, three methods were proposed. The first method assumes that the characteristic rate is related with the slip rate of faults. The second method employs the assumption that the characteristic rate is proportional to the activity rate. The third method is using the seismic moment balance method proposed by Aki (1966). All these parameters and models were implemented in the logic tree and reasonable weight for each branch of the logic tree was assigned. Finally four NGAs were selected based on the fact that they can capture the measured ground acceleration during the 2005 Kashmir, Pakistan, earthquake, and were used according to the fault models developed in this study.

Although this report estimated some of the input parameters based on best estimates due to lack of information on fault properties in NW Pakistan, it is necessary to obtain these parameters as appropriately as possible in the future to yield the most reliable results. Obtaining

the precise fault width and dip is very important task in seismic hazard analysis not only because the fault geometry determines the distance between source and site, but also because it affects the determination of upper bound magnitude. Slip rate of individual fault is another important fault property that needs to be well investigated because it plays a significant role in estimating the proper characteristic rate.

Seismic hazard curves and uniform response spectra were generated for selected cities. Seismic hazard maps corresponding to 475, 975 and 2475 return periods were also generated for the entire region. The results show that cities with the highest hazards are Kaghan and Muzaffarabad, with PGA ~ 0.6g for a 475-year return period. Islamabad, the capital city of Pakistan, also has a significant seismic hazard, much higher than predicted by previous studies. On the other hand, much lower ground motions were predicted for the cities located farther from active faults, including Astor, Bannu, Malakand, Mangla, Peshawar, and Talagang. However, the PGAs computed for these cities are still similar to or slightly higher than those by previous studies.

Despite the uncertainties and assumptions associated with both the deterministic and probabilistic seismic hazard analyses, the results from both methodologies were comparable, thus providing a measure of confidence in the results. The computed hazards also correspond well to the known seismic history of the region, including the recent 2005 Kashmir earthquake. In addition, use of the conditional mean spectrum instead of the uniform hazard spectrum could provide significant efficiency in seismic design in many cities in NW Pakistan.

When earthquakes occur in mountainous regions, earthquake-induced landslides and rockfalls commonly cause significant damage. However, current practice of using pseudo-static slope stability analysis to evaluate landslides only accounts for the horizontal ground

acceleration, and does not predict factors of safety that are consistent with available landslide concentration data. This report proposed three other factors that can influence rock slope stability: (1) vertical ground accelerations; (2) topographic effects; and (3) "bond break" effects.

The vertical ground acceleration, when estimated using available attenuation relations and vertical-to-horizontal acceleration ratios, can equal the horizontal acceleration in the near-fault region for large magnitude earthquakes. For gentle to moderate slopes (i.e., less than ~ 60°) and sliding depths exceeding about 1 m, incorporating large vertical accelerations in a pseudo-static stability analysis tends to decrease the FS. While the effect of vertical acceleration on the computed FS is not significant, this study suggests that it should not be ignored. Furthermore, both the horizontal and vertical accelerations may be amplified near slope crests as a result of constructive geometric wave interference, i.e., topographic effects. When the vertical acceleration was amplified by a topographic factor, the effect of vertical accelerations on FS became more important. Lastly, the occurrence of high amplitude vertical accelerations on slopes may damage or "break" interparticle bonding (i.e., cementation, cohesion, etc.) along rock bedding planes, particularly near the ground surface where weathering and jointing is commonly more severe, effectively eliminating the equivalent cohesion of the rock. If bonding is destroyed, the FS can decrease considerably. In fact, observations in many earthquakes suggest that most earthquake-induced landslides are shallow, disrupted slides and falls that occur near slope crests or peaks, where topographic amplification and bond break effects are most likely to occur.

In this report, we propose a new approach to evaluate regional pseudo-static slope stability that accounts for vertical accelerations, potential topographic amplification, and potential bond breakage. The procedure was incorporated into a logic tree approach to account for variability in both rock and geometric properties of the slope. To examine the applicability of

the newly proposed method, we compared the factors of safety computed with this procedure to landslide concentration data collected during four recent earthquakes (1989 Loma-Prieta, 1999 Chi-Chi, 2005 Kashmir, and 2008 Wenchuan). Observations from these events all show abrupt changes in landslide concentration in the near-fault region. When the computed FS incorporates vertical accelerations, topographic effects, and bond breakage, the FS trends are consistent with the observed trends in landslide concentration, and qualitatively explain the abrupt increase in landslide concentration in the near-fault region of these earthquakes.

REFERENCES

Abrahamson, N., et al. (2008). "Comparisons of the NGA ground-motion relations." Earthquake Spectra 24(1): 45-66.

Abrahamson, N. and Silva, W. (2008). "Summary of the Abrahamson & Silva NGA ground-motion relations." Earthquake Spectra 24(1): 67-97.

Abrahamson, N. A. and Litehiser, J. J. (1989). "Attenuation of vertical peak acceleration." Bulletin - Seismological Society of America 79(3): 549-580.

Aki, K. (1966). "Generation and propagation of G-waves from the Niigata earthquake of June 19, 1964. Part 2. Estimation of earthquake movement, released energy, and stress-strain drop from G-wave spectrum." Bull. Earthquake Res. Inst. 44: 23-88.

Ambraseys, N. and Bilham, R. (2000). "A note on the Kangra Ms = 7.8 earthquake of 4 April 1905." Current Science 79(1): 45-50.

Ambraseys, N. N. and Douglas, J. (2004). "Magnitude calibration of north Indian earthquakes." Geophysical Journal International 159(1): 165-206.

Ambraseys, N. N., et al. (2005). "Equations for the estimation of strong ground motions from shallow crustal earthquakes using data from Europe and the middle east: Horizontal peak ground acceleration and spectral acceleration." Bulletin of Earthquake Engineering 3(1): 1-53.

Ambraseys, N. N., et al. (2005). "Equations for the estimation of strong ground motions from shallow crustal eUsing data from Europe and the middle east: Vertical peak ground acceleration and spectral acceleration." Bulletin of Earthquake Engineering 3(1): 55-73.

Ambraseys, N. N. and Simpson, K. A. (1995). Prediction of vertical response spectra in Europe. Research Report ESEE-95/1, Imperial College.

Ambraseys, N. N. and Simpson, K. A. (1996). "Prediction of vertical response spectra in Europe." Earthquake Engineering and Structural Dynamics 25(4): 401-412.

Ambraseys, N. N., et al. (1996). "Prediction of horizontal response spectra in Europe." Earthquake Engineering and Structural Dynamics 25(4): 371-400.

Ashford, S. A. and Sitar, N. (1997). "Analysis of topographic amplification of inclined shear waves in a steep coastal bluff." Bulletin of the Seismological Society of America 87(3): 692-700.

Ashford, S. A., et al. (1997). "Topographic effects on the seismic response of steep slopes." Bulletin of the Seismological Society of America 87(3): 701-709.

Assimaki, D. and Gazetas, G. (2004). "Soil and topographic amplification on canyon banks and the 1999 Athens earthquake." Journal of Earthquake Engineering 8(1): 1-43.

Assimaki, D., et al. (2005). "Soil-dependent topographic effects: A case study from the 1999 Athens earthquake." Earthquake Spectra 21(4): 929-966.

Aydan, Ã., et al. (2009). "Geotechnical evaluation of slope and ground failures during the 8 October 2005 Muzaffarabad earthquake, Pakistan." Journal of Seismology 13(3): 399-413.

Baker, J. W. (2008). "The conditional mean spectrum: A tool for ground motion selection." Journal of Structural Engineering in review.

Baker, J. W. and Cornell, C. A. (2006). "Spectral shape, epsilon and record selection." Earthquake Engineering and Structural Dynamics 35(9): 1077-1095.

Baker, J. W. and Jayaram, N. (2008). "Correlation of spectral acceleration values from NGA ground motinos models." Earthquake spectra 24(1): 299-317.

Bazzurro, P. and Cornell, C. A. (1999). "Disaggregation of seismic hazard." Bulletin of the seismological society of America 89(2): 501-520.

Bendick, R., et al. (2007). "Slip on an active wedge thrust from geodetic observations of the 8 October 2005 Kashmir earthquake." Geology 35(3): 267-270.

Bernreuter, D. L. (1992). "Determining the Controlling Earthquake from Probabilistic Hazards for the Proposed Appendix B." Lawrence Livermore National Laboratory Report UCRL-JC-111964.

Bhat, G. M., et al. (2005). October 8 Kashmir Earthquake: Impact on geoenvironment and structures in the Karnah and Uri Tehsils of Kashmir (India), Post Graduate Department of Geology, Univeristy of Jammu.

Bilham, R. (2004). "Historical Studies on Earthqaueks in India." Annals of Geophysics.

Bilham, R. and Ambraseys, N. (2005). "Apparent Himalayan slip deficit from the summation of seismic moments for Himalayan earthquakes, 1500-2000." Current Science 88(10): 1658-1663.

Bonilla, M. G., et al. (1984). "Statistical relations among earthquake magnitude, surface rupture length, and surface fault displacement." Bulletin of the seismological society of America 74(6): 2379-2411.

Boore, D. M. (1972). "Note on effect of simple topography on seismic SH waves." Bulletin of the Seismological Society of America 62(1): 275-&.

Boore, D. M. and Atkinson, G. M. (2008). "Ground-motion prediction equations for the average horizontal component of PGA, PGV, and 5%-damped PSA at spectral periods between 0.01 s and 10.0 s." Earthquake Spectra 24(1): 99-138.

Boore, D. M., et al. (1997). "Equations for estimating horizontal response spectra and peak acceleration from western North American earthquakes: A summary of recent work." Seismological Research Letters 68(1): 128-153.

Bouckovalas, G. D. and Papadimitriou, A. G. (2005). "Numerical evaluation of slope topography effects on seismic ground motion." Soil Dynamics and Earthquake Engineering 25(7-10): 547-558.

Bray, J. D., et al. (1998). "Simplified seismic design procedure for geosynthetic-lined, solid-waste landfills." Geosynthetics International 5(1-2): 203-235.

Brown, P. T. and Booker, J. R. (1985). "Finite Element Analysis of Excavation." Computers and Geotechnics 1: 207-220.

Campbell, K. W. and Bozorgnia, Y. (2003). "Updated near-source ground-motion (attenuation) relations for the horizontal and vertical components of peak ground acceleration and acceleration response spectra." Bulletin of the Seismological Society of America 93(1): 314-331.

Campbell, K. W. and Bozorgnia, Y. (2007). Campbell-Bozorgnia NGA ground motion relations for the geometric mean horizontal component of peak and spectral ground motion parameters, Pacific Earthquake Engineerign Research Center.

Campbell, K. W. and Bozorgnia, Y. (2008). "NGA ground motion model for the geometric mean horizontal component of PGA, PGV, PGD and 5% damped linear elastic response spectra for periods ranging from 0.01 to 10 s." Earthquake Spectra 24(1): 139-171.

Castellani, A., et al. (1982). "Seismic response of topographic irregularities." Soil dynamics and earthquake engineering. Proc. conference, Southampton, July 1982. Vol. 1: 251-268.

Celebi, M. (1987). "Topographical and geological amplifications determined from strong-motion and aftershock records of the 3 March 1985 Chile earthquake." Bulletin of the Seismological Society of America 77(4): 1147-1167.

Celebi, M. (1991). "Topographical and geological amplification: case studies and engineering implications." Structural Safety 10(1-3): 199-217.

Chiou, B. S. J. and Youngs, R. R. (2008). "An NGA model for the average horizontal component of peak ground motion and response spectra." Earthquake spectra 24(1): 173-215.

Cornell, C. A. (1968). "Engineering seismic risk analysis." Bulletin of Seismological Society of America 58: 1583-1606.

Cornell, C. A. and Vanmarcke, E. H. (1969). The major influences on seismic risk. Proceedings of the Fourth World Conferences on Earthquake Engineering. Santiago, Chile. A(1)**:** 69-93.

Cui, P., et al. (2009). "The 12 May Wenchuan earthquake-induced landslide lakes: Distribution and preliminary risk evaluation." Landslides 6(3): 209-223.

Dai, F. C., et al. (2011). "Spatial distribution of landslides triggered by the 2008 Ms 8.0 Wenchuan earthquake, China." Journal of Asian Earth Sciences 40(4): 883-895.

Dasgupta, S., et al. (2000). Seismotectonic atlas of India and its environs. P. L. Narula, S. K. Acharyya and J. Banerjee, Geological Survey of India.

Dipietro, J. A., et al. (2000). The main mantle thrust in Pakistan: Its character and extent. Geological Society Special Publication**:** 375-393.

Dunning, S. A., et al. (2007). "The Hattian Bala rock avalanche and associated landslides triggered by the Kashmir Earthquake of 8 October 2005." Engineering Geology 93(3-4): 130-144.

Durrani, A. J., et al. (2005). The Kashmir Earthquake of October 8, 2005. A quick look report. Urbana, Mid-America Earthquake Center, University of Illinois at Urbana-Champaign**:** 51 p.

EC8 (2000). Design Provisions for Earthquake Resistance of Structures, Prt 1-1: General rules-Seismic Actions and General Requirements for Structures. prEN. 1998-5.

Elnashai, A. S. and Papazoglou, A. J. (1997). "Procedure and spectra for analysis of RC structures subjected to strong vertical earthquake loads." Journal of Earthquake Engineering 1(1): 121-155.

French Association for Earthquake Engineering (AFPS) (1995). Guidelines for Seismic Microzonation studies. October.

Gardner, J. K. and Knopoff, L. (1974). "Is the sequence of earthquakes in Southern California, with aftershocks removed, Poissonian?" Bulletin of the Seismological society of America 64(5): 1363-1367.

Gazetas, G., et al. (2002). "Topography and soil effects in the Ms 5.9 Parnitha (Athens) earthquakes: The case of Adámes." Natural Hazards 27(1-2): 133-169.

Graizer, V. (2009). "Low-velocity zone and topography as a source of site amplification effect on Tarzana hill, California." Soil Dynamics and Earthquake Engineering 29(2): 324-332.

Green, M. G. (1994). "Construction of the San Antonio, Texas, flood control tunnels." Bulletin of the Association of Engineering Geologists XXXI(1): 15-31.

Grunthal, G. and Wahlstrom, R. (2003). "An Mw based earthquake catalogue for central, northern and northwestern Europe using a hierarchy of magnitude conversions." Journal of Seismology 7.

Gutenberg, B. and Richter, C. F. (1954). Seismicity of the earth and associated phenomena. Princeton, N.J., Princeton University Press.

Hanks, T. C. and Bakun, W. H. (2002). "A bilinear source-scaling model for M-log A observations of continental earthquakes." Bulletin of the seismological society of America 92(5): 1847-1846.

Hanks, T. C. and Bakun, W. H. (2008). "M-log A observations for recent large earthquakes." Bulletin of the seismological society of America 98(1): 490-494.

Hanks, T. C. and Kanamori, H. (1979). "A moment magnitude scale." Journal of Geophysical Research B: Solid Earth 84(B5): 2348-2350.

Hartzell, S. H., et al. (1994). "Initial investigation of site and topographic effects at Robinwood Ridge, California." Bulletin - Seismological Society of America 84(5): 1336-1349.

Heuckroth, L. E. and Karim, R. A. (1973). "Afghan seismotectonics." Philosophical Transactions of the Royal Society of London Series a-Mathematical Physical and Engineering Sciences 274(1239): 389-395.

Hoek, E., et al. (2002). "Hoek-Brown failure criterion-2002 edition." Proceedings of the Fifth North American Rock Mechanics Symposium 1: 267-273.

Hough, S. E., et al. (2010). "Localized damage caused by topographic amplification during the 2010 M7.0 Haiti earthquake." Nature Geoscience 3(11): 778-782.

Hung, J. J. (2000). "Chi-Chi earthquake induced landslides in Taiwan." Earthquake Engineering and Engineering Seismology 2(2): 25-33.

Hynes-Griffin, M. E. and Franklin, A. G. (1984). Rationalizing the seismic coefficient method. Miscellaneous Paper GL-84-13. Vicksburg, Mississippi, U. S. Army Corps of Engineers Waterways Experiment Station**:** 521 pp.

Idriss, I. M. (2008). "An NGA empirical model for estimating the horizontal spectral values generated by shallow crustal earthquakes." Earthquake Spectra 24(1): 217-242.

Idriss, I. M. and Seed, H. B. (1967). "Response of earth banks during earthquakes." Soil Mechanics and Foundations Division, ASCE 93(SM3): 61-82.

Jayangondaperumal, R., et al. (2008). "Liquefaction features of the 2005 Muzaffarabad-Kashmir earthquake and evidence of palaeoearthquakes near Jammu, Kashmir Himalaya." Current Science 95(8): 1071-1077.

Johnston, A. C. (1996). "Seismic moment assessment of earthquakes in stable continental regions - I. Instrumental seismicity." Geophysical Journal International 124(2): 381-414.

Kamp, U., et al. (2008). "GIS-based landslide susceptibility mapping for the 2005 Kashmir earthquake region." Geomorphology 101(4): 631-642.

Kaul, P. H. (1911). Census of India.

Keefer, D. K. (1984). "Landslides caused by earthquakes." Geological Society of America Bulletin 95(4): 406-421.

Keefer, D. K. (2000). Statistical analysis of an earthquake-induced landslide distribution - the 1989 Loma Prieta, California event.

Keefer, D. K. and Manson, M. W. (1989). Regional distribution and characteristics of landslides generated by the earthquake. The Loma Prieta, California, earthquake of October 17, 1989: Strong ground motion and ground failure. D. K. Keefer., U.S. Geological Survey Professional Paper 1551-C.

Keefer, D. K. and Manson, M. W. (1998). "Regional distribution and characteristics of landslides generated by the earthquake." US Geological Survey Professional Paper 1551-C: 7-32.

Khazai, B. and Sitar, N. (2004). "Evaluation of factors controlling earthquake-induced landslides caused by Chi-Chi earthquake and comparison with the Northridge and Loma Prieta events." Engineering Geology 71(1-2): 79-95.

Kim, B., et al. (2010). Probabilistic seismic hazard analysis for Islamabad and Peshawar in Pakistan using discrete faults. 5th International Conference on Earthquake Geotechnical Engineering, Santiago, Chile.

Kokusho, T. and Ishizawa, T. (2007). "Energy approach to earthquake-induced slope failures and its implications." Journal of Geotechnical and Geoenvironmental Engineering 133(7): 828-840.

Kokusho, T. and Kabasawa, K. (2003). "Energy approach to flow failure and its application to flow due to water film in liquefied deposits." Proc., Int. Conf. on Fast Slope Movement: 297-302.

Kovacs, W. D., et al. (1971). "Studies of seismic response of clay banks." ASCE J Soil Mech Found Div 97(SM2).

Kramer, S. L. (1996). Geotechnical earthquake engineering. Upper Saddle River, N.J., Prentice Hall.

Kramer, S. L. and Smith, M. W. (1997). "Modified Newmark model for seismic displacements of compliant slopes." Journal of Geotechnical and Geoenvironmental Engineering 123(7): 635-644.

Lambe, P. C. and Hansen, L. A. (1990). "Design and Performance of Earth Retaining Structures - Proceedings of a Conference." Geotechnical Special Publication(25 1990): 439-470
ubl by ASCE, New York, NY, USA.

Larson, K. M., et al. (1999). "Kinematics of the India-Eurasia collision zone from GPS measurements." Journal of Geophysical Research B: Solid Earth 104(B1): 1077-1093.

Lawrence, W. R. (1967). The valley of Kashmir, Kesar Publishers.

Lee, I. K., et al. (1983). Geotechnical Engineering. Boston, Pitman.

Liao, H. W. (2000). Landslides triggered by Chi-Chi earthquake. Institiute of Geophysics. Chung-Li, National Central University. Master**:** 90.

Lin, J. S. and Whitman, R. V. (1983). "Decoupling approximation to the evaluation of earthquake-induced plastic slip in earth dams." Earthquake Engineering and Structural Dynamics 11(5 , Sep.-Oct. 1983, p.667-678.).

Lungarini, L., et al. (2005). "Finite element modelling of topographic effects on elastic ground deformation at Mt. Etna." Journal of Volcanology and Geothermal Research 144(1-4 SPEC. ISS.): 257-271.

Makdisi, F. I. and Seed, H. B. (1978). "Simplified procedure for estimating dam and embankment earthquake-induced deformations." Journal of the Geotechnical Engineering Division 104(GT7): 849-867.

Marcuson, W. F. I. and Curro, J. R. (1981). "Field and laboratory determination of soil moduli." Journal of the Geotechnical Engineering Division 107(GT10): 1269-1291.

McDougall, J. W. and Khan, S. H. (1990). "Strike-slip faulting in a foreland fold-thrust belt: the Kalabagh Fault and western Salt Range, Pakistan." Tectonics 9(5): 1061-1075.

McGuire, R. K. (1995). "Probabilistic seismic hazard analysis and design earthquakes: closing the loop." Bulletin - Seismological Society of America 85(5): 1275-1284.

Meunier, P., et al. (2007). "Regional patterns of earthquake-triggered landslides and their relation to ground motion." Geophysical Research Letters 34(20).

Monalisa, et al. (2007). "Seismic hazard assessment of the NW Himalayan fold-and-thrust belt, Pakistan, using probabilistic approach." Journal of Earthquake Engineering 11(2): 257-301.

Monalisa and Qasim Jan, M. (2010). "Geoseismological study of the Ziarat (Balochistan) earthquake (doublet?) of 28 October 2008." Current Science 98(1): 50-57.

Mukhopadhyay, D. K. and Mishra, P. (2005). "A balanced cross section across the Himalayan frontal fold-thrust belt, Subathu area, Himachal Pradesh, India: Thrust sequence, structural evolution and shortening." Journal of Asian Earth Sciences 25(5): 735-746.

Nason, R. D. (1971). Shattered earth at Wallaby Street, Sylmar, in the San Fernando, California, earthquake of February 9, 1971, U.S. Geological Survey Professional Paper 733**:** 97-98

Newmark, N. M. (1965). "Effects of earthquakes on dams and embankments." Geotechnique 15(2): 139-&.

NORSAR and PMD (Pakistan Meterological Department) (2006). Seismic Hazard Analysis for the Cities of Islamabad and Rawalpindi.

Nowroozi, A. A. (1985). "Empirical relations between magnitude and fault parameters for earthquakes in Iran." Bull. Seismol. Soc. Am 75(5): 1327-1338.

Nozu, A., et al. (1997). Relation between seismic coefficient and peak ground acceleration estimated from attenuation relation., Technical Note of the Port and Harbor Research Institute. Ministry of Transport, Japan.

Owen, L. A., et al. (2008). "Landslides triggered by the 8 October 2005 Kashmir earthquake." Geomorphology 94(1-2): 1-9.

Petersen, M. D. (2008). Documentation for the 2008 Update of the United States National Seismic Hazard Maps, USGS.

PMD (Pakistan Meterological Department) and NORSAR (2006). Seismic Hazard Analysis and Zonation of Azad Kashmir and Northern Areas of Pakistan.

Power, M., et al. (2008). "An overview of the NGA project." Earthquake spectra 24(1): 3-21.

Pyke, R. (1991) Selection of seismic coefficients for use in pseudo-static slope stability analyses.

Quittmeyer, R. C. and Jacob, K. H. (1979). "Historical and modern seismicity of Pakistan, Afghanistan, Northwestern India, and Southeastern Iran." Bulletin of the seismological society of America 69(3): 773-823.

Raghukanth, S. T. G. (2008). "Ground motion estimation during the Kashmir earthquake of 8th October 2005." Natural Hazards 46(1): 1-13.

Rathje, E. M. and Bray, J. D. (2000). "Nonlinear coupled seismic sliding analysis of earth structures." Journal of Geotechnical and Geoenvironmental Engineering 126(11): 1002-1014.

Reiter, L. (1990). Earthquake hazard analysis : issues and insights. New York, Columbia University Press.

Sanchezsesma, F. J., et al. (1982). "A boundary method for elastic wave diffraction - Application to scattering of SH-waves by surface irregularities." Bulletin of the Seismological Society of America 72(2): 473-490.

Sato, H. P., et al. (2007). "Interpretation of landslide distribution triggered by the 2005 Northern Pakistan earthquake using SPOT 5 imagery." Landslides 4(2): 113-122.

Searle, M. P. (1996). "Geological evidence against large-scale pre-Holocene offsets along the Karakoram Fault: Implications for the limited extrusion of the Tibetan plateau." Tectonics 15(1): 171-186.

Seed, H. B. (1979). "Considerations in the earthquake-resistant design of earth and rockfill dams." Geotechnique 29(3): 215-263.

Sella, G., et al. (2002). "REVEL: A model for recent plate velocities from space geodesy." Journal of Geophysical Research B: Solid Earth 107(4): 11-11.

Singh, D. D. (2000). "Seismotectonics of the Himalaya and its vicinity from centroid-moment tensor (CMT) solution of earthquakes." Journal of Geodynamics 30(5): 507-537.

Sitar, N. and Clough, G. W. (1983). "Seismic response of steep slopes in cemented soils." Journal of Geotechnical Engineering-Asce 109(2): 210-227.

Slemmons, D. B. (1982). Determination of design earthquake magnitudes for microzonation. Proceedings, 3rd International Earthquake Microzonation Conference. Seattle, Washington. 1**:** 119-130.

Slemmons, D. B., et al. (1989). "Determination of earthquake size from surface faulting events." Proc. Int. Seminar on Seismic Zoning, China.

Smith, W. D. (1975). "Application of finite element analysis to body wave progagation problems." Geophysical Journal of the Royal Astronomical Society 42(2): 747-768.

Somerville, P. G., et al. (1997). "Modification of empirical strong ground motion attenuation relations to include the amplitude and duration effects of rupture directivity." Seismological Research Letters 68(1): 199-222.

Stamatopoulos, C. A., et al. (2007). "Mitigation of the seismic motion near the edge of cliff-type topographies." Soil Dynamics and Earthquake Engineering 27(12): 1082-1100.

Stepp, J. C. (1972). Analysis of completeness of the earthquake sample in the Puget Sound Area and its effect on statistical estimates of earthquake hazard. Proc. of the International Conference on Microzonations.

Tang, C. L., et al. (2009). "The Tsaoling landslide triggered by the Chi-Chi earthquake, Taiwan: Insights from a discrete element simulation." Engineering Geology 106(1-2): 1-19.

Terzaghi, K. (1950). Mechanism of Landslides. The Geological Society of America, Berkey. November**:** 83-123.

Tocher, D. (1958). "Earthquake energy and ground breakage." Bulletin of the seismological society of America 48(2): 147-153.

U.S. Department of Energy (U.S. DOE) (1996). Natural Phenomena Hazards Assessment Criteria, DOE-STD-1023-96. Washington, D.C.

U.S. Nuclear Regulatory Commission (U.S. NRC) (1997). Identification and characterization of seismic sources and determination of safe shutdown earthquake ground motion, Regulations 10 CFR Part 100, Regulatory Guide 1.165, Apendix C. Washinton, D.C.

USGS (2010). "Magnitude 7.6 - Pakistan." Earthquake Hazards Program. http://earthquake.usgs.gov/earthquakes/eqinthenews/2005/usdyae/usdyae.php.

Weichert, D. H. (1980). "Estimation of the earthquake recurrence parameters for unequal observation periods for different magnitudes." Bulletin of the Seismological society of America 70: 1337-1356.

Wells, D. L. and Coppersmith, K. J. (1994). "New empirical relationships among magnitude, rupture length, rupture width, rupture area, and surface displacement." Bulletin of teh Seismological Society of America 84(4): 974-1002.

WGCEP (2003). Earthquake probabilities in the San Francisco Bay Region 2002-2031, U.S. Geological Survey Open-File Report 03-214.

WGCEP (2008). The uniform California earthquake rupture forcast, version 2 (UCERF 2), U.S. Geological Survey Open-File Report 2007-1437 and California Geological Survey Special Report 203.

Yegian, M. K., et al. (1991). "Earthquake-induced permanent deformations. Probabilistic approach." Journal of geotechnical engineering 117(1): 35-50.

Yin, Y., et al. (2009). "Landslide hazards triggered by the 2008 Wenchuan earthquake, Sichuan, China." Landslides 6(2): 139-151.

Youngs, R. R. and Coppersmith, K. J. (1985). "Implications of fault slip rates and earthquake recurrence models to probabilistic seismic hazard assessments." Bulletin of the seismological society of America 75(4): 939-964.

Zhao, C. and Valliappan, S. (1993). "Seismic wave scattering effects under different canyon topographic and geological conditions." Soil Dynamics and Earthquake Engineering 12(3): 129-143.